



SMR.550 - 14

**SPRING COLLEGE IN MATERIALS SCIENCE ON  
"NUCLEATION, GROWTH AND SEGREGATION IN MATERIALS  
SCIENCE AND ENGINEERING"  
( 6 May - 7 June 1991 )**

---

**BACKGROUND MATERIAL FOR LECTURES ON  
"EXTENDED DEFECTS"**

**E.J. SAVINO**  
Proyecto Multinacional de Investigacion y  
Desarrollo en Materiales - OEA-CNEA  
Av. del Libertador 8250  
1429 Buenos Aires  
Argentina

---

**These are preliminary lecture notes, intended only for distribution to participants.**



SPRING COLLEGE IN MATERIALS SCIENCE  
on "NUCLEATION, GROWTH AND SEGREGATION  
IN MATERIALS SCIENCE AND ENGINEERING"

I.C.T.P., 6 May - 7 June, 1991

ADDITIONAL MATERIAL TO LECTURE NOTES ON "EXTENDED DEFECTS" -  
E.J. SAVINO

INDEX

1. Elastic field of defects

"The Dislocation Loop in an Anisotropic Medium and Its Interaction with an Interstitial Atom", by N. Meissner, E. J. Savino, J. R. Willis and R. Bullough

2. Static Lattice Distortion of Point Defects

"Lattice static Green function for an hcp lattice" by R. Migoni, C. N. Tome, N. Smetniansky-De Grande and E. J. Savino

"Atomic Displacements Around Nitrogen Interstitial Impurities in Ta and Nb", by S. Rao, E. J. Savino and C. R. Houska

"The morphology of planar vacancy aggregates in copper" by E. J. Savino and R. C. Perrin

3. Planar Defects

"The influence of local volume forces on surface relaxation of pure metals and alloys: applications to Ni, Al and Ni<sub>3</sub>Al", by E. J. Savino and D. Farkas

"Oscillatory relaxations in (111) planar defects in Ni<sub>3</sub>Al", by D. Farkas, E. J. Savino, P. Chidambaram, A. F. Voter, D. J. Srolovitz and S. P. Chen

#### 4. Dislocation Core

"Core Structure of Straight Dislocations in  $\text{Ni}_3\text{Al}$ ", by R. Pasianot, D. Farkas and E. J. Savino

"Comparison of TEM Observations with Dislocation Core Structure Calculations in B2 ordered compounds", by D. Farkas, R. Pasianot, E. J. Savino and D. B. Miracle

"Dislocation Core Structure in Ordered Intermetallic Alloys", by R. Pasianot, D. Farkas and E. J. Savino

phys. stat. sol. (b) **63**, 139 (1974)

Subject classification: 10.4; 21.4

*Theoretical Physics Division, Atomic Energy Research Establishment,  
Harwell, Didcot, Berkshire*

## The Dislocation Loop in an Anisotropic Medium and Its Interaction with an Interstitial Atom

By

N. MEISSNER<sup>1)</sup>, E. J. SAVINO<sup>2)</sup>, J. R. WILLIS<sup>3)</sup>, and R. BULLOUGH

Several explicit expressions for the distortion field of an elliptical dislocation loop in a general anisotropic medium are presented. These are used to evaluate the interaction energy between an interstitial dislocation loop in copper and a nearby interstitial atom. The interstitial atom is represented by either a simple spherical inclusion or by realistic Kanzaki forces for its dumb-bell configuration. The effects of both the microscopic anisotropy of the point defect and of the elastic anisotropy of the body on the form and magnitude of the interaction energy is thus exposed.

Einige explizite Ausdrücke für das Verzerrungsfeld einer elliptischen Versetzungsschleife in einem allgemeinen anisotropen Medium werden mitgeteilt. Diese werden benutzt, um die Wechselwirkungsenergie zwischen einer Zwischengitterversetzungsschleife in Kupfer und einem benachbarten Zwischengitteratom zu berechnen. Das Zwischengitteratom wird entweder durch einen einfachen kugelförmigen Einschluss oder durch realistische Kanzaki-Kräfte für seine Hantelkonfiguration dargestellt. Sowohl der Einfluß der mikroskopischen Anisotropie des Punktdefekts als auch der elastischen Anisotropie des Volumens auf die Form und Größe der Wechselwirkungsenergie wird so dargestellt.

### 1. Introduction

When self-interstitial atoms are created by displacement events in an irradiated material they frequently cluster to form planar aggregates or interstitial dislocation loops. The subsequent interaction between such loops and the remaining or newly created point defects plays a crucial role in the development of radiation damage. Thus, for example, any neutral sinks (such as small gas bubbles) will grow into discernable voids if the interstitial loops have a preferential attraction for interstitials compared with vacancies and the presence of such a preferential attraction forms the basic hypothesis of the present theory of such void growth (see for example [1]). The spatial form and magnitude of this interaction are thus important and are calculated in the present paper. In Section 2 expressions for the displacement and distortion fields around an elliptical dislocation loop in an arbitrary anisotropic body are described and discussed primarily according to their relative ease of numerical evaluation. The local and non-local force models for the split-dumb-bell interstitial are given in Section 3 together with specific Kanzaki forces [2] for copper. Finally in Section 4 the interaction energy between a circular interstitial loop and a self interstitial is

<sup>1)</sup> Attached from the University of Surrey, Guildford.

<sup>2)</sup> On leave from Comision Nacional de Energia Atomica, Departamento de Metalurgia, Argentina; with a Fellowship from Consejo Nacional de Investigaciones Cientificas y Tecnicas, Argentina.

<sup>3)</sup> School of Mathematics, University of Bath.

calculated for copper. Copper was chosen both to demonstrate the effects of fairly high anisotropy and because the point defect forces for the dumb-bell have been previously obtained [3]. A feature of the calculation is that the orientation of the axis of the interstitial is not necessarily constrained to a particular  $\langle 100 \rangle$  direction but is allowed to change its orientation to minimise the total energy of the loop-point defect system. The results confirm the presence of a significant attractive interaction between the interstitial loop and the interstitial atom and thus support the void growth hypothesis and imply a preferential drift flow of the interstitials to such loops. Such flows can be deduced as the orthogonal trajectories to the various iso-interaction energy contours presented.

## 2. The Elastic Field of a Dislocation Loop

The displacement field  $u(x)$  produced by an arbitrary dislocation loop of Burgers vector  $b$  in an anisotropic medium is given by the well known Volterra result [4]:

$$u_i(x) = \int_S b_j \epsilon_{ijk} G_{ir,s}(x' - x) dS_k(x'), \quad (1)$$

where  $S$  is a surface bounded by the dislocation line and the subscripts refer to the Cartesian components of the various quantities;  $C_{ijkl}$  are the elastic moduli,  $G_{ir}(x' - x)$  are the components of the elastic Green's function and the comma notation means partial differentiation. Differentiation of (1) yields the distortion field  $\beta_{ij}(x) = u_{i,j}(x)$  and by a simple application of Stokes's theorem, Mura [5] has shown that this field has the form

$$\beta_{ij}(x) = - \oint_{\partial S} \epsilon_{ijk} b_s C_{qkr} G_{ir,s}(x - x') dx'_q, \quad (2)$$

where the line integral is taken over the dislocation loop, coincident with  $\partial S$  the boundary of the surface  $S$ ,  $x'$  is a point on the loop and  $\epsilon_{ijk}$  is the Cartesian permutation tensor.

By Fourier transformation it can be shown that the Green's function has the explicit integral form

$$G_{ir}(x) = \frac{1}{8\pi^2} \iiint dk_1 dk_2 dk_3 M_{ir}(k) e^{-ik \cdot x}. \quad (3)$$

In (3)

$$M_{ir}(k) = \frac{N_{ir}(k)}{D(k)}, \quad (4)$$

where

$$N_{ir}(k) = (L^{-1}(k))_{ir} D(k), \quad D(k) = |L(k)|, \quad (5)$$

and

$$L_{ir}(k) = C_{imrs} k_m k_s. \quad (6)$$

On substituting (3) into either (1) or (2), the problem of evaluating the elastic field of an arbitrary dislocation loop is thus reduced to that of multiple quadrature. By transforming to spherical coordinates in  $k$ -space and integrating over the radial variable and then projecting from the unit sphere on to an appropriate cylindrical surface, Willis [6] has shown that the distortion field (2) can be written in the more explicit form

$$\beta_{ij}(x) = \frac{1}{4\pi^2} \epsilon_{jql} b_m C_{lmrs} \sum_{N=1}^3 \int_{\partial S} dx'_q \oint_L \frac{k_r^N N_{ir}(k^N)}{u_k \cdot \frac{\partial D}{\partial k_k}(k^N)} [k^N \cdot (x' - x) - 0i]^2 ds \quad (7)$$

where  $\mathbf{n}$  is the loop normal,  $L$  is the unit circle in  $\mathbf{k}$ -space perpendicular to  $\mathbf{n}$  and

$$\mathbf{k}^N = \mathbf{k} + \mathbf{n}Z^N, \quad (8)$$

$\mathbf{k}$  being restricted to lie on  $L$ , and  $Z^N$  ( $N = 1, 2, 3$ ) are the three roots of the sextic equation

$$D(\mathbf{k} + \mathbf{n}Z) = 0 \quad (9)$$

which have positive imaginary parts. If the point  $\mathbf{x}$  lies in the plane of the loop then the summation can be brought inside the integral and the expression somewhat simplified.

When the dislocation loop is elliptical (or circular) the integration over  $L$  can be performed by a procedure analogous to Willis [6], and the displacement field has the form

$$u_i(\mathbf{x}) = -\frac{iab}{2\pi} C_{ijkl} b_j n_k \oint ds f_{ml}(\mathbf{k}) \frac{\mathbf{k}^N \cdot \mathbf{x}}{[a^2(\mathbf{k} \cdot \mathbf{l})^2 + b^2(\mathbf{k} \cdot \mathbf{m})^2]^{3/2}} \times \\ \times \frac{1}{[a^2(\mathbf{k} \cdot \mathbf{l})^2 + b^2(\mathbf{k} \cdot \mathbf{m})^2 - (\mathbf{k}^N \cdot \mathbf{x} + 0i)^2]^{1/2} + f(\mathbf{x} \cdot \mathbf{n})}, \quad (10)$$

where

$$f_{ml}(\mathbf{k}) = \sum_{N=1}^3 \frac{\mathbf{k}_m^N N_l(\mathbf{k}^N)}{n_k \frac{\partial D}{\partial k_k}(\mathbf{k}^N)}; \quad (11)$$

$a$  and  $b$  are the major and minor axis of the ellipse (the minor axis  $b$  should not be confused with the Burger's vector  $\mathbf{b}$ ).  $f(\mathbf{x} \cdot \mathbf{n})$  is a constant for  $\mathbf{x} \cdot \mathbf{n} \neq 0$  with a discontinuity at  $\mathbf{x} \cdot \mathbf{n} = 0$ . The corresponding distortion field was shown by Willis [6] to be

$$\beta_{ij}(\mathbf{x}) = +\frac{iab}{2\pi} b_m C_{lmrs} n_l \oint ds f_{rs}(\mathbf{k}) \frac{1}{[a^2(\mathbf{k} \cdot \mathbf{l})^2 + b^2(\mathbf{k} \cdot \mathbf{m})^2 - (\mathbf{k}^N \cdot \mathbf{x})^2]^{3/2}}. \quad (12)$$

In these expressions  $(\mathbf{l}, \mathbf{m}, \mathbf{n})$  is an orthogonal triad of unit vectors with  $\mathbf{n}$  normal to the loop and  $\mathbf{l}$  and  $\mathbf{m}$  are in the plane of the loop along the major and minor axes, respectively. The numerical evaluation of the integrals in (10) and (12) requires the accurate solution of the sextic (9) at the set of points on  $L$  defined by the overall accuracy of the quadrature. In addition certain unavoidable singularities arising from both degeneracy of the sextic in certain  $\mathbf{k}$  directions and from the small values taken by the irrational denominators in (10) and (12), necessitates special techniques with the quadratures. In particular, when  $\mathbf{x}$  is in the plane of the loop and outside it, the denominators in (10) and (12) become exactly zero for certain  $\mathbf{k}$  and (12) can only be interpreted, in the sense of distributions, as the limit as  $\mathbf{x} \cdot \mathbf{n}$  tends to zero, while (10) exists as an improper Riemann integral.

Expressions for the displacement and distortion fields equivalent to (10) and (12), which avoid having to solve a sextic equation and also are free of singularities when  $\mathbf{x} \cdot \mathbf{n} = 0$ , can be obtained by substituting the Green function (3) into (1), so that

$$u_i(\mathbf{x}) = -\frac{i}{8\pi^3} C_{pkr} b_p n_k \int dS(\mathbf{x}') \iiint d\mathbf{k} M_{ir}(\mathbf{k}) \frac{1}{k} e^{-i\mathbf{k} \cdot (\mathbf{x}' - \mathbf{x})}. \quad (13)$$

It is convenient to reduce  $S$  to a circle by stretching the coordinates along  $\mathbf{l}$  and  $\mathbf{m}$  so that

$$x_i = (a/l_j + b/m_j + n_j) y_j, \quad (14)$$

with inverse

$$y_i = (a^{-1}l_j + b^{-1}m_j + n_j) x_j, \quad (15)$$

so that  $S$  is mapped onto the unit circle  $\mathbf{y} \cdot \mathbf{n} = 0$ ,  $(\mathbf{y} \cdot \mathbf{l})^2 + (\mathbf{y} \cdot \mathbf{m})^2 \leq 1$ . Then, if  $\mathbf{k}'$  is related to  $\mathbf{k}$  by (15), so that

$$\mathbf{k}_i = (a^{-1}l_j + b^{-1}m_j + n_j) \mathbf{k}'_j, \quad (16)$$

(13) reduces to

$$u_i(\mathbf{x}) = \frac{i}{8\pi^3} C_{pkrs} b_p n_k \int dS(\mathbf{y}') \int \int \int dk'_1 dk'_2 dk'_3 M_{ir}(\mathbf{k}) k_r e^{-i\mathbf{k}' \cdot (\mathbf{x} - \mathbf{y})}. \quad (17)$$

Changing to spherical polar coordinates so that

$$dk'_1 dk'_2 dk'_3 = |\mathbf{k}'|^2 d|\mathbf{k}'| d\Omega, \quad (18)$$

where  $d\Omega$  is an element of the unit sphere, and integrating with respect to  $|\mathbf{k}'|$ , using the homogeneity of  $M_{ir}(\mathbf{k})$ , gives

$$u_i(\mathbf{x}) = \frac{i}{8\pi^3} C_{pkrs} b_p n_k \int dS(\mathbf{y}') \int_{|\mathbf{k}'|=1} d\Omega \frac{M_{ir}(\mathbf{k}) k_r}{|\mathbf{k}' \cdot (\mathbf{y}' - \mathbf{y}) - 0i|^2}. \quad (19)$$

The integrals with respect to  $\mathbf{y}'$  may now be evaluated by setting

$$\mathbf{y}' = \lambda(\mathbf{l} \cos \theta + \mathbf{m} \sin \theta) \quad (20)$$

so that

$$dS(\mathbf{y}') = \lambda d\lambda d\theta. \quad (21)$$

The integral with respect to  $\lambda$  is elementary and the integral with respect to  $\theta$  can be evaluated by a method given by Willis [6], to yield the result

$$u_i(\mathbf{x}) = \frac{i}{4\pi^2} C_{pkrs} b_p n_k \int \frac{d\Omega}{|\mathbf{k}'|=1} \frac{M_{ir}(\mathbf{k}) k_r}{[(\mathbf{k}' \cdot \mathbf{l})^2 + (\mathbf{k}' \cdot \mathbf{m})^2]^{1/2}} \times \left\{ 1 - \frac{(\mathbf{k}' \cdot \mathbf{y})}{[(\mathbf{k}' \cdot \mathbf{y} - 0i)^2 + (\mathbf{k}' \cdot \mathbf{l})^2 + (\mathbf{k}' \cdot \mathbf{m})^2]^{1/2}} \right\} \quad (22)$$

and, by differentiating (22) with respect to  $x_j$ , bearing in mind that  $\mathbf{k}' \cdot \mathbf{y} = \mathbf{k} \cdot \mathbf{x}$ ,

$$\beta_{ij}(\mathbf{x}) = \frac{i}{4\pi^2} C_{pkrs} b_p n_k \int \frac{d\Omega k_j M_{ir}(\mathbf{k}) k_r}{[(\mathbf{k}' \cdot \mathbf{y} - 0i)^2 + (\mathbf{k}' \cdot \mathbf{l})^2 + (\mathbf{k}' \cdot \mathbf{m})^2]^{3/2}}. \quad (23)$$

The integrals in (22) and (23) are singular and the singularity in (23) is so severe that the integral exists only in the sense of distributions. For computation, therefore, an alternative is needed and this is developed for the latter below. We project the integral over the unit plane in (23) onto the surface  $C$  of the enveloping cylinder whose generators are parallel to  $\mathbf{y}$ , that is, onto

$$(\mathbf{k}' \wedge \mathbf{y})^2 = 1, \quad (24)$$

where  $\mathbf{y}$  is a unit vector along  $\mathbf{y}$ . The integrand is homogeneous of degree  $-3$  and

$$d\Omega = \frac{dS}{|\mathbf{k}'|^3} \quad (25)$$



so that (23) is unchanged except for the replacement of  $d\Omega$  by  $ds$ . Integration by parts along the generators of  $C$  can be effected by setting

$$\mathbf{k}' = k'_y \hat{y} + \beta[(n + (n \cdot \hat{y}) \hat{y}) + \gamma \hat{y} + n] \quad (26)$$

for instance, in terms of which

$$dS = dk'_y ds, \quad (27)$$

where  $ds$  is an element of arc on the cross-section of  $C$ . Integration by parts twice with respect to  $k'_y$  then gives, after re-arrangement,

$$\begin{aligned} \beta_{ij}(x) = & \frac{1}{4\pi^2} C_{pkrs} b_p n_k y_l y_m \int_C dS \operatorname{Im} \left[ \frac{(k' \cdot y + 0i)^2 - (k' \cdot l)^2 - (k' \cdot m)^2}{\varphi(k')} \right]^{1/2} \times \\ & \times \frac{\partial^2}{\partial k'_l \partial k'_m} (k_j M_{ir}(k) k_s), \end{aligned} \quad (28)$$

where

$$\varphi(k') = [(k' \cdot l - k'_y l_y)^2 + (k' \cdot m - k'_y m_y)^2] |y|^2 - (l_y k' \cdot m - m_y k' \cdot l)^2 \quad (29)$$

in which

$$l_y = l \cdot \hat{y} \quad (30)$$

and so on. The insertion of the "imaginary part" symbol in (28) is justified because the real part of the square root can be shown to make no contribution by a symmetry argument.

Equation (28) is valid so long as  $\varphi(k')$  does not vanish on  $C$  and it may be noted that, in the representation (26),

$$\varphi(k') = (l_y^2 + m_y^2) \{ \gamma^2 |y|^2 - (l_y^2 + m_y^2) \} + \beta^2 n_y^2. \quad (31)$$

Excluding the case  $l_y = m_y = 0$ , and assuming also that  $n_y \neq 0$ , so that  $x$  is not in the plane of the loop,  $\varphi(k')$  vanishes only when  $\gamma = \beta = 0$ , which implies that  $k'$  is not on  $C$ , so long as

$$|y|^2 > l_y^2 + m_y^2. \quad (32)$$

As  $x$  tends to the plane of the loop,  $n_y$  tends to zero and  $\varphi(k')$  vanishes when  $\gamma = 0$ , so that values of  $\beta$  can be found for which  $k'$  lies on  $C$ , for each  $k'_y$ . The formula (28) still applies, however, subject to (32), since the imaginary part of the square root is zero in a neighbourhood of  $\gamma = 0$  and  $n_y = 0$  independently of  $k'_y$ .

Equation (28) thus provides an alternative to (12), for use particularly when  $x$  lies outside the loop, when, in contrast to (12), it contains no singularity. Although the integration by parts could also have been performed using the original variables  $x$  and  $k$ , to yield a formula similar to (28), this alternative in fact contains singularities for some points  $x$  outside the loop so that, from this view point, the transformation (14) is essential. If the loop is circular, with  $a = b$ , (14) is, of course, trivial, and may be accommodated by measuring  $x$  in units of the loop radius,  $a$ . It may be remarked finally that, since the integrand in (28) is homogeneous of degree  $-3$ , the integral can, if desired, be projected back onto the unit sphere without any change of form. The representation (22) of  $u_i(x)$  could be treated similarly.

These distortion fields will be used to discuss the elastic interaction between interstitial atoms and a circular interstitial dislocation loop. However before doing so we must define the representation used to define the interstitial point defect; this we now do.

### 3. The Interstitial in Copper

The configuration of the dumb-bell interstitial for a face centred cubic metal such as copper is depicted schematically in Fig. 1. The forces on the nearest neighbour atoms and their displacements have been calculated by Bullough and Tewary [7] using the method of lattice statics with the perfect lattice Green's function for copper. This Green's function was obtained by fitting directly to the phonon dispersion data [8] and does not require the arbitrary restrictions to short range force constants implicit in the usual Born von Karman analysis

Table 1

The unrelaxed positions  $S^{(k)}$  of the twelve nearest neighbours to the [100] dumb-bell interstitial in copper and their displacements  $d^{(k)}$ . The superscript  $(k)$  is related to the neighbour type in the left hand column. The relaxed atom positions are given by  $S^{(k)} + d^{(k)}$ . Results for interstitials of other  $\langle 100 \rangle$  orientations are obtained by obvious permutation

neighbour $k$	type	unrelaxed atom positions $S^{(k)}$	atom displacements $d^{(k)}$	force in relaxed position $F^{(k)}$ (eV/ $a_0$ )
1	$\pm(110)$	$\pm a_0(110)$	$\pm a_0(0.0282, 0.0945, 0)$	$\pm \frac{1}{\sqrt{8}} (1.5175, 6.6685, 0)$
2	$\pm(110)$	$\pm a_0(110)$	$\pm a_0(0.0282, -0.0945, 0)$	$\pm \frac{1}{\sqrt{8}} (1.5175, -6.6685, 0)$
3	$\pm(101)$	$\pm a_0(101)$	$\pm a_0(0.082, 0, 0.0945)$	$\pm \frac{1}{\sqrt{8}} (1.5175, 0, 6.6685)$
4	$\pm(101)$	$\pm a_0(101)$	$\pm a_0(0.0282, 0, -0.0945)$	$\pm \frac{1}{\sqrt{8}} (1.5175, 0, -6.6685)$
5	$\pm(011)$	$\pm a_0(011)$	$\pm a_0(0, -0.0154, -0.0154)$	$\pm \frac{1}{\sqrt{8}} (0, -0.4383, -0.4383)$
6	$\pm(011)$	$\pm a_0(011)$	$\pm a_0(0, -0.0154, 0.0154)$	$\pm \frac{1}{\sqrt{8}} (0, -0.4383, 0.4383)$

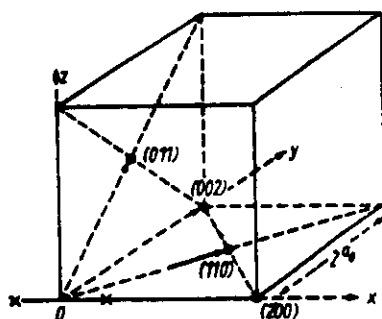


Fig. 1. The four nearest neighbour atoms to the (100) dumb-bell interstitial in an f.c.c. lattice. The dumb-bell atoms are indicated by  $\times - \times$ . 8 (110) neighbours, 4 (011) neighbours, 4 (002) neighbours, 2 (200) neighbours

for the dynamical matrix. The short range interatomic forces required for the actual dumb-bell atoms were derived from the Born-Mayer potential and the analysis of the defect region of the crystal was achieved by the usual matrix partitioning of the defect Green's function with appropriate group theoretical reduction.

The forces and displacements of the 12 nearest neighbour atoms are given in Table 1, where the position vectors of the various atoms are referred to the centre point 0 of the dumb-bell shown in Fig. 1. These quantities will now be used to discuss the interaction energy between such interstitial atoms and a nearby interstitial dislocation loop.

#### 4. The Interaction Energy between the Dislocation Loop and the Interstitial

If the centre of the dumb-bell interstitial is defined by the vector  $\mathbf{x}$  relative to the dislocation loop, then if  $\mathbf{u}^L(\mathbf{x})$  is the displacement field of the loop at that point, the interaction energy between the loop and the point defect is

$$E(\mathbf{x}) = - \sum_{k=1}^6 [u_i^L(\mathbf{x} + \mathbf{S}^{(k)} + \mathbf{d}^{(k)}) F_i^{(k)} - u_i^L(\mathbf{x} - \mathbf{S}^{(k)} - \mathbf{d}^{(k)}) F_i^{(k)}]. \quad (33)$$

This exact expression could be evaluated using the expressions for the loop displacement field given in Section 2. However for all practical purposes the vectors  $\mathbf{S} \pm \mathbf{d}$  will be small compared to  $\mathbf{x}$  and therefore the displacement functions in (27) may be replaced by a Taylor series expansion and the first derivative term only retained; thus we obtain

$$E = -2 \sum_{k=1}^6 \beta_{ij}^L(\mathbf{x}) [S_j^{(k)} + d_j^{(k)}] F_i^{(k)}, \quad (34)$$

where  $\beta_{ij}^L(\mathbf{x})$  is the loop distortion field at the point  $\mathbf{x}$  and the vector components  $S_j^{(k)}$  and  $d_j^{(k)}$  are given in Table 1.

Occasionally an interstitial atom is modelled by a spherical inclusion and we shall refer to this crude representation for comparative purposes only. Thus if  $2a_0(1 + \delta)$  is the inclusion radius and  $\delta$  is the misfit parameter then

$$E(\mathbf{x}) = -\delta \int_{\text{inclusion}} p_{ij}^L(\mathbf{x}) dV, \quad (35)$$

where  $p_{ij}^L(\mathbf{x})$  is the stress field of the loop, related to the distortion field by Hooke's law

$$p_{ij}^L(\mathbf{x}) = C_{ijkl} \beta_{kl}^L(\mathbf{x}) \quad (36)$$

and the integration is over the volume of the spherical "atomic" inclusion. When the body is isotropic the function  $p_{ij}^L(\mathbf{x})$  is harmonic and thus the integral in (35) is simply equal to the value of  $p_{ij}^L$  at the centre of the spherical region multiplied by its volume. Hence

$$E(\mathbf{x}) = -\frac{4}{3} \pi 8a_0^3 \delta p_{ij}^L(\mathbf{x}). \quad (37)$$

The magnitude of  $\delta$  for an interstitial in copper has been estimated by equating the effective strength of the dumb-bell interstitial with the forces in Table 1 to the strength of the spherical inclusion: this yields the results  $\delta = 0.067$  and this value has been used in the isotropic computations. Since the inclusion is small compared with  $|\mathbf{x}|$  (37) is also a good approximation for an anisotropic body. Thus when the interstitial is represented by a simple spherical inclusion (37) may be used to estimate  $E(\mathbf{x})$ : when the body is anisotropic  $p_{ij}^L$  is computed

from (36) using the distortion fields given in Section 2; if, however, the body is isotropic then the Peach-Koehler result [9] is appropriate.

The various expressions for the general distortion field given in Section 2 ((12), (22), (23), and (28)) have been assessed for their ease of numerical evaluation. When the field point is not in the plane of the loop the expression (12) has been found to be the most convenient; for points in the loop plane and outside the loop expression (28) can be used. In practice, however, the requirement of the large number of second derivatives in (28) makes the quadrature in (28) a large numerical task and it was found preferable to use (12) to get values arbitrarily close to the loop plane and to avoid field points precisely on the loop plane. For certain applications, such as the interactions between coplanar loops, it would be necessary to evaluate the distortion fields precisely in the loop plane; in such cases expression (28) must be used and its presentation for such purposes is thus justified. The quadrature in (12) for a circular loop required care to maintain reasonable accuracy and the procedure adopted was a Newton-Cotes adaptive non-recursive scheme [10]. The main advantage of this procedure is that it imposes a convergency condition over the absolute value of the function and not, as is the case of most formulae, over its derivatives; Simpson's method, with a convergency condition on the 4th derivative, requires impossibly short integration steps to achieve the same condition.

It is evident from the form of the integrand in (12) that the integration is not equally convergent in every sub-interval around the loop. If  $r_L = a = b$  is the radius of the loop  $L$ , then, difficult points arise when

$$r_L^2 \approx \text{Re} [(k^N \cdot x)^2] \quad (38)$$

that is when the irrational denominator approaches zero. In addition, however, the derivative of  $D(k)$  in the denominator of  $f_{dr}(k)$  can vanish since in certain symmetry directions the sextic equation degenerates and has double roots. In this situation a spline fitting procedure used in the present Newton-Cotes scheme fails since the function is not sufficiently smooth over the double root. It is thus essential to locate the positions of the double roots before fitting the splines (such double roots are easily located by the routine used to solve the sextic) and then, once located, a spline is fitted outside the point but not across the interval containing it.

The interaction energies between an interstitial atom and a circular interstitial loop were obtained for the loop shown in Fig. 2. The interaction energy was calculated for a grid of points in the two orthogonal planes (112) and (110) passing through the centre of the loop and from this mesh of values contours

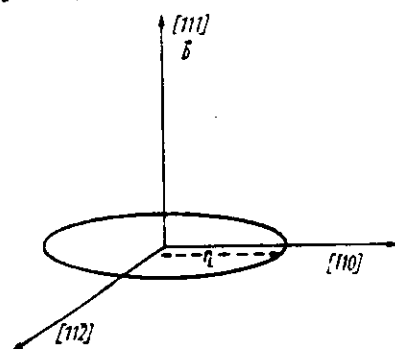


Fig. 2. The circular, pure edge interstitial dislocation loop with Burgers vector  $b = \frac{1}{2}[111]$  used to calculate the interstitial loop interaction in copper

of iso-interaction energies were computed. The results for the various representations are presented in Fig. 3 to 9. In Fig. 3 these contours are shown for the simplest case of an isotropic point defect near the loop in an isotropic body; these energies have been evaluated using (37) with mean values of the shear modulus and Poisson's ratio for copper of  $\mu = 5.46 \times 10^{11}$  dyn/cm<sup>2</sup> and  $\nu = 0.324$  [11]. In this representation there is complete axial symmetry about the loop normal and therefore all planes through the  $\{111\}$  axis of the loop will have identical contours and the complete interaction is thus described by the contours in Fig. 3. In contrast we show in Fig. 4 and 5 the corresponding contours in the  $\{112\}$  plane and the  $\{110\}$  plane respectively for the isotropic body when the interstitial has a dumb-bell configuration (as defined in Section 3) with its axis parallel to the  $[100]$  direction. In this latter situation we see that though the contours in the  $\{112\}$  plane are only quantitatively affected by the microscopic anisotropy of the point defect the corresponding contours in the  $\{110\}$  plane are qualitatively changed by the point defect anisotropy.

The results computed using expression (12) for the full anisotropic body (copper) when the interstitial has the  $\{100\}$  dumb-bell configuration are given in Fig. 6 and 7 for the respective  $\{112\}$  plane and the  $\{110\}$  plane. Finally, there is of course no reason why the axis of the interstitial should remain parallel to a particular direction as it drifts towards (or away from) the loop and we have therefore calculated the interaction energy at each grid point for each of the  $\langle 100 \rangle$  orientations of the interstitial and then adopted the orientation that yields the least total energy at that particular point. These results for the anisotropic body (copper) are presented for the  $\{112\}$  and  $\{110\}$  planes in Fig. 8 and 9, respectively.

Several features of these contours may be noted:

1. Both the microscopic anisotropy of the interstitial and the anisotropy of the body have a marked effect on the form of the interaction energy between the loop and the point defect (compare Fig. 3, 5, and 7 for example).

2. When the complete anisotropy is included the interaction is very complex (Fig. 6 and 7) and when the point defect is allowed to reorientate its axis there can be quite a radical change in the contours; thus the area of attractive interaction is greatly increased in the  $\{112\}$  plane (Fig. 8) compared with the fixed  $[100]$  orientation (Fig. 6).

3. Perhaps the most important observation is that, in general, anisotropy greatly reduces the drift path length that any interstitial would have to take to be captured by the interstitial loop (and thereby increase its size). Thus if we compare the completely isotropic results in Fig. 3 with the contours in Fig. 9 for the anisotropic body and arbitrary orientated dumb-bell we see that at any point in the latter plane the interstitial path (orthogonal trajectory to the iso-interaction energy contours) to the loop is always very short. Whereas in Fig. 3 when the interstitial is located in the volume above the loop area very long drift paths are required. The qualitative conclusion is that anisotropy leads to an enhancement of the efficiency of interstitial capture by an interstitial loop.

4. Finally we note that the attractive interaction energies are large; at a distance of half a loop radius from the perimeter of the loop the energy is still  $\approx 0.05$  eV. In addition the contour lines are compact, thereby implying a high drift velocity and again indicating an important interstitial-loop interaction.

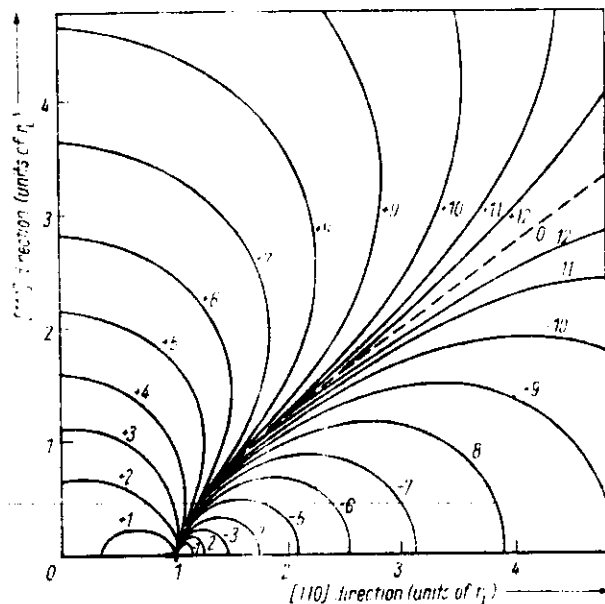


Fig. 3. The iso-interaction energy contours between an isotropic interstitial point defect and the interstitial pure edge dislocation loop in an isotropic body in a quadrant of the (112) plane through the centre of the loop. The cross-section through the perimeter of the loop is indicated by the usual dislocation symbol ( $\perp$ ). The  $\pm n$  ( $n = 1 \dots 12$ ) number on each contour indicate an energy of  $\pm 0.4 \times 21^{\frac{1}{2}}$  eV for that contour; the  $n = 0$  contour (---) means zero interaction energy

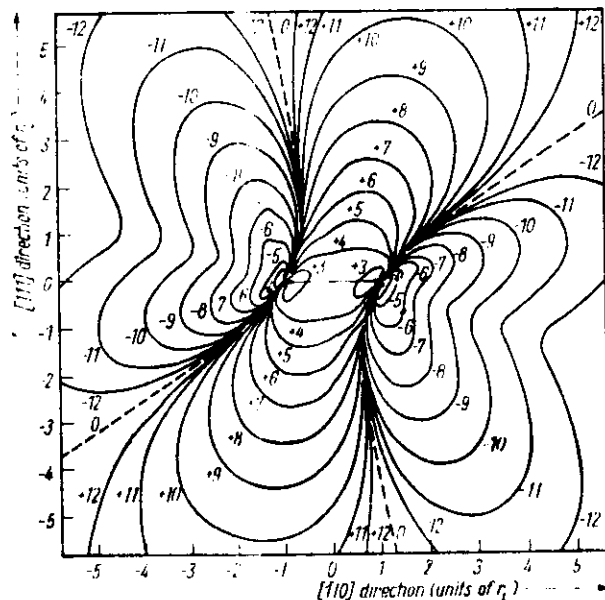


Fig. 4. The iso-interaction energy contours between a [100] dumb-bell interstitial and the interstitial pure edge dislocation loop in an isotropic body in the (112) plane through the centre of the loop. Other details are specified in the caption to Fig. 3

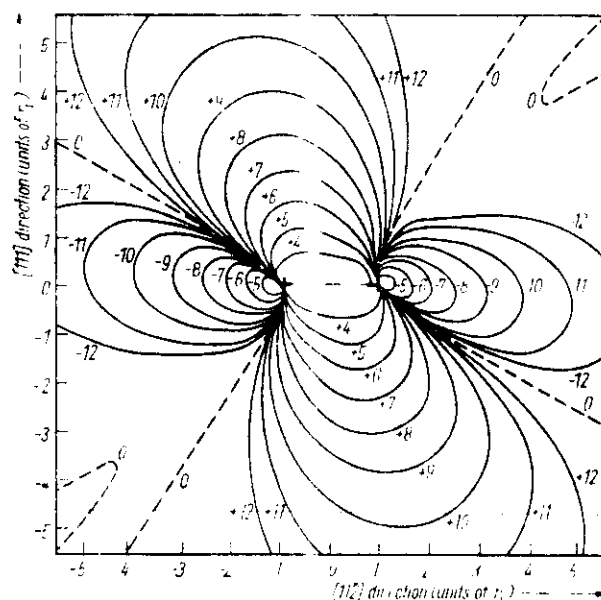


Fig. 5. The iso-interaction energy contours between a  $[100]$  dumb-bell interstitial and the interstitial pure edge dislocation loop in an isotropic body in the  $(110)$  plane through the centre of the loop. Other details are specified in the caption to Fig. 3

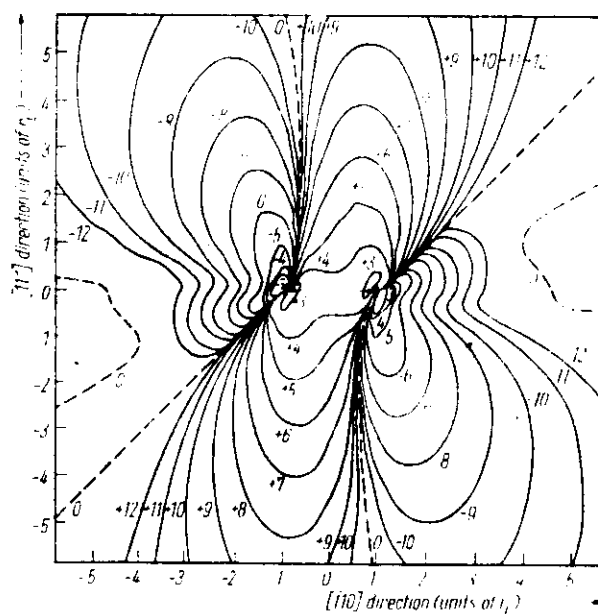


Fig. 6. The iso-interaction energy contours between a  $[100]$  dumb-bell interstitial and the interstitial pure edge dislocation loop in an anisotropic body (copper) in the  $(112)$  plane through the centre of the loop. Other details are specified in the caption to Fig. 3

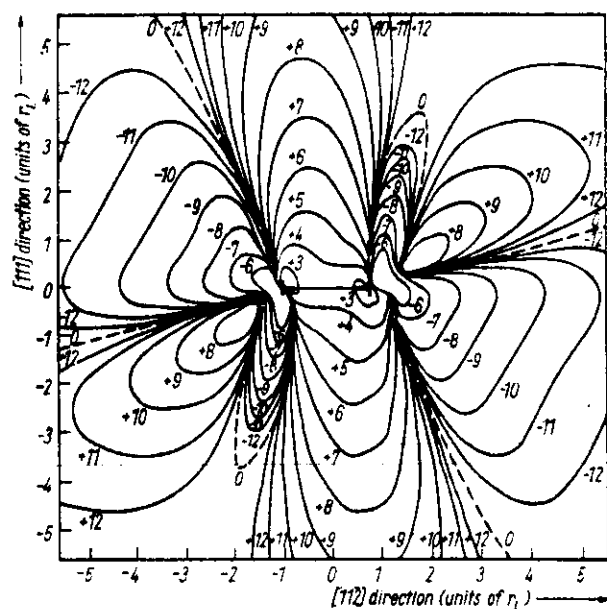


Fig. 7. The iso-interaction energy contours between a  $[100]$  dumb-bell interstitial and the interstitial pure edge dislocation loop in an anisotropic body (copper) in the  $(110)$  plane through the centre of the loop. Other details are specified in the caption to Fig. 3

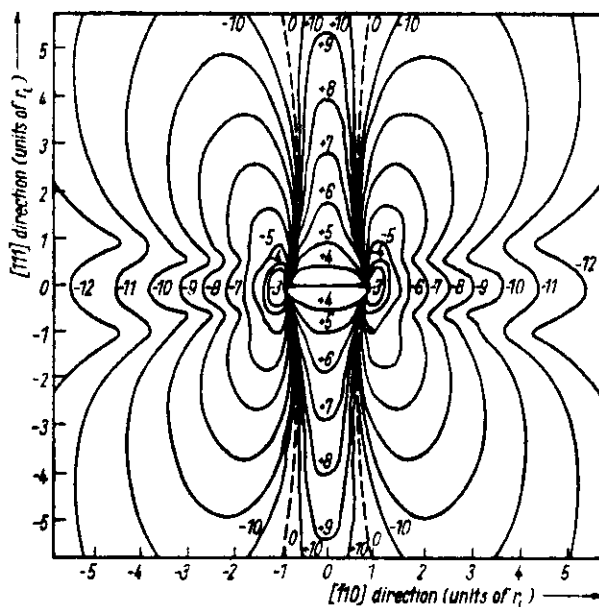


Fig. 8. The iso-interaction energy between an arbitrary  $\langle 100 \rangle$  dumb-bell interstitial and the interstitial pure edge dislocation loop in an anisotropic body (copper) in the  $(112)$  plane through the centre of the loop. Other details are specified in the caption to Fig. 3



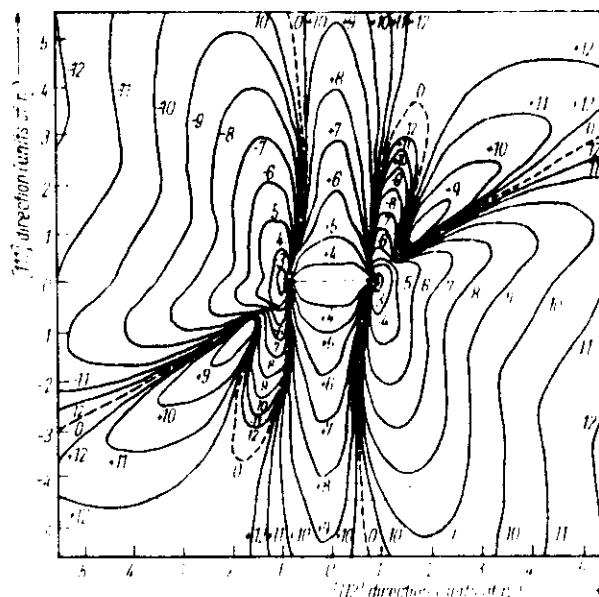


Fig. 9. The iso-interaction energy contours between an arbitrary  $\{100\}$  dumb-bell interstitial and the interstitial pure edge dislocation loop in an anisotropic body (copper) in the  $(110)$  plane through the centre of the loop. Other details are specified in the caption to Fig. 3

### References

- [1] A. D. BRAILSFORD and R. BULLOUGH, *J. nuclear Mater. (Amsterdam)* **44**, 121 (1972).
- [2] H. KANZAKI, *J. Phys. Chem. Solids* **2**, 24 (1957).
- [3] V. K. TEWARY, A.E.R.E. Harwell Rep. T.P. 388 (1969).
- [4] V. VOLTERRA, *Ann. Ecole Normale Supér.* **24**, 401 (1907).
- [5] T. MURA, *Phil. Mag.* **3**, 625 (1963).
- [6] J. R. WILLIS, *Phil. Mag.* **21**, 931 (1970).
- [7] R. BULLOUGH and V. K. TEWARY, *Proc. Conf. Interatomic Potential and Simulation of Lattice Defects*, Ed. P. C. GRUBEN, Plenum Press, London 1972.
- [8] V. K. TEWARY and R. BULLOUGH, *J. Phys. F* **1**, 554 (1971).
- [9] M. O. PEACH and J. S. KOEHLER, *Phys. Rev.* **80**, 436 (1950).
- [10] P. J. DAVIS and P. RABINOVITZ, *Numerical Interaction*, Blaisdell Publ. Co., London 1967.
- [11] J. P. HIRTH and J. LOTHE, *Theory of Dislocations*, McGraw-Hill, New York 1968.

(Received February 19, 1971)



# Lattice static Green function for an hcp lattice

R. Migoni, C. N. Tomé, N. Smetniansky-De Grande, and E. J. Savino

*Departamento de Materiales, Comisión Nacional de Energía Atómica, Buenos Aires, Argentina*

(Received 20 March 1980)

Two different techniques for calculating the lattice distortion under a unitary force, the lattice Green function (GF) at zero frequency, are discussed. One is based on the classical Fourier inversion procedure for a finite number of points within the first Brillouin zone, i.e., periodic boundary conditions are assumed. Explicit formulas which take full profit of the hcp lattice symmetry and allow for a fast and relatively simple calculation of the GF are deduced. An extrapolation procedure is proposed in order to evaluate the GF for a lattice with infinite boundaries. This procedure allows one to differentiate the lattice dispersive contributions to the GF from the continuum ones. A second calculation technique, called semidiscrete, is proposed. This is based on assuming that the atoms located beyond a given distance from the lattice point where a force is applied are displaced like points of an infinite elastic medium under that force. Both techniques are applied to calculate the GF for some points of an hcp lattice held by two different interatomic potentials adjusted to some Mg parameters. The dispersive contribution to the GF values is found to be potential dependent and relatively small.

## I. INTRODUCTION

The displacement field induced by a point defect in a crystal lattice can be calculated via the lattice Green function (GF) as reviewed by Tewary.<sup>1</sup> The defect is simulated by a distribution of effective forces which induce the lattice distortion through harmonic interactions. The method was originally developed by Kanzaki<sup>2</sup> in 1957 for the calculation of the distortion induced by a vacancy. In 1962, Flinn and Maradudin<sup>3</sup> showed that the GF can be calculated only once for the perfect lattice and used for any defect symmetry. Its correct evaluation may be, therefore, of paramount importance. This perfect lattice GF is defined as the lattice response to a unit force at the origin. Then for relatively short distances it should be influenced by the discrete character of the lattice, while at large distances it should converge to its continuum counterpart, the elastic GF.

Defect distortion calculations via the lattice static GF method have been mainly tackled in crystals with cubic symmetry and generally with one atom per unit cell. Analogous calculations in the hexagonal close-packed lattice have been relatively neglected except for the work of Popovic and Carbotte<sup>4</sup> and the more recent ones by Sahoo and Sahu<sup>5</sup> and Tomé *et al.*<sup>6</sup> Popovic and Carbotte<sup>4</sup> developed in their paper the lattice static formalism for that structure and did some calculations for the vacancy configuration. Their approach is similar to Kanzaki's<sup>2</sup> and it does not involve the explicit calculation of the GF. This is calculated by Sahoo and Sahu<sup>5</sup> through the usual method of Fourier inverting the force-constant matrix in a lattice with periodic boundary conditions (BC). However, those authors do not consider the influence of these conditions on the GF

values. Periodicity imposes symmetry restrictions to the GF values at the boundary of the supercell and may also affect the values inside it. Then the convergence of the lattice GF, calculated by imposing those BC, to the elastic one is not certain for any region of the crystal. Schober *et al.*<sup>7</sup> have also shown that, in lattices with cubic symmetry, even for atoms relatively close to the origin and a large periodicity volume, the BC have a significant influence on the calculated values of the GF. Those authors calculate the infinite medium GF by the Gilat-Raubenheimer method of numerical integration over the first Brillouin zone (BZ) and compare their results with previous calculations where periodic boundary conditions were assumed. In this paper the GF is first calculated by the somewhat simpler method of summation over a finite number of points in the BZ. The corresponding direct-space representation would be a set of periodic supercells. The supercell size's influence on the results is systematically studied by varying the number of points included in the summation. The infinite discrete lattice response is obtained by an extrapolation procedure based on some physical insight of the boundaries relevance. This approach allows us to differentiate the contribution to the GF of the boundary conditions from the lattice dispersive one. Previous analysis of this last contribution did not separate it from the first one.<sup>8</sup>

As an alternate approach to the Fourier-inversion method the lattice GF can be calculated in the direct-space representation. This procedure has been applied by Tomé *et al.*<sup>6</sup> for generating the GF used in their defect calculation, and one of the purposes of this work is its detailed deduction. The method is based on imposing, for distances beyond a certain range, the identity be-

tween the lattice and continuum responses, i.e., there the above-mentioned dispersive influence of the lattice is neglected. The resulting response is called "semidiscrete GF." This approximation seems particularly suitable for hcp crystals where the elastic GF can be calculated analytically.<sup>9</sup>

In Sec. II the semidiscrete GF method is described. In Sec. III the Fourier-inversion method is applied for calculating the lattice GF of an hcp lattice with periodic BC. Full advantage of the crystal symmetry is taken in order to reduce the BZ summation to a 24th part of zone. Only simple expressions which are explicitly given in the Appendix have to be evaluated. The BC are discussed in Sec. IV. There an extrapolation procedure is outlined to deduce the GF values of an infinite lattice from a set of GF calculations with periodic BC. In Sec. V numerical values of the GF for Mg obtained by either method discussed above and by using two different potentials are compared among themselves and with the elastic GF. Finally a detailed discussion on the validity of the calculation methods and the previous numerical results is dealt with in Sec. VI.

## II. SEMIDISCRETE GREEN FUNCTION

As was said in the Introduction this calculation method is based on neglecting the lattice dispersive influence on the GF values for atoms located beyond a certain distance from the origin. A finite region in the crystal, hereafter called region *I*, is surrounded by atoms embedded in an infinite elastic medium, region *II*. The GF can be obtained as the ensemble response to a unit force applied at the origin, assumed to be located at the center of *I*. Within the harmonic approximation the displacement  $\vec{u}(n)$  of an atom *n* under a force  $\vec{F}(m)$  applied over *m* must satisfy the equations

$$\begin{pmatrix} \phi_{II} & \phi_{II} \\ \phi_{II} & \phi_{II} \end{pmatrix} \begin{pmatrix} \vec{u}_I \\ \vec{u}_I \end{pmatrix} = \begin{pmatrix} \vec{F}_I \\ \vec{F}_I \end{pmatrix}, \quad (1)$$

where  $\phi_{JK}$  is a  $3N_J \times 3N_K$  matrix composed by the force constants  $\phi_{\alpha\beta}(n_J, n_K)$  which relate the atom  $n_J$  of region *J* with the atom  $n_K$  of *K* ( $J, K = I, II$ ;  $n_I = 1, \dots, N_I$ ;  $n_{II} = N_I + 1, \dots, N_I + N_{II}$ ;  $\alpha, \beta = x, y, z$ ). In Eq. (1),  $N_{II}$  may be effectively infinite.  $\vec{u}_I$  and  $\vec{F}_I$  are the vectors of atomic displacements and forces at the atoms in region *J*. They are composed by three-dimensional vectors  $\vec{u}(n_J)$  and  $\vec{F}(n_J)$ . When a unit force in the  $\alpha$  direction is applied over the atom  $n_I = 1$ , at the origin,

$$F_\alpha(n_I) = \delta_{\alpha\alpha} \delta_{n_I}, \quad (2a)$$

and

$$\vec{F}(n_{II}) = 0,$$

for any  $n_I, n_{II}$ . According to the previous assumptions an atom in *II* displaces by

$$u_\gamma(n_{II}) = G_{\gamma\alpha}^{e1}(n_{II}, 1), \quad (2b)$$

where  $G^{e1}$  stands for elastic GF. The corresponding displacement of an atom in *I* is

$$u_\gamma(n_I) = G_{\gamma\alpha}^{s4}(n_I, 1). \quad (2c)$$

$G^{s4}$  is the semidiscrete GF, which is now defined by Eqs. (1) and (2). Equations (2) are replaced in (1) and the following system of equations is obtained:

$$\phi_{\alpha\gamma}(n_I, n_I') G_{\gamma\alpha}^{s4}(n_I', 1) + \phi_{\alpha\gamma}(n_I, n_{II}) G_{\gamma\alpha}^{e1}(n_{II}, 1) = \delta_{\alpha\alpha} \delta_{n_I}, \quad (3a)$$

$$\phi_{\alpha\gamma}(n_{II}, n_I) G_{\gamma\alpha}^{s4}(n_I, 1) + \phi_{\alpha\gamma}(n_{II}, n_{II}') G_{\gamma\alpha}^{e1}(n_{II}', 1) = 0, \quad (3b)$$

where the Einstein convention applies for summations. Equation (3a) states the equilibrium of forces in region *I* and the semidiscrete GF is obtained from it as

$$G_{\alpha\alpha}^{s4}(n_I', 1) = (\phi_{\alpha\gamma}^{-1})_{\alpha\alpha}(n_I', n_I) [\delta_{\alpha\alpha} \delta_{n_I} - \phi_{\alpha\gamma}(n_I, n_{II}) G_{\gamma\alpha}^{e1}(n_{II}, 1)]. \quad (4)$$

This expression allows for an explicit calculation of  $G^{s4}$  for a lattice held by a relatively short-range potential. Owing to the dispersive character of that lattice, for a finite-size region *I* the elastic GF at the atoms of *II* would not correspond to a configuration with null harmonic forces. This means that Eq. (3b) does not vanish exactly upon replacement of (4) for  $G^{s4}$ . Its value can be identified with forces applied over the atoms of region *II* in order to keep them at the positions imposed by the elastic response. These forces have an inverse dependence with the size of region *I*, and a convergence criterion for the GF calculation can be adopted. The calculated ensemble response,  $G^{s4}$  for region *I* and  $G^{e1}$  for *II*, is accepted as the semidiscrete GF when the misfitting forces calculated by (3b) are some orders of magnitude smaller than unity (i.e., the value of the force applied over atom 1 for calculating the GF).

## III. LATTICE GREEN FUNCTION FOR hcp LATTICES

The lattice-static GF is generated as thoroughly described by Tewary<sup>1</sup> and Schober *et al.*,<sup>7</sup> by Fourier transformation of  $\underline{G}(q) = \underline{\Phi}^{-1}(q)$  over the BZ, i.e., periodic boundary conditions are assumed. The  $6 \times 6$  matrix  $\underline{\Phi}(q)$  is the reciprocal-lattice transform of the force-constant matrix. Both  $\underline{\Phi}(q)$  and  $\underline{G}(q)$  have the symmetry<sup>10</sup>

$$\underline{G} = \begin{pmatrix} \underline{G}(11) & \underline{G}(12) \\ \underline{G}^*(12) & \underline{G}^*(11) \end{pmatrix}, \quad (5)$$

where  $\underline{G}(kk')$  are  $3 \times 3$  submatrices and  $k, k'$  refer to the atomic sites (1 or 2) in the unit cell. Figure

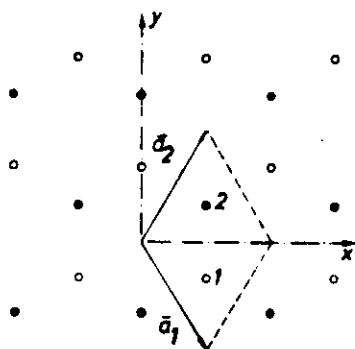


FIG. 1. Schematic representation of the unit cell and hexagonal and Cartesian axes in the hcp lattice. The origin is located at the inversion center of the lattice, the octahedral site. The full circles are drawn as located at a basal plane separated by  $\frac{1}{2}c$  from the one of empty circles.

1 illustrates the arrangement of atoms, the choice of hexagonal and Cartesian coordinate systems, and the atomic sites within the unit cell.  $\underline{G}(11)$  is in general Hermitian but in a model of central forces it is real and symmetric.  $\underline{G}(12)$  is symmetric. Owing to the symmetry of  $\underline{G}$ , only its two upper blocks need to be calculated, which can be readily made from  $\underline{\Phi}(11; q)$  and  $\underline{\Phi}(12; q)$ .

The Fourier transformation of  $\underline{G}(q)$  is performed by summing over one of the 24 equivalent irreducible polyhedra (IP) within the BZ of the hexagonal lattice. For each  $\vec{q}$  the equivalent terms in the whole BZ are obtained by using the symmetry operations ( $\delta$ ) of the lattice. The expression for the GF is then:

$$\underline{G}_{ss}^N(lk, l'k') = \frac{1}{N} \sum_{\text{IP}} \frac{1}{h_s} \Gamma_{ss}(lk, l'k'; \vec{q}), \quad (6)$$

with

$$\Gamma_{ss}(lk, l'k'; \vec{q}) = \sum_{\delta} [\underline{T}(\delta) \underline{G}(\vec{q}) \underline{T}^\dagger(\delta)]_{ss(lk, l'k')} \times e^{i\vec{q} \cdot [\underline{R}(\delta)(\vec{r}(lk) - \vec{r}(l'k'))]}. \quad (7)$$

$l$  denotes the unit cell and  $k$  (1 or 2) the sites in the cell.  $N$  is the total number of points in BZ, i.e., the number of cells in the periodicity volume of the direct space. The sum in Eq. (7) runs over the 24 symmetry operations of the  $D_{6h}$  point group of the hcp lattice. The fact that for boundary points of the IP there is a subgroup of order  $h_s$  of operations that leaves the point invariant is taken into account by dividing by  $h_s$  in Eq. (6) (for  $h_s$  see, e.g., Table XV in Ref. 10).  $\underline{S}$  is the  $3 \times 3$  rotation or reflexion matrix associated with the operation  $\delta$  and  $\underline{T}(\delta)$  is a  $6 \times 6$  transformation matrix which adopts either the form

$$\begin{pmatrix} \underline{S} & 0 \\ 0 & \underline{S} \end{pmatrix} \quad \text{or} \quad \begin{pmatrix} 0 & \underline{S} \\ \underline{S} & 0 \end{pmatrix}.$$

The second one is valid for operations which interchange sublattices 1 and 2. In (6) the contribution of the acoustic branch for  $\vec{q} = 0$  must be excluded because this implies a rigid-lattice translation.  $\underline{\Phi}(\vec{q} = 0)$  must then be diagonalized and only the contribution of the optical eigenvalue included in the summatory  $\sum'$ . Detailed expressions for  $\Gamma_{ss}(lk, l'k'; q)_{q \rightarrow 0}$  are given in the Appendix.

#### IV. BOUNDARY CONDITIONS FOR THE GF CALCULATION

In Secs. II and III the calculation techniques for the GF of an hcp lattice in the semidiscrete and lattice approximations were discussed. This last GF, calculated by Fourier inversion with a finite number of points in the first BZ, gives the response of a lattice supercell with periodic BC, while the first, the semidiscrete GF, gives the response of an effectively infinite crystal where some dispersive lattice contributions are not included in the calculation. In order to compare both techniques, the function calculated with periodic BC must be extrapolated for the case of an infinitely large supercell.

The lattice GF calculated for a supercell of  $N$  unit cells can be written as

$$\underline{G}^N = \underline{G}^{\infty} + \underline{G}^{\text{im}}, \quad (8)$$

where  $\underline{G}^{\infty}$  gives the response of an infinite lattice and  $\underline{G}^{\text{im}}$  the image correction due to the BC. It is illustrative to write the first term in (8) as

$$\underline{G}^{\infty}(\vec{r}, \Omega) = (1/r) [\underline{A}(\Omega) + \underline{B}(\vec{r}, \Omega)], \quad (9)$$

where  $\Omega$  defines the direction of the vector  $\vec{r}$ . This equation is only defined for the discrete set of  $\vec{r}$  vectors corresponding to the lattice positions.  $\underline{A}(\Omega)/r$  is identified with the elastic GF  $\underline{G}^{\text{el}}$  at those positions.  $\underline{B}(\vec{r}, \Omega)$  responds then for the dispersive behavior of  $\underline{G}^{\infty}$  imposed by the discrete character of the lattice and it must vanish for  $r \gg a$  ( $a$  is a lattice parameter).

Imposing periodic BC for a crystal supercell results in cancelling  $\underline{G}^N$  at the symmetry points of the supercell boundary. As an average effect the absolute values of  $\underline{G}^N$  are expected to be in general lower than those of  $\underline{G}^{\infty}$ .  $\underline{G}^{\text{im}}$  must account for this effect and in addition it must decrease for a given  $\vec{r}$  when the size of the supercell is increased. It appears convenient to write

$$\underline{G}^{\text{im}}(\vec{r}, \Omega, R) = -1/R [\underline{A}(\Omega) + \underline{B}'(\vec{r}, \Omega, R)], \quad (10)$$

where  $R$  is the distance from the center to the boundary of the supercell in the  $\Omega$  direction and

the same restrictions for  $(\mathbf{r}, \Omega)$  as in (9) must be imposed. For  $\mathbf{r} = \mathbf{R}$ ,  $\underline{B}'(\mathbf{r}, \Omega, R)$  must be equal to  $\underline{B}(\mathbf{r}, \Omega)$  at the above-mentioned symmetry points and for any  $\mathbf{r}$  this term spreads the influence of the BC on the calculated values of  $\underline{G}^N$ .

Replacing Eqs. (9) and (10) in (8) results in

$$\underline{G}^N(\mathbf{r}, R, \Omega) = \underline{G}^N(\mathbf{r}, \Omega) [I - \underline{f}(\mathbf{r}, \Omega, R) \mathbf{r}/R], \quad (11)$$

where

$$\underline{f}(\mathbf{r}, \Omega, R) = [\underline{A}(\Omega) + \underline{B}(\mathbf{r}, \Omega)]^{-1} [\underline{A}(\Omega) + \underline{B}'(\mathbf{r}, \Omega, R)]. \quad (12)$$

If  $\underline{f}(\mathbf{r}, \Omega, R)$  is nearly independent of  $R$  it is not necessary to know its detailed expression, and (11) provides the clue of how to extrapolate from the calculated  $\underline{G}^N(\mathbf{r}, R, \Omega)$  the corresponding  $\underline{G}^N(\mathbf{r}, \Omega)$ . In Sec. V it is shown for Mg that  $\underline{f}$  is independent of  $R$ , to a very good approximation, for  $R > 3r$  (note that it still depends on  $\mathbf{r}$ ).

BC may also affect the semidiscrete GF. In its calculation, the dispersive terms outside a given region  $I$  are imposed to cancel out. As a result of this cancellation spurious contributions to the calculated function may arise. Though these contributions must be small because of the convergence criterion proposed in Sec. II, they are not null and we shall see in the next section that some lattice symmetries are affected.

## V. NUMERICAL RESULTS

The semidiscrete and lattice GF for some near-neighbor atoms of the Mg lattice are calculated by using the two interatomic potentials discussed by Tomé *et al.*<sup>6</sup> One of them is a spline-fit pair potential fitted to some Mg parameters. It is relatively short ranged and holds in equilibrium an hcp lattice with a  $c/a$  ratio corresponding to a rigid-sphere packing. The other potential has been deduced from Appapillai and Heine<sup>11</sup> optimized pseudopotentials and the experimental  $c/a$  ratio is adopted for the calculations.

For the calculations of  $\underline{G}^N$  a hexagonal mesh of  $\bar{Q}$  points is generated with an equal number  $L$  of intervals from the center to the boundaries of the BZ in  $x$  and  $z$  directions. The main axes of the reciprocal lattice are oriented parallel to the direct-lattice ones (see Fig. 1). The corresponding periodicity volume in direct space is hexagonal with basal and axial edges of dimensions  $R_s = La$  and  $R_c = 2Lc$ , respectively. The number of unit cells included in this region is  $N = 6L^3$ . We shall first try to extrapolate from the calculated values  $\underline{G}^N$  of the lattice GF for different supercell sizes the corresponding function for an infinite lattice— $\underline{G}^N$ . Equations (9) and (11) suggest a convenient way of processing the  $\underline{G}^N$  values for obtaining  $\underline{G}^N$

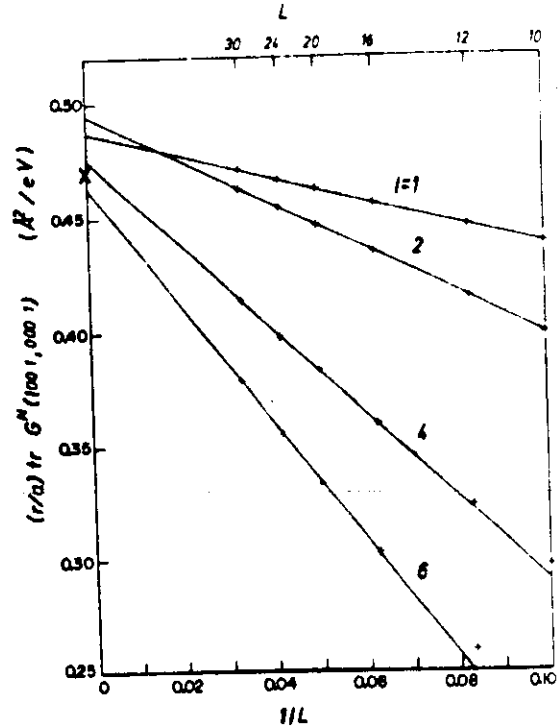


FIG. 2.  $(r/a) \text{tr} G^N(1001, 0001)$  vs  $1/L$ , where  $r$  is the distance between atoms  $(2001)$  and  $(0001)$ ;  $\underline{G}^N$  is the GF calculated for  $N$  cells in the first BZ;  $L$  is the maximum value of  $l$  within the supercell in the direct space.  $\times$  is the value of  $(r/a) \text{tr} G^N(1001, 0001)$ .

as follows: The behavior of  $\underline{r} \underline{G}^N(\mathbf{r}, \Omega, R)$  as a function of  $1/R$ , for a fixed  $\bar{\mathbf{r}}$ , is analyzed for different number  $N$  of cells in the first BZ. For all the points and potentials studied and as far as  $R > 3r$ , we found the function  $\underline{r} \underline{G}^N$  to be linear in  $1/R$ . As an example, in Fig. 2  $\underline{r} \underline{G}^N(\mathbf{r}, \Omega, R)$  is plotted against  $1/L$  for atoms located along the  $[100]$  direction (see Fig. 1). This linear dependence indicates that the function  $\underline{f}(\mathbf{r}, R, \Omega)$  in Eq. (11) is independent of  $R$  for  $R > 3r$ . This result is very useful, since it can be used to extrapolate, from the calculated values to the lattice GF,  $\underline{G}^N$ , for different number of cells  $N$ , the corresponding  $\underline{G}^N$ . The numerical results reported hereafter show that  $\underline{G}^N$  can be obtained by this method for points near the origin with very good precision. Also in Fig. 2, the extrapolated values,  $\underline{r} \underline{G}^N$ , can be compared with the corresponding values for the elastic GF,  $\underline{r} \underline{G}^{\text{el}} = \underline{r} \underline{A}(\Omega)$ , constant for every neighbor in a given direction and indicated by a cross at  $1/L = 0$ . The observed differences correspond to the dispersive term  $\underline{B}(\mathbf{r}, \Omega)$  in Eq. (9). It is apparent that the dispersive influence of the lattice attenuates oscillatory with increasing  $\mathbf{r}$ . However, in the example shown in Fig. 2, this term does not seem to influence the  $\underline{G}^N$  function values by more than

TABLE I. Some values of the lattice GF calculated by two different interatomic potentials fitted to Mg parameters are compared with the long-wave, elastic values.

$(lk)$	$\alpha\beta$	$G_{\alpha\beta}(lk,01)$ ( $\text{\AA}^3/\text{eV}$ )					
		Empirical potential		$G^{\text{el}}$	Pseudopotential		$G^{\text{el}}$
		$G^{\text{e}}$	$G^{\text{sd}}$		$G^{\text{e}}$	$G^{\text{sd}}$	
(0001)	xx	0.5723	0.5686		0.6009	0.6038	
	zz	0.5699	0.5663		0.6100	0.6115	
(0002)	xx	0.1233	0.1242	0.1327	0.1171	0.1278	0.1510
	yy	0.1672	0.1640	0.1538	0.1760	0.1779	0.1764
	zz	0.1936	0.1907	0.1806	0.2060	0.2094	0.2278
	yz	0.0404	0.0391 <sup>a</sup>	0.0291	0.0423	0.0405 <sup>a</sup>	0.0382
	xy						
(1001)	xx	0.2253	0.2216	0.2093	0.2297	0.2343	0.2442
	yy	0.1332	0.1327	0.1329	0.1357	0.1409	0.1541
	zz	0.1282	0.1271	0.1303	0.1316	0.1354	0.1550
	xy	0.0012	0.0021 <sup>b</sup>	0	0.0029	0.0059 <sup>b</sup>	0
	yx	-0.0012	-0.0001 <sup>b</sup>	0	-0.0029	0.0000 <sup>b</sup>	0
	yz						
(1002)	xx	0.1049	0.1067	0.1180	0.0962	0.1082	0.1367
	yy	0.0986	0.0976	0.1022	0.1022	0.1063	0.1177
	zz	0.1024	0.1018	0.1084	0.1001	0.1061	0.1302
	yz	0.0066	0.0069 <sup>a</sup>	0.0100	0.0014	0.0019	0.0133
	xy						
	xx	0.0115	0.0120 <sup>a</sup>	0.0174	0.0023	0.0033	0.0230
	yy						
	xy	0.0054	0.0079	0.0137	-0.0052	0.0016	0.0165
	yx						
	yz						
(0011)	xx	0.0823	0.0803	0.1229	0.0847	0.0884	0.1411
	yy						
	zz	0.1246	0.1243	0.1337	0.1444	0.1503	0.1600

<sup>a</sup>Value averaged between  $G_{\alpha\beta}^{\text{sd}}$  and  $G_{\beta\alpha}^{\text{sd}}$ , which should be equal by lattice-symmetry considerations.

<sup>b</sup>The lattice symmetry imposes  $G_{xy}^{\text{sd}} = -G_{yx}^{\text{sd}}$  in this case.

4%. On the other side, the image term  $G^{\text{im}}$  in (8) may greatly influence the calculated GF,  $G^{\text{N}}$ , with periodic BC. For example, in Fig. 2 it can be seen that for the (400,1) atom, even when 162 000 cells in the whole BZ ( $L=30$ ) are used for calculating  $G^{\text{N}}$ , the term  $G^{\text{im}}$  accounts for over 10% of the calculated  $G^{\text{N}}$  value.

In Table I the values of the GF calculated in the semidiscrete approximation are compared with the extrapolated values for  $G^{\text{e}}$ . The semidiscrete GF,  $G^{\text{sd}}$ , is calculated for a spherical region of 21 atoms around the origin and the two above-mentioned potentials are used for the calculations. The previously mentioned loss of some symmetry operations for the semidiscrete  $G^{\text{sd}}$  can be inferred from the values marked with a or b in the table. They do not fulfill the symmetry imposed by the group symmetry at that point. For the sake of comparison the elastic GF,  $G^{\text{el}}$ , is also reported. This function has been calculated by using Kröner's formulation<sup>9</sup> for the corresponding atomic positions with respect to the origin. The elastic con-

stants deduced from the corresponding potential in the long-wave limit<sup>12</sup> are used for the calculation (see Ref. 6 for their values). On going from the elastic into either of the lattice GF's ( $G^{\text{e}}$  or  $G^{\text{sd}}$ ), it can be seen that the difference among the elastic constants used for the two  $G^{\text{el}}$  calculations has a larger influence on the values reported for that function than the dispersive term.

## VI. SUMMARY AND CONCLUSIONS

In this paper two different calculation methods for the lattice GF have been proposed. The already classical Fourier-inversion method in a lattice with periodic BC (Ref. 1) is applied to an hcp structure and explicit formulas for the calculation, which take full profit of the lattice symmetry, are deduced. As discussed by Schober *et al.*,<sup>7</sup> the influence of the periodic BC on the calculated GF values may be quite important. This problem is discussed and an extrapolation procedure is proposed to calculate the GF for an

infinite lattice. This procedure has been proved to be successful in obtaining that function for the hcp lattice. However, as it is based on quite general ideas about the GF dependence on BC, we think it likely to be applied with comparable success to any lattice symmetry. The observed differences between the GF calculated for finite-size supercells and infinite ones may be very large as shown in Fig. 2. This fact has been suggested previously for cubic structures by Schober *et al.*<sup>7</sup> but has not been taken into account in some calculations reported for defects in the hcp lattice.<sup>5</sup> The relative importance of this error in the reported defect configuration is reduced by the defect symmetry as discussed by Laciana *et al.*<sup>13</sup> but it is still important when very few points in the first BZ are included in the GF calculation.<sup>14</sup>

The semidiscrete method is appealing in the sense that it does not rely on Fourier-inversion and extrapolation procedures for obtaining an infinite-lattice GF. However, some lattice dispersive contributions are neglected by this method and a set of spurious small forces are imposed on the boundary between regions I and II. The latter may cause some problems if the numerical values are to satisfy all the lattice symmetries.

The very close agreement of the  $\bar{G}''$  values reported in Table I with the  $\bar{G}^{ad}$  values shows these problems as being only minor, and it is a further test on the validity of the extrapolation procedure used for calculating  $\bar{G}''$ .

From Table I, by comparing the lattice GF values,  $\bar{G}''$  and  $\bar{G}^{ad}$ , with the elastic response,  $\bar{G}^{el}$ , calculated for the same position, it can be concluded that (a) even for the atom's first neighbors to the origin, the dispersive contribution is within a 20% of their main GF values, (b) its magnitude depends on the interatomic potential used for the calculation, and (c) a comparable dispersion in values is obtained when the  $\bar{G}^{el}$ , calculated with the elastic constants deduced from either potential in the long-wave limit, are compared among themselves.

#### ACKNOWLEDGMENTS

This work was supported in part by the Comisión de Investigaciones Científicas de la Provincia de Buenos Aires (CIC), Argentina. One of us (C.N.T.) acknowledges support from the Comisión de Investigaciones Científica de la Provincia de Buenos Aires (CIC), Argentina.

#### APPENDIX

Some symmetry operations of the  $D_{6h}$  point group interchange blocks of the  $\bar{G}$  matrix corresponding to the two different sublattices. As it can be seen in Eq. (5), this is equivalent to a complex conjugation. Therefore it is possible to handle the  $3 \times 3$  blocks of  $\bar{G}$  separately instead of the  $6 \times 6$  matrices involved in Eq. (7). In addition, since inversion is an element of the group and interchange sublattices, there are twelve lattice-interchanging operations. Their corresponding terms in Eq. (7) are just complex conjugates of the ones associated with the 12 remaining operations. Equation (7) is thus written as

$$\Gamma_{ss}(lk, l'k'; q) = 2 \sum_{\bar{S}}^{12} \{ \bar{G}'_{ss}(kk', \bar{S}\bar{q}) \cos(\bar{S}\bar{q} \cdot \bar{r}) - \bar{G}''_{ss}(kk', \bar{S}\bar{q}) \sin(\bar{S}\bar{q} \cdot \bar{r}) \}, \quad (A1)$$

where  $\bar{G}'(kk', \bar{S}\bar{q})$  and  $\bar{G}''(kk', \bar{S}\bar{q})$  are, respectively, the real and imaginary parts of  $SG(kk', \bar{q})S'$ . Here the  $\bar{S}$  are the twelve operations that do not interchange sublattices (see Tables XIV and XVI in Ref. 10).  $\bar{r}$  stands in Eq. (A1) for  $\bar{r}(lk) - \bar{r}(l'k')$ .

Performing the operations  $\bar{S}$  with the Cartesian axes located as shown in Fig. 1, the following expressions are obtained:

$$\begin{aligned} \Gamma_{xx} &= 2C_s \{ A_{xx}(4C_s C_s + [CC]_x) + 3A_{yy}[CC]_x + 2\sqrt{3}A_{yz}[CC]_x \\ &\quad - B_{xx}(4C_s S_s + [CS]_x) - 3B_{yy}[CS]_x - \sqrt{3}(B_{yz} + B_{zy})[CS]_x \}, \\ \Gamma_{yy} &= 2C_s \{ A_{yy}(4C_s C_s + [CC]_y) + 3A_{xx}[CC]_y - 2\sqrt{3}A_{yz}[CC]_y \\ &\quad - B_{yy}(4C_s S_s + [CS]_y) - 3B_{xx}[CS]_y + \sqrt{3}(B_{yz} + B_{zy})[CS]_y \}, \\ \Gamma_{zz} &= 8C_s \{ A_{zz}(C_s C_s + [CC]_z) - B_{zz}(C_s S_s + [CS]_z) \}, \\ \Gamma_{xy} &= 4S_s \{ A_{xx}([CS]_x - 2C_s S_s) - \sqrt{3}A_{yy}[CS]_x + B_{xx}([CC]_x - 2C_s C_s) - \sqrt{3}B_{yy}[CC]_x \}, \\ \Gamma_{xz} &= 4S_s \{ -A_{xx}([SC]_x + 2S_s C_s) - \sqrt{3}A_{yy}[SC]_x + B_{xx}([SS]_x + 2S_s S_s) + \sqrt{3}B_{yy}[SS]_x \}, \\ \Gamma_{yz} &= 2C_s \{ \sqrt{3}(A_{yy} - A_{xx})[SS]_x - 2A_{yy}(2S_s S_s + [SS]_x) \\ &\quad + \sqrt{3}(B_{yy} - B_{xx})[SC]_x - 4B_{yy}S_s C_s + (B_{yy} - 3B_{xx})[SC]_x \}, \end{aligned} \quad (A2)$$



where  $A$  is the real and  $B$  the imaginary part of  $G(q)$ . We omit the indices  $(kk')$  in  $A_{\alpha\beta}$  and  $B_{\alpha\beta}$ , and  $(lk, l'k')$  in  $\Gamma_{\alpha\beta}$ . For  $k \neq k'$ ,  $\Gamma_{\alpha\beta} = \Gamma_{\beta\alpha}$ , but for  $k = k'$ ,  $\Gamma_{\alpha\beta}$  differs from  $\Gamma_{\beta\alpha}$  in the signs of the  $B$  coefficients. The  $C_\alpha$  and  $S_\alpha$  are cosines and sines of  $q_\alpha [r_\alpha(lk) - r_\alpha(l'k')]$ . We also define

$$\begin{aligned} [CC]_\alpha &= C'_\alpha C'_\alpha \pm C''_\alpha C''_\alpha, \\ [CS]_\alpha &= C'_\alpha S'_\alpha \pm C''_\alpha S''_\alpha, \text{ etc.}, \end{aligned} \quad (\text{A3})$$

where the prime or double prime corresponds to the replacement of  $q_\alpha$  in the argument of cosines and sines by the corresponding component of the vector

$$\vec{q}' = (\frac{1}{2}q_x + \frac{1}{2}\sqrt{3}q_y, \frac{1}{2}\sqrt{3}q_x - \frac{1}{2}q_y, q_z),$$

or

$$\vec{q}'' = (-\frac{1}{2}q_x + \frac{1}{2}\sqrt{3}q_y, \frac{1}{2}\sqrt{3}q_x + \frac{1}{2}q_y, q_z),$$

respectively.

<sup>1</sup>V. K. Tewary, *Adv. Phys.* **22**, 757 (1973).

<sup>2</sup>H. Kanzaki, *J. Phys. Chem. Solids* **2**, 24 (1957).

<sup>3</sup>P. A. Flinn and A. A. Maradudin, *Ann. Phys. (N.Y.)* **18**, 81 (1962).

<sup>4</sup>Z. D. Popovic and J. P. Carbotte, *J. Phys. F* **4**, 1599 (1974).

<sup>5</sup>D. Sahoo and H. K. Sahu, *Phys. Rev. B* **18**, 6727 (1978); **18**, 6738 (1978).

<sup>6</sup>C. N. Tomé, A. M. Monti, and E. J. Savino, *Phys. Status Solidi B* **92**, 323 (1979).

<sup>7</sup>H. R. Schober, M. Monstoller, and P. H. Dederichs, *Phys. Status Solidi B* **64**, 173 (1974).

<sup>8</sup>R. Bullough, M. J. Norgett, and S. Weeb, *J. Phys. F* **1**,

345 (1971).

<sup>9</sup>E. Kröner, *Z. Phys.* **136**, 402 (1953).

<sup>10</sup>J. L. Warren, *Rev. Mod. Phys.* **40**, 38 (1968).

<sup>11</sup>M. Appapillai and V. Heine, *Tech. Report No. 5 SST/77*, 1972 Univ. Cambridge, 1972 (unpublished).

<sup>12</sup>M. Born and K. Huang, *The Dynamical Theory of Crystal Lattices* (Clarendon, Oxford, 1954).

<sup>13</sup>C. E. Laciana, A. J. Podraza, and E. J. Savino, *Phys. Status Solidi A* **45**, 315 (1978).

<sup>14</sup>By repeating the Sahoo and Sahu calculations we conclude that they are committing an error of less than 1% by using their calculated GF in calculating the vacancy configuration.



**Atomic Displacements Around Nitrogen  
Interstitial Impurities in Ta and Nb**

*S. Rao, E.J. Savino, and C.R. Houska*



---

Reprinted from Materials Research Society Symposium Proceedings Volume 82, *Characterization of Defects in Materials*, R.W. Siegel, R. Sinclair, and J.R. Weertman, editors.

# ATOMIC DISPLACEMENTS AROUND NITROGEN INTERSTITIAL IMPURITIES IN Ta AND Nb

S. Rao, E. J. Savino\* and C. E. Houeka  
Department of Materials Engineering  
Virginia Polytechnic Institute and State University  
Blacksburg, VA 24061

## ABSTRACT

The core as well as the long range elastic displacements around N octahedral interstitial atoms in Ta and Nb are modelled using the Green Function - Kanzaki force method. The theoretical calculations are compared with experimental attenuation factor and diffuse scattering data, reported in the literature, for both N in Nb and N in Ta [1,2,3]. It is shown that a third neighbor radial Kanzaki force model is needed to explain the experimental findings, and the long range elastic displacement field is non-spherical.

## INTRODUCTION

Gas interstitials like N,C when incorporated into transition metals like Fe,Nb,Ta are known to occupy the octahedral interstitial sites of the BCC lattice [2]. As a result, a distortion around the octahedral interstitial sites is induced. The displacement of the lattice atoms can be calculated using the Green function - Kanzaki force method [4]. At large distances from the defect, the displacements are well described by the elastic Green's function, solution for an equivalent force source. The displacement of the lattice atoms causes an attenuation and shift of the Bragg peaks as well as diffuse scattering [5]. Experimental attenuation factor and diffuse scattering data for N in Nb and N in Ta have been reported in the literature [1,2,3]. These data are used here to theoretically determine the core and long range displacements about the interstitial defect. It is shown that a third neighbor radial Kanzaki force model (three force model, from now on) explains the experimental findings much better than a second neighbor (two force) model, in agreement with the conclusions of Dosch and Peiel for N in Nb [2]. For both N in Nb and N in Ta, the second and third neighbor forces are about one-third the first in absolute value and are opposite in sign.

## THEORY

In the Green function model, the displacement of Nb or Ta atoms around a N octahedral interstitial can be written as [4]

$$u_i^m = \sum_{j,n} G_{ij}^{m-n} f_j^n \quad (1)$$

where  $u_i^m$  ( $i = 1,2,3$ ) are the cartesian components of displacement of the  $m^{th}$  lattice atom,  $G_{ij}^{m-n}$  is the Green function matrix of the ideal lattice and  $f_j^n$  are the cartesian components of the Kanzaki forces acting on the  $n^{th}$  lattice atom. The Kanzaki forces are not only due to the defect-lattice interaction but they also model any anharmonicity in the host lattice displacement field. For points far away from the defect eq. (1) must converge to the harmonic, elastic solution:

$$u_i(r) = G_{ij,k}^{el}(r) P_{jk} \quad (2)$$

\*On leave from Departamento de Materiales, Comision Nacional de Energia Atomica, Argentina.

where  $G^{el}$  stands for the elastic Green function. In eq. (2) the derivative of the elastic Green function is taken with respect to the  $k$  direction ( $k = \partial/\partial x_k$ ) and  $P_{jk}$  is the dipole tensor for a set of forces at the origin. It can be seen that eq. (1) converges to (2) if the dipole tensor is related to the Kanzaki forces by:

$$\sum_n r_i^n f_j^n = P_{ij} \quad (3)$$

where  $r_i^n$  are the cartesian components of the vector joining the interstitial site with the  $n^{th}$  lattice atom. The dipole tensor for a (100) oriented N octahedral interstitial in a BCC lattice can be written as

$$\begin{bmatrix} P_{11} & 0 & 0 \\ 0 & P_{22} & 0 \\ 0 & 0 & P_{22} \end{bmatrix}. \text{ If radial Kanzaki forces are assumed to act only on the first and second neighboring shells around the N defect, then } P_{11} = f^{(1)} a \text{ and } P_{22} = \sqrt{2} f^{(2)} a. \text{ For a three force model, } P_{11} = f^{(1)} a + \frac{4f^{(3)}}{\sqrt{5}} a \text{ and } P_{22} = \sqrt{2} f^{(2)} a + \frac{8f^{(3)}}{\sqrt{5}} a.$$

The attenuation factor for the Bragg reflections,  $e^{-2M}$ , can be written as [4]

$$-2M = \ln \langle e^{-2M} \rangle = C \langle \sum_n (1 - \cos 2\pi H \cdot u^n) \rangle \quad (4)$$

where the sum goes over all lattice atoms around a N interstitial,  $H = h_1 b_1 + h_2 b_2 + h_3 b_3$ , is a vector in reciprocal space expressed in terms of reciprocal lattice vectors. For the calculation, an average must be taken over the three possible octahedral interstitial orientations (001, 010, 100). The macroscopic volume change due to a concentration,  $C$ , of N defects is equal to [5]

$$\frac{\Delta V}{V} = C \langle \frac{P_{11}}{V_c (C_{11} + 2C_{12})} \rangle \quad (5)$$

where  $C_{11}$  and  $C_{12}$  are the elastic constants of the cubic crystal,  $V$  is the volume of one lattice atom. Since all three types of interstitial sites are occupied with equal probability, the average lattice expansion along the (100), (010) and (001) directions are equal and the lattice remains cubic. For a small defect concentration a simple expression for diffuse scattering has been obtained as [5]

$$\begin{aligned} I_{Diff}(H) &= CN_0 \langle |G(H)|^2 \rangle \\ G(H) &= f_H^D + f_H \sum_{n=1}^L \exp(i2\pi H \cdot R^n) \{ \exp(i2\pi H \cdot u^n) - 1 - i2\pi H \cdot u^n \} \\ &\quad + i2\pi H \cdot u(q) \end{aligned} \quad (6)$$

$$2\pi H = 2\pi H_0 + q$$

The summation is taken over the first few  $L$  shells around a N defect. Beyond the  $L^{th}$  shell, the exponential function  $\exp(i2\pi H \cdot u^n)$  can be expanded in a Taylor series as a function of the displacements,  $\exp(i2\pi H \cdot u^n) = 1 + i2\pi H \cdot u^n$ . In the third term of eq. (6),  $u(q)$  is the Fourier transform of the displacement field.  $H_0$  locates the  $(hkl)$  point and  $q$  is a vector in the first Brillouin zone.  $f_H^D$  and  $f_H$  are the atomic scattering factor of the defect and the lattice atoms, respectively.  $N_0$  is the total no of lattice atoms. At low  $q$  values,  $G(H)$  is determined by the elastic displacement field far away from the defect (Huang scattering). At large  $q$  values,  $G(H)$  is determined by the local displacements around the interstitial. The exponent of the attenuation factor,  $2M$ , can be rewritten as

$$2M = C \langle |G_q(H_0)|^2 \rangle$$

$$= C \frac{1}{N_1} \langle \sum_{n=1}^{N_1} |G_{q_n}(H_0)|^2 \rangle \quad (7a)$$

where

$$G_{q_n}(H_0) = \sum_{m=1}^L \exp(iq_n \cdot R^m) (\exp(i2\pi H_0 \cdot \nu^m) - 1 - i2\pi H_0 \cdot \nu^m) + i2\pi H_0 \cdot \nu(q_n) \quad (7b)$$

The summation in eq. (7a) is taken over  $N_1$  equally spaced wave vectors in the first Brillouin zone.

#### RESULTS AND DISCUSSION

In Fig. 1, experimental attenuation factor data for N in Nb (1.4 at%) obtained by Dosch and Peisl [1],  $2M/C$ , are plotted against  $h_1^2$  and compared with theoretical values, obtained from both the 2-force and 3-force Kanzaki models. Radial forces,  $f_1$ ,  $f_2$ , and  $f_3$ , used in the calculations for both the 2-force and 3-force models are given in Table 1. Both the 2-force and 3-force models satisfy eq. (2), unlike the 3-force model proposed by Dosch and Peisl for N in Nb [2]. Equation (6) which is exact, was used to derive the theoretical attenuation factor values. In the papers by Dosch and Peisl [1] and Metzger and Trautmann [3], it is assumed that the displacements beyond the 4th or 6th neighboring shell have spherical symmetry. This assumption results in a significant underestimate of the contribution to  $2M$  from these outer shells.

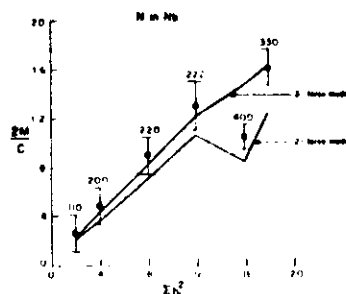


FIG.1. Experimental attenuation factor data (a) [Ref. 1], plotted against  $h_1^2$  and compared with calculations for the 2-force and 3-force models, for N in Nb.  $h_1$ ,  $h_2$  and  $h_3$  are the Miller indices of the Bragg reflection.

The displacements of the Nb atoms up to the (005) shell around a N interstitial were calculated using eq. (1) and the eighth neighbor force constant matrix for Nb [6]. The summation in eq. (7b) was taken up to the (005) shell. Beyond the (005) shell,  $\exp(i2\pi H_0 \cdot \nu^m) = 1 + i2\pi H_0 \cdot \nu^m$ , and the contribution from these shells is included in the term  $i2\pi H_0 \cdot \nu(q)$  of eq. (7b). The Fourier transform of the displacement field was calculated by taking the Kanzaki forces in reciprocal space and multiplying those by the Fourier transform of the Green function [5]. The transform of the Green function is directly obtained by inversion of the reciprocal space force constant matrix [4]. All lattice atoms were included in the determination

Table I. Radial Kanzaki forces,  $f^{(1)}$ ,  $f^{(2)}$  and  $f^{(3)}$ , in  $\text{eV-Å}^{-1}$ , acting on the first three neighboring shells around a W interstitial in Nb (a) and Ta (b), for the 2-force and 3-force models.

	Nb (a)		Ta (b)	
	2-force	3-force	2-force	3-force
$f^{(1)}$	3.88	2.45	4.98	3.18
$f^{(2)}$	0.94	-1.08	1.53	-1.01
$f^{(3)}$	0.00	0.80	0.00	1.00

of  $2M$  by an analytical extrapolation,  $M \rightarrow \infty$ , in eq. (7a). From Fig. 1, it is clear that the 2-force model predicts  $2M$  values that are approximately 20% less than the experimental values whereas the 3-force model of Table I, agrees with the experimental data quite well. In Figs. (2), (3) and (4), experimental neutron diffuse scattering data [2] in absolute units ( $I_D$  in  $\text{cm}^{-1}$ ), at three different regions in reciprocal space (Table I of Ref. [2]), are compared with the theoretical values obtained from eq. (6), using both the 2-force and 3-force models. The neutron scattering lengths of N and Nb,  $f_N^D$  and  $f_{Nb}^D$ , were taken as  $0.94$  and  $0.71 \times 10^{-12}$  cm, respectively [7]. Once again, the 3-force model fits the experimental data much better than the 2-force model, though in Fig. 4, both the 2-force and 3-force models do not provide a quantitative fitting of the experimental data. The absolute values of the core displacements calculated from the 3-force model, are normally larger than those obtained from the 2-force model, and therefore predicts larger attenuation factor and diffuse scattering values. The elastic displacement field far away from the defect remains the same for both the models, since they are determined only by the dipole tensor of the defect and the elastic constants of Nb (eq. 2).

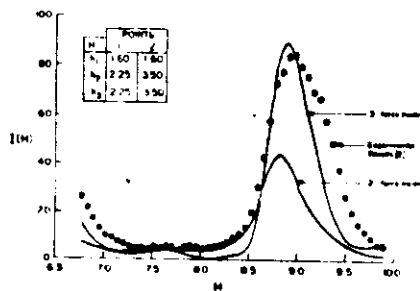


FIG.2. Experimental scattering along a line in reciprocal space connecting points 1 and 2 (see insert) as compared with theoretical calculations from 2 and 3-force models for N in Nb, in absolute units.

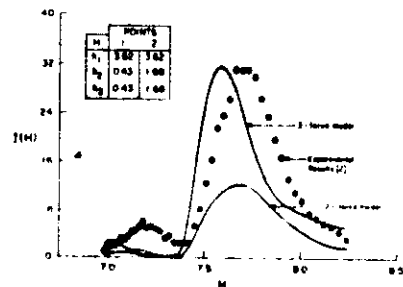


FIG.3. Experimental scattering along a line in reciprocal space connecting points 1 and 2 (see insert) as compared with theoretical calculations from 2 and 3-force models for N in Nb, in absolute units.

Figure 5 is a polar plot of the locus of elastic displacements of constant magnitude. The tetragonal axis is denoted by  $c$ , and the direction of the displacements are indicated at intervals of  $10^\circ$ . The elastic displacements were calculated using eq. (2). The effect of cubic anisotropy in the elastic constants of  $Mb$  on the long range displacements is shown by plotting the displacements based on substituting average isotropic elastic Green function which is identical to results developed by Keating and Coland [8]. All of our results clearly demonstrate that the long range field does not exhibit spherical symmetry.

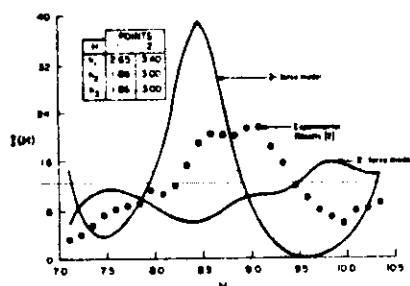


FIG.4. Experimental scattering along a line in reciprocal space connecting points 1 and 2 (see insert) as compared with theoretical calculations from 2 and 3-force models for  $N$  in  $Mb$ , in absolute units.

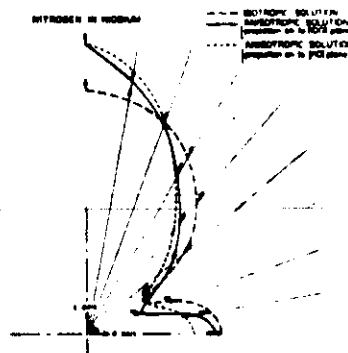


FIG.5. Locus of elastic displacements of constant magnitude for  $N$  in  $Mb$ .

In Fig. 6, the experimental  $2M/C$  values for  $N$  in  $Ta$ , up to 1.8 at  $X$ , obtained by Metzger and Trautmann [3], are plotted and compared with the values predicted by the 2-force and 3-force models of Table I. The dipole tensor for  $N$  in  $Ta$  is taken from reference [9] and the seventh neighbor force constant matrix for  $Ta$ , from reference [10]. Figure 6 shows that the 3-force model fits the experimental data very closely whereas the 2-force model is inconsistent with the data. Experimental data beyond the (660) reflection was not used in the fitting procedure since the change in the mean square thermal displacements of  $Ta$  atoms around a  $N$  defect effect the experimental data significantly at these large  $h$  values [11,3]. At this point, the thermal parameters are not available for the extended calculations. The magnitude of the core displacements predicted by the 3-force model are normally larger than that predicted by the 2-force model, as in the case of  $N$  in  $Mb$ .

Figure 7 is a polar plot of the locus of the elastic displacements far away from the defect, of constant magnitude, for  $N$  in  $Ta$ . This has the same non-spherical appearance as for  $N$  in  $Mb$ ; however, at 100Å (along  $c$ ) the displacement for  $N$  in  $Mb$  is  $1.5 \times 10^{-4}$  Å while for  $N$  in  $Ta$  it is only  $0.37 \times 10^{-4}$  Å.



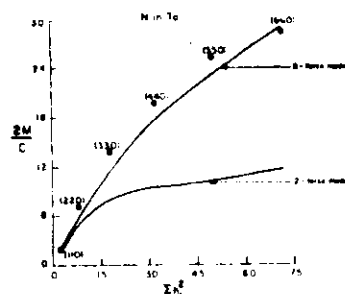


FIG. 6. Experimental attenuation factor data, (e) [Ref. 3]  $2M/C$ , plotted against  $h_1^2$  and compared with calculations for the 2-force and 3-force models, for N in Ta.  $h_1$ ,  $h_2$ , and  $h_3$  are the Miller Indices of the Bragg reflection.

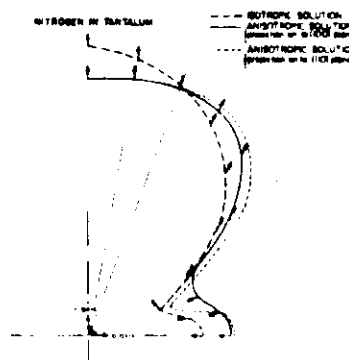


FIG. 7. Locus of elastic displacements of constant magnitude for N in Ta.

#### CONCLUSIONS

In conclusion, we want to stress the following points:

(i) Attenuation factor and diffuse scattering measurements have been used to quantitatively determine the atomic displacements at the core of an interstitial impurity. This has been shown convincingly for the systems, N in Nb and N in Ta, in this paper.

(ii) The Green function - Kanzaki force method seems to be appropriate for theoretically modeling the core as well as the long range displacement field about an interstitial defect in a bcc lattice.

(iii) Both the two force and three force Kanzaki models provide the same long range displacement field. As a result, they predict the same amount of average lattice expansion, Huang scattering and internal friction. To distinguish between models giving different core displacements it is necessary to measure the very weak diffuse scattering between reflections and (or) small oscillations or trends in the attenuation factor.

#### ACKNOWLEDGEMENTS

This research was sponsored by Office of Naval Research Grant No. N00014-83-K-0750, P00004.

#### REFERENCES

1. R. Dosch, J. Peisl and B. Dorner, Z. Phys. B, **61**, 479 (1985).
2. R. Dosch and J. Peisl, Phys. Rev. B, **32**, 623 (1985).

3. T. H. Metzger and C. Trautmann, *Z. Phys. B*, **62**, 63 (1985).
4. V. K. Tewary, *J. Phys. F*: **3**, 1515 (1973).
5. P. H. Dederichs, *J. Phys. F*: **3**, 471 (1973).
6. Y. Nakagawa and A. D. B. Woods, *Phys. Rev. Lett.*, **11**, 271 (1963).
7. International Tables for X-Ray Crystallography, Vol. IV (Kynoch Press, Birmingham, 1974), p. 270.
8. D. T. Keating and A. M. Goland, *Acta Metall.*, **15**, 1865 (1967).
9. J. Bucholz, *Proc. Int. Meeting on Hydrogen in Metals*, Julich, Vol. II, p. 544.
10. A. D. B. Woods, *Phys. Rev.*, **136A**, 781 (1964).
11. M. A. Krivoglas, *Theory of X-Ray and Thermal Neutron Scattering by Real Crystals* (Plenum, New York, 1969), p. 241.

## The morphology of planar vacancy aggregates in copper

E J Savino† and R C Perrin

Theoretical Physics Division, Building 8.9, AERE, Harwell, Oxfordshire, UK

Received 13 May 1974

**Abstract.** The morphology of small planar aggregates of vacancies in copper has been investigated by computer simulation. Clusters of as few as six vacancies have been found to collapse to form loops or stacking fault tetrahedra. This is consistent with the theory that vacancy loops are nucleated directly in individual neutron cascades. Larger triangular clusters collapse and dissociate to form stacking fault tetrahedra by the Silcox-Hirsch mechanism. Hexagonal clusters show a more complex rhombohedral relaxation with extensive dissociation of the Frank dislocation on {111} planes. This may explain the fine structure observed recently in electron microscope images of vacancy loops in copper.

### 1. Introduction

Vacancy clusters formed after ion bombardment or neutron irradiation of copper are generally thought to be in the form of Frank loops. The characteristic black white electron microscope images obtained from these defects under dynamical two beam conditions show some fine structure and this has led Wilson and Hirsch (1972) and Haussermann (1972) to suggest that the Frank dislocation has to some extent dissociated to form a Shockley partial and a stair rod dislocation by a reaction of the type

$$\frac{1}{3}[111] = \frac{1}{6}[112] + \frac{1}{6}[110].$$

However, this interpretation of the experimental images is purely qualitative since no calculations have yet been performed of the images to be expected from such a dissociated defect. Also, it is possible for complicated images to arise from simple edge loops under certain imaging conditions. Nevertheless, as has been pointed out by Eyre (1973) in a recent review, the concept of the loops undergoing partial dissociation may explain their unexpected stability in post irradiation annealing experiments at temperatures as high as 773 K (Makin and Manthorpe 1963, Barry and Eyre 1970) at which they should have lifetimes of the order of a second or less.

Since the calculation of the elastic displacement field of the dissociated loop which would reproduce the observed images is extremely difficult a more profitable approach would seem to be that of using the technique of computer simulation to obtain the atomic structure of the vacancy Frank loop and then determining the relevant electron microscope images. This process has recently been successfully applied to the straight Shockley dislocation by Perrin and Savino (1973) who calculated weak beam electron microscope images of the dissociated edge dislocation using the atomic coordinates

† Present address: Comisión Nacional de Energía Atómica, Departamento de Metalurgia, Argentina.

calculated by Norgett *et al* (1972). A comparison of these images with the experimental observations of Stobbs and Sworn (1972) and Cockayne *et al* (1972) enabled Perrin and Savino to predict that the stacking fault energy was at least  $70 \text{ erg cm}^{-2}$ . A feature of the calculations of Norgett *et al* was the introduction of the rapidly convergent conjugate gradients method for minimization, with a consequent reduction in the computation time required to obtain the equilibrium defect configuration. This has made it feasible to simulate regions of crystal large enough to study the morphology of small loops. We have, therefore, as a first step calculated the atomic configuration of small hexagonal and triangular vacancy loops in copper.

## 2. Simulation model

Since we were concerned with planar vacancy aggregates on  $\{111\}$  planes the simulated region of copper crystal was chosen to be a rectangular prism with a  $\{111\}$  face. The other faces of the prism were bounded by appropriate  $\{112\}$  and  $\{110\}$  planes. The dimensions of this region in which the atoms were free to move was generally taken to be 37  $\{112\}$  planes, 26  $\{111\}$  planes and 33  $\{110\}$  planes except in the case of the triangular cluster of 36 vacancies when, because of the pattern of relaxation, the corresponding numbers of planes were 50 by 22 by 28. Thus the free region always consisted of over 5000 atoms. To stabilize this assembly and to enable all the interactions of the free atoms to be evaluated this region was surrounded by a boundary region of fixed atoms, the width of which was equal to the range of the potential.

The atoms were arranged initially on a perfect fcc lattice with the observed copper lattice spacing. The vacancy defect was then created by removing the appropriate atoms from the central  $\{111\}$  plane, except that the large triangular loop was placed on the  $\{111\}$  plane at one third of the distance from the boundary in anticipation of the expected tetrahedral relaxation. The boundary atoms were normally constrained to remain in their perfect lattice positions but for the hexagonal aggregate they were given the elastic displacements due to a circular loop of radius equal to the side of the hexagon. These displacements which were appropriate to an anisotropic medium were evaluated in the manner described by Meissner *et al* (1973).

The atoms were assumed to interact via the potential function constructed by Englert *et al* (1970) to fit certain copper parameters including a stacking fault energy of  $70 \text{ erg cm}^{-2}$ . This potential has been successfully used in calculations related to straight dislocations in copper by Norgett *et al* (1972) and Perrin *et al* (1972). The equilibrium configuration of the defect was then obtained by minimizing the total energy of the crystal using the method of conjugate gradients (Fletcher and Reeves 1964). Since this method requires the evaluation of first derivatives of the function to be minimized (ie forces) it is designed to guarantee convergence to the minimum of a quadratic function in  $N$  steps where  $N$  is the number of variables. In practice we found that even with over 15 000 variables we obtained the energy minimum to the required accuracy with about 150 function evaluations.

## 3. Results

### 3.1. Collapse of planar clusters

Before examining in detail the morphology of the largest triangular and hexagonal loops

which we can simulate within our model we have determined the minimum size of planar cluster which can be considered to have collapsed into a loop. To do this we have removed successively increasing numbers of vacancies in the most compact configurations from the central (111) plane of the crystal and calculated the relaxation of the adjacent (111) planes towards this cluster. In table 1 we display the separation of the (111) planes on either side of the defect plane as a function of the number of vacancies. The separation

Table 1. Separation of (111) planes on either side of a planar vacancy cluster as a function of the number of vacancies

No of vacancies	Shape	Separation
1	—	1.136
2	—	1.088
3	Triangle	1.109
4	Rhombus	0.782
6	Triangle	0.594
7	Hexagon	0.614
10	Triangle	0.592
36	Triangle	0.586
37	Hexagon	0.599

has been calculated at the centre of the defect by interpolating between the coordinates of surrounding atoms where necessary. For a fully collapsed perfect loop this separation should be the (111) interplanar spacing of  $0.577a$  ( $a$  is the copper lattice parameter) but the presence of the intrinsic fault prevents collapse to this value. The separation between (111) planes across an infinite stacking fault has been found by Englert *et al* using the same interatomic potential to be  $0.59a$ . Thus from table 1 we see that a triangular cluster of six vacancies can be considered to have totally collapsed, the resulting configuration being an embryonic stacking fault tetrahedron which can presumably then grow, in the presence of an excess vacancy concentration, by the de Jong-Koehler mechanism (de Jong and Koehler 1963).

An estimate of the number of vacancies at which a (111) platelet should collapse to a Frank loop can be made using elasticity theory and surface energy arguments (see, for example, Sigler and Kuhlmann-Wilsdorf 1966, Bullough and Perrin 1969) and indicate that in copper such a collapse should occur at about five vacancies. While such calculations cannot be accurate for clusters of this size it is encouraging that they are in agreement with the simulation results.

Johnson (1967) has considered the collapse of vacancy clusters in nickel using an interatomic potential similar to the Englert copper potential but of shorter range. He studied clusters of up to 30 vacancies and although complete collapse to a loop was not achieved extrapolation of the results indicated that collapse should occur at about 180 vacancies. However, Johnson's calculations also show that the elastic energies of perfect and Frank loops are lower than the energy of (111) platelets with more than about 16 vacancies. It is not clear exactly why Johnson's platelets do not collapse at this point but do in the present calculations. The longer range of the Englert potential, which includes a repulsive second neighbour interaction, would appear to be the most significant difference in the calculations. We should perhaps stress that we have considered only vacancy clusters which have already aggregated on a particular (111) plane and have not

studied the relative stabilities of compact three dimensional clusters (voids) and loops, as has been done by Johnson. These calculations gave the void as the stable configuration for small numbers of vacancies but did not take account of the fact that a significant part of the vacancy formation energy comes from terms which depend on the volume. Including this in the calculations would obviously increase the likelihood of the loop being the stable form.

The fact that relatively small numbers of vacancies do appear to collapse to a loop or stacking fault tetrahedron is of great significance to the nucleation of such defects in an irradiation environment. In particular, it is highly likely that vacancy loops would be formed by individual neutron cascades since calculations of displacement cascades (see, for example, Beeler 1966) show that they contain compact vacancy clusters of this size.

### 3.2. Triangular clusters

A planar cluster in the form of an equilateral triangle with  $\langle 110 \rangle$  sides of approximately 20 Å was formed by removing 36 atoms from a  $\{111\}$  plane. The crystal was then allowed to relax to its equilibrium configuration under the influence of the interatomic potential and a complete collapse of the vacancy cluster was observed. This was achieved by the atoms inside the tetrahedron defined by the  $\{111\}$  planes which pass through the sides

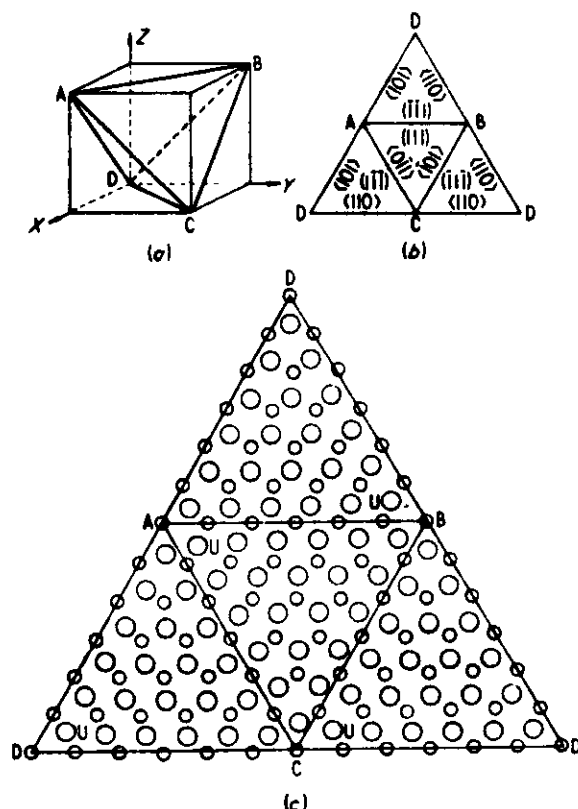


Figure 1. Atomic configuration of a stacking fault tetrahedron. (a) Orientation of tetrahedron relative to cube axes. (b) Expanded view of tetrahedron. (c) Atomic configuration of the tetrahedron faces. The large circles correspond to atoms outside the tetrahedron, the smaller to atoms in the faces. Unfaulting can be seen at points marked U.

of the triangle of vacancies dropping down to eliminate the vacancy cluster. This motion which creates a tetrahedron of stacking fault can also be thought of as the passage of  $\frac{1}{6}\langle 112 \rangle$  Shockley partials across three faces of the tetrahedron, leaving  $\frac{1}{6}\langle 110 \rangle$  stair rod dislocations at the edges—the Silcox-Hirsch (1959) mechanism. Such stacking fault tetrahedra have been observed in copper after electron irradiation (Ipohorski and Spring 1970).

Figure 1(a) shows schematically the tetrahedron resulting from the triangle of vacancies ABC on a  $\{111\}$  plane. Figure 1(c) displays the atomic structure of the stacking fault across the four faces of tetrahedron expanded as in figure 1(b). The centres of the circles represent the positions of the atoms on the  $\{111\}$  planes on either side of the stacking fault. The small circles are on the inside and the large circles are on the  $\{111\}$  planes bounding the tetrahedron on the outside. It can be seen from figure 1(c) that a certain degree of unfaulinging has taken place, particularly from one corner of each face marked U in the figure. This is perhaps more clearly seen in figure 2 which shows the planes

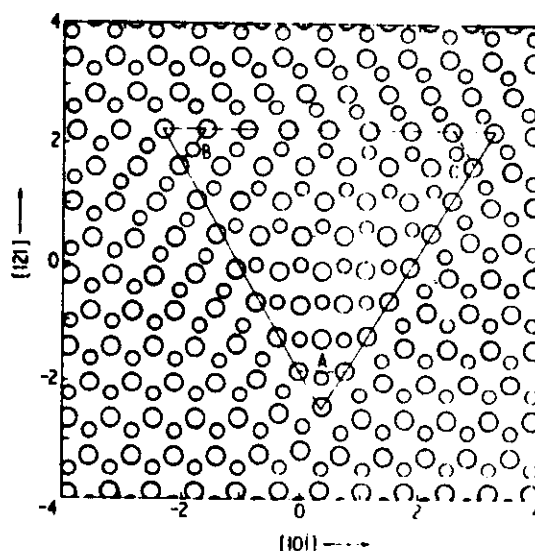


Figure 2. Atomic configuration of face ABC of the tetrahedron showing unfauling at A, partial unfauling at B and complete faulting at C.

bounding the face ABC in full. Clearly, the atom at C is in the almost perfectly faulted position while the atom at A has unfaulted to near its perfect lattice position. (Compare the relative positions of the atoms with the perfect lattice in the corner of the figure.) The atom at B is in an intermediate position midway between the faulted and unfaulted positions. The other three faces of the tetrahedron all show exactly the same features. This apparent unfauling is caused by distortion of the atom planes outside the tetrahedron whereas the passage of a Shockley partial would correspond to movement of atoms on the  $\{111\}$  planes which have vacancies in them. It seems likely that this unfauling is a dislocation core effect associated with the changed coordination of the atoms in the edges and corners of the tetrahedron and may not be so significant for larger tetrahedra.

### 3.3. Hexagonal Frank loops

**3.3.1. Morphology.** We have created vacancy Frank loops in the form of hexagons with  $\langle 110 \rangle$  sides and diameters of 18 and 23 Å by removing 37 and 61 atoms respectively from the central (111) plane of the crystal. In contrast to the triangular loop there was considerable relaxation on both sides of the loop plane. As the relaxation of the larger loop might be constrained by the boundary we shall describe only the smaller one in detail although there was no qualitative difference between them.

The principal relaxations were found to take place on the  $\{111\}$  planes which pass through the edges of the hexagonal loop, the relaxation being on opposite sides of the loop plane for alternate edges of the hexagon. The intersection of these planes defines a rhomboid enclosing the original loop, as shown in figure 3(a). Since the most likely mode

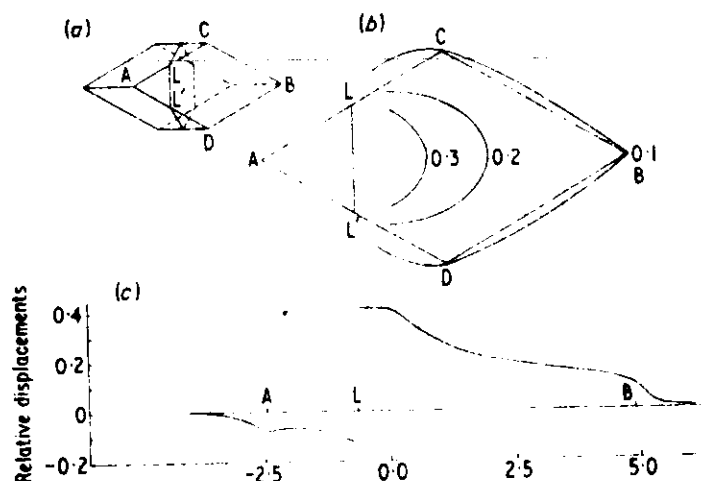


Figure 3. (a) Rhomboid defined by the  $\{111\}$  planes which pass through the edges of a (111) hexagonal loop. (b) Contour plot of the relative displacement of atoms in the  $\langle 112 \rangle$  direction AB across the face ACBD. (c) The displacements of figure 3(b) plotted along AB. (All distances are expressed in units of the lattice parameter.)

of dissociation of the Frank dislocation bounding the loop is to split into a stair rod and a  $\frac{1}{6}\langle 112 \rangle$  Shockley partial dislocation we have plotted in figure 3(b) contours of the displacement in the  $\langle 112 \rangle$  direction BA of atoms on the inside of the face ACBD relative to the atoms in the (111) plane just outside. The complete passage of a  $\frac{1}{6}\langle 112 \rangle$  Shockley partial causes a relative displacement of  $0.41a$ , so the observed relaxations can be thought of as the incomplete passage of a Shockley partial across the face ACBD, with the 0.2 contour as the centre of a rather wide Shockley dislocation. This extreme width of the partial dislocation has been found previously in simulations of the straight dislocation in copper (Perrin *et al* 1972, Norgett *et al* 1973). It can be clearly seen in figure 3(c) where the  $\langle 112 \rangle$  displacement along the line AB has been plotted. The displacement can be seen to approach the full Shockley partial value of  $0.41a$  at the loop L. On the other side of the loop the displacement of  $0.14a$  corresponds to the projection of the  $\frac{1}{6}\langle 110 \rangle$  stair rod dislocation on to the  $\langle 112 \rangle$  direction. The apparent extension of the sessile stair rod towards A is caused by the Shockley partial dislocations on the intersecting



(111) planes through ALC and AL'D in figure 3(a). The displacements associated with these dislocations show up on the face ALL' because of the small number of atoms in this region.

**3.3.2. Interaction with point defects.** A simple estimate of the energy of interaction between this loop configuration and point defects can be obtained by treating the interstitial as a spherical inclusion or the vacancy as a centre of dilatation in an isotropic medium. The interaction energy at a point  $x$  is then given by

$$E(x) = -\frac{4}{3}\pi a^3 \delta P_{ii}(x)$$

where  $a$  is the lattice parameter,  $\delta$  the strength of the inclusion or dilatation and  $P_{ii}(x)$  is the stress field of the loop. The strength  $\delta$  for the interstitial has been given by Meissner *et al* (1973) as 0.067 and for the vacancy by Bullough and Hardy (1968) as 0.022. The  $P_{ii}$  have been evaluated from the atomic coordinates and contours of isointeraction energies have been computed. These are displayed in figure 4 for a (110) section through the centre of the loop. The contour values are for the interstitial interaction with the vacancy value given in brackets. The lines AB, BC, CD trace the intersection of the projection plane with the {111} planes which pass through the loop edges. It can be clearly seen that interstitials are strongly attracted to regions such as BC where these {111} planes intersect and also to the region immediately above and below the loops. Vacancies

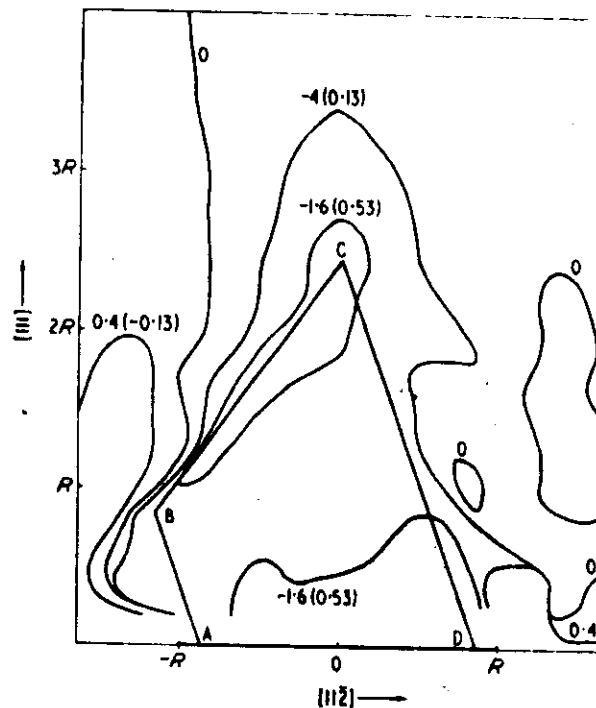


Figure 4. Isoenergy contours for the interaction of point defects with a hexagonal vacancy loop. The contour values, in eV, are for the interstitial interaction with the vacancy value in brackets.

are only attracted towards the loop in the loop plane which should promote the growth of the loop configuration rather than any three dimensional form. Figure 5 shows the equivalent contours for the interaction of point defects with the anisotropic elastic

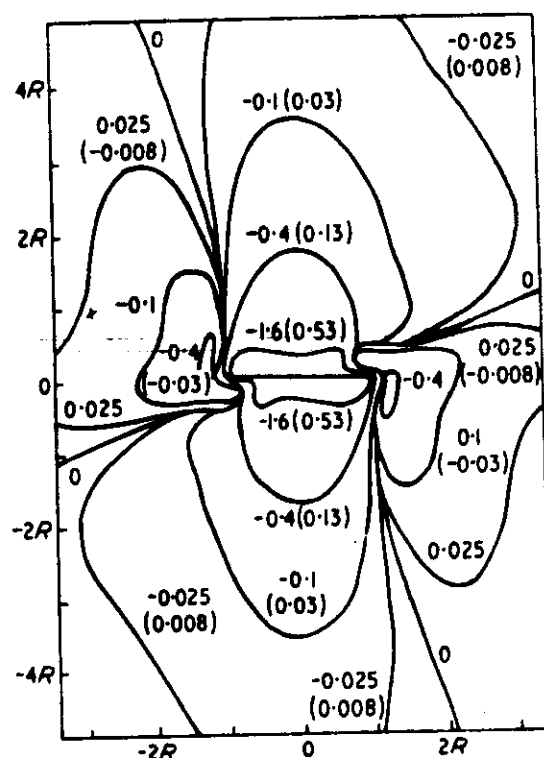


Figure 5. Isoenergy contours for the interaction of point defects with the anisotropic elastic displacement field around a circular vacancy loop. The contour values, in eV, are for the interstitial interaction with the vacancy value in brackets.

displacement field around a circular vacancy loop. A comparison of figures 4 and 5 demonstrates the considerable change in loop morphology which exists between the atomic and elastic models.

#### 4. Conclusions

Using the interatomic potential of Englert *et al* to define the interaction between atoms, it has been shown by computer simulation that in copper (111) planar vacancy aggregates of as few as six vacancies readily collapse to more stable configurations. Since many clusters of this size are formed in the cascades produced by neutron irradiation it gives support to the current theory that vacancy loops are nucleated in individual neutron spiker.

A triangular cluster of vacancies on a (111) plane relaxes via the Silcox-Hirsch mechanism to become a stacking fault tetrahedron bounded by stair rod dislocations.

A hexagonal vacancy loop shows considerable relaxation on the (111) planes which pass through the edges of the loop. The intersection of these planes defines a rhomboid. The displacements can be thought of as the dissociation of the Frank dislocations into sessile stair rod dislocations and Shockley partials which extend incompletely over the faces of the rhomboid. This dissociation may explain the unexpected stability of vacancy loops in copper on annealing and be responsible for the fine structure observed in electron microscope images of such loops.

### Acknowledgments

The authors would like to thank Dr N Meissner for providing figure 5 and one of us (EJS) wishes to thank Consejo Nacional de Investigaciones Cientificas y Tecnicas, Argentina for a fellowship during the period when this work was carried out.

### References

- Barry D E and Eyre B L 1970 *Phil. Mag.* **22** 717-38  
 Beeler J R 1966 *Phys. Rev.* **150** 470-87  
 Bullough R and Hardy J R 1968 *Phil. Mag.* **17** 833-42  
 Bullough R and Perrin R C 1969 *Radiation Damage in Reactor Materials* vol II (Vienna: IAEA) pp 233-251  
 Cockayne D J H, Jenkins M L and Ray I L F 1971 *Phil. Mag.* **24** 1383-92  
 Englert A, Tompa H and Bullough R 1970 *Fundamental Aspects of Dislocation Theory*, Nat. Bureau of Standards, *Spec. Publ.* No 317 (Washington: NBS) pp 273-83  
 Eyre B L 1973 *J. Phys. F: Metal Phys.* **3** 422-70  
 Fletcher R and Reeves C M 1964 *Comput. J.* **7** 149  
 Haussermann F 1972 *Phil. Mag.* **25** 537-59  
 Ipohorski M and Spring M 1970 *Phil. Mag.* **22** 1279-84  
 de Jong M and Koehler J S 1963 *Phys. Rev.* **129** 49-61  
 Johnson R A 1967 *Phil. Mag.* **16** 553-64  
 Makin M J and Manthorpe S A 1963 *Phil. Mag.* **8** 1725-38  
 Meissner N, Savino E J, Willis J R and Bullough R 1974 *Phys. Stat. Solidi B* **63** 139-51  
 Norgett M J, Perrin R C and Savino E J 1972 *J. Phys. F: Metal Phys.* **2** L73-5  
 Perrin R C, Englert A and Bullough R 1972 *Interatomic Potentials and Simulation of Lattice Defects* ed P C Gehlen, J R Beeler and R I Jaffee (New York: Plenum) pp 509-24  
 Perrin R C and Savino E J 1973 *J. Microsc.* **98** 214-20  
 Sigler J A and Kuhlmann-Wilsdorf D 1966 *The Nature of Small Defect Clusters* AERE Rep. R-5269 pp 125-43  
 Silcox J and Hirsch P B 1959 *Phil. Mag.* **4** 72-89  
 Stobbs W M and Sworn C H 1971 *Phil. Mag.* **24** 1365-81  
 Wilson M M and Hirsch P B 1972 *Phil. Mag.* **25** 983-92



## The influence of local volume forces on surface relaxation of pure metals and alloys: applications to Ni, Al and Ni<sub>3</sub>Al

By E. J. SAVINO† and D. FARKAS‡

† International Centre for Theoretical Physics, 34100 Trieste, Italy

‡ Virginia Polytechnic Institute and State University,  
Department of Materials Engineering, 202 Holden Hall, Blacksburg,  
Virginia 24061, U.S.A.

### ABSTRACT

We present an analysis of the relative influence of the interatomic potential, lattice structure and defect symmetry on the calculated and measured distortion for the free surfaces of alloys and pure metals. In particular, the effect of using local 'volume' dependent interactions is studied, as opposed to simple pair interatomic forces. The dependence of the relaxation on the lattice structure is examined by comparing pure metals with ordered alloys. A Green function method for surface relaxation is presented and used for the above analysis as well as for studying the influence of different surface symmetries. Examples based on computer simulation of Ni, Al and Ni<sub>3</sub>Al for some surface orientations are presented.

### §1. INTRODUCTION

At present much experimental and theoretical effort is being devoted to the study of intermetallic alloys, with special emphasis on the Ni, Al system, mainly NiAl and Ni<sub>3</sub>Al. The free-surface distortion of some of these alloys has been measured by Davis and Noonan (1985), Sondericker, Jona, Moruzzi and Marcus (1985) and Sondericker, Jona and Marcus (1986). These authors report for the (110) surface of NiAl perpendicular distortions which oscillate in value as a function of depth and a relatively large outwards displacement of the Al atoms at the free surface (0.22 Å). For the (100) surface of Ni<sub>3</sub>Al, a slight buckling is found with a small displacement outwards of the Al atoms (0.02 ± 0.03 Å) together with a contraction of the first interplanar distance. Oscillations in the perpendicular atomic relaxations were also observed in pure Al and Ni surfaces by Sondericker *et al.* (1986), Nielsen, Anderson, Petersen and Adams (1982), Anderson, Nielsen, Petersen and Adams (1984), Noonan and Davis (1984) and Adams, Petersen and Sorensen (1985). On the theoretical side, the above experimental results have been reproduced by the computer simulation calculations of Chen, Voter and Srolovitz (1986), Foiles and Daw (1987), Farkas, Savino, Chidambaram, Voter, Chen and Srolovitz (1987). Jona (1978) and Gupta (1981) showed that the above contraction of the first interplanar distance can be reproduced by those calculations if a many-body interaction potential is adopted. In the above mentioned computer simulations the energy of an ensemble of  $N$  atoms is expressed as

$$E_{\text{tot}} = U_p + U_N, \quad (1)$$

where  $U_p$  is a pair-interaction term and  $U_N$  depends on the local density at the atom

†Adjunct Professor Virginia Polytechnic Institute and State University, Materials Engineering Department, Blacksburg, Virginia, U.S.A. On leave from Comision Nacional de Energia Atomica, Departamento de Materiales, Buenos Aires, Argentina.

location. This expression (1) is the same as that used in the 'embedded atom' model of Daw and Baskes (1984), in the 'empirical' model of Finnis and Sinclair (1984) and in the 'glue' model of Ercolessi, Parinello and Tosatti (1986 a) and Ercolessi, Tosatti and Parinello (1986 b). We shall refer hereafter to all of these potentials as 'local volume dependent'. Ercolessi *et al.* (1986 a, 1986 b), successfully calculated the measured surface reconstruction in Au, providing a quantitative approach to Heine and Marks' (1982) explanation of surface reconstruction as resulting from the opposition of two types of forces: a pair-wise repulsion between the atoms and a multi-atom electron-gas attraction. Therefore, the approximation of eqn. (1) for the energy has proved quite successful in the numerical simulation of surface properties both for alloys and for pure metals. Those calculations do not involve any change in the energy function at the surface except for the absence of atoms in one-half space. Also, in general, that function is adjusted only to bulk properties of the material. The purpose of this paper is to examine the relative influence of pair and local volume-dependent terms in the energy on the different modes of surface relaxation, namely static oscillations, buckling, etc. We expect the above-mentioned opposite character of the two kinds of forces not only to determine the surface restructuring but also to affect relaxation. We shall emphasize the different static distortions to be expected in alloys with respect to those in pure metals. In that sense, we will advance the basis of a lattice model for the static relaxation of the surface arising from force sources. This model extends the previous ones of Gupta (1981), Jona (1978), and Allan and Lannoo (1973, 1976) to the case of a lattice with more than one atom per unit cell. Some computer simulation results for the free surface of Ni, Al and Ni<sub>3</sub>Al are reported. These results are based on the interatomic potentials of Voter and Chen (1987) developed within the spirit of Daw and Baskes (1984) 'embedded-atom' model. The calculated relaxations, together with those previously reported in the literature for the same systems, are discussed on the basis of the lattice model for the static distortion developed below. Therefore, we shall present a consistent analysis of the relative influence of the interatomic potential, lattice structure and defect symmetry on the calculated and measured distortion for the alloy and pure metal surfaces.

## §2. LATTICE DISTORTION AT THE CRYSTAL SURFACE

For the case of point defects, Flinn and Maradudin (1962) and Tewary (1973) developed a Green function approach for the calculation of the lattice relaxation. An equivalent but simplified approach was reported for the atomic relaxation at the surface of simple metals by Allan *et al.* (1973; 1976) and by Landman, Hill and Mostoller (1980). A more detailed approach, which takes into account the full lattice and defect symmetry and is based on the validity of a general interatomic-potential law, can be developed for the surface distortions even in the case of alloys. The physical and mathematical basis of this approach is necessary for the understanding of the general pattern of relaxation behind the computer simulation results. In this section we present the basic concepts of defect-source force and lattice response.

For small static displacements  $u(L)$  of an atom  $L$  or a cluster of atoms at the lattice site  $L$  of an ensemble, the energy can be expanded as a function of the displacements as

$$E = E_{\text{tot}}^0 - \sum_L K_L^0(L) \cdot u_L(L) + 1/2 \sum_{L,L'} \phi_{LL'}^0(L, L') u_L(L) u_{L'}(L'), \quad (2)$$

where  $E_{\text{tot}}^0$  is the energy of the ensemble when every atom is located at the perfect

lattice sites (for the free surface it corresponds to the energy of the *unrelaxed* half space).  $\mathbf{K}_i^0(L) = -\partial E_{tot}^0/\partial u_i(L)$  are the forces at the unrelaxed lattice site and  $\phi^*(L, L')$  is the force constant matrix for the defect lattice:

$$\phi^*(L, L') = \phi(L, L') + \zeta(L, L'). \quad (3)$$

In eqn. (3)  $\phi_{ij}(L, L') = \partial^2 E_{tot}/\partial u_i(L)\partial u_j(L')$  is the force-constant matrix for the perfect lattice and  $\zeta$  includes the change in force constants caused by the defect. These changes arise from the loss of atomic interactions and to the eventual changes in the interaction constants.  $\zeta$  also may contain terms of order higher than second in the expansion of the energy, that is, anharmonic distortion terms. By analogy to the approach of Kanzaki (1957) to the equivalent problem for the point defect, the Kanzaki forces  $K$  are defined to contain the effect of that change in the force constants:

$$\mathbf{K}(L) = \mathbf{K}^0(L) - \zeta(L, L') \cdot \mathbf{u}(L'). \quad (4)$$

The lattice relaxation can be obtained by imposing a condition of minima to the energy in eqn. (2). It results in

$$\mathbf{u}(L) = \mathbf{G}^*(L, L') \mathbf{K}^0(L') \quad (5)$$

where the Green function  $\mathbf{G}^*$  has been defined as the inverse of the defect-lattice force-constant matrix, that is,  $\mathbf{G}^* = \phi^{*-1}$ . Recently, Garcia Moliner, Platero and Velasco (1984), Garcia Moliner and Velasco (1986) and Levi, Benedek, Miglio, Platero, Velasco and Garcia Moliner (1984) have developed a general procedure for calculating the dynamic Green function for modelling surface and interphase properties. The above-defined lattice static Green function corresponds to the zero-frequency limit of their dynamic one. The only relevant approximation in their calculation is that the surface-induced perturbation of the force-constant matrix is taken as relatively short range. Hence, within this approach, solving eqn. (5) constitutes an alternative method for calculating surface atomic distortion to the computer simulation used hereafter.

For the case of an alloy, a set of  $N_k$  atoms is located at every lattice site  $L$  of a Bravais lattice. The atomic positions associated with site  $L$  are thus denoted by the pair of indices  $(l, k)$ . The forces on the atoms are defined by the corresponding derivatives of the energy in eqn. (2). Those forces and the atomic displacements are related to those in eqns. (4) and (5) by the equations

$$\mathbf{u}(l, k) = \mathbf{u}(L) + \Delta \mathbf{u}(l, k), \quad (6a)$$

$$\mathbf{K}^0(l, k) = \mathbf{K}^0(L) + \Delta \mathbf{K}^0(l, k), \quad (6b)$$

where the first term of the right-hand side is the symmetric, 'acoustic' mode of Farkas *et al.* (1987):

$$\mathbf{u}(L) = N_k^{-1} \sum_{k=1, N_k} \mathbf{u}(l, k), \quad \mathbf{K}^0(L) = N_k^{-1} \sum_{k=1, N_k} \mathbf{K}^0(l, k).$$

The second term is the relative, antisymmetric or 'optical' mode for each atom at the cell.

Minimizing the energy with respect to the atomic displacements yields the system

of coupled equations:

$$N_k \cdot K_i^0(L) = \Phi_{ij}^L(L, L') u_j(L') + \Phi_{ij}^{LK}(L, l'k') \Delta u_j(l', k'), \quad (7a)$$

$$\Delta K_i^0(l, k) = \Phi_{ij}^K(lk, l'k') \Delta u_j(l', k') + \Phi_{ij}^{LK}(lk, L') u_j(L'), \quad (7b)$$

where

$$\Phi^L(L, L') = \sum_{k, k'} \varphi^*(lk, l'k'),$$

$$\Phi^{LK}(L, l'k') = \Phi^{LK}(l'k', L) = \sum_k \varphi^*(lk, l'k'),$$

$$\Phi^K(lk, l'k') = \varphi^*(lk, l'k')$$

the defect lattice force constants  $\varphi^*$  are defined like those in eqn. (3) but the derivatives are taken with respect to the relative atomic displacements within

Contrary to eqn. (5) these equations include the dispersive response of the lattice as defined by Kunin (1982, 1983).

### §3. EFFECT OF LOCAL-VOLUME DEPENDENT INTERATOMIC POTENTIAL

In §3 we summarize some general information about the local volume-dependent potentials. In eqn. (1) for the energy it is assumed that the pair part can be expanded as a sum over the atom pairs at the ensemble:

$$U_P = 1/2 \sum_{M, M' \neq M} V(R_{MM'}) \quad (8)$$

where  $R_{MM'}$  is the distance between  $M$  and  $M'$  atoms (in §3  $M = (l, k)$ ). Also the local-volume-dependent part can be expanded as a simple sum over the atoms:

$$U_N = \sum_M f_M(\rho_M), \quad (9)$$

where  $\rho_M$  corresponds to the local density at the location of the atom  $M$ . This density is evaluated as a sum of functions dependent on the distance between the atom  $M$  and its neighbours:

$$\rho_M = \sum_{M' \neq M} \varphi_{M'}(R_{MM'}). \quad (10)$$

Therefore, its value (10) is scaled with the number of neighbours per shell and the function  $\varphi_{M'}$  depends on the type of neighbour  $M'$  but not on the atom  $M$  where the density is evaluated. As done by Ercolessi *et al.* (1986a, 1986b) in the case of only first-neighbour interaction  $\varphi_M$  may be normalized to unity at the neighbour distance.

The source forces  $K^0$  (Kanzaki forces for the *unrelaxed* lattice) in eqn. (5) can be evaluated for the free-surface defect. Those are obtained from the total energy of the unrelaxed semi-infinite ensemble of atoms at the perfect lattice location ending at a plane free surface. By inserting eqns. (8) and (9) into (1) and deriving the energy with respect to the atom coordinances, the force on atom  $M$  is

$$K^0(M) = - \sum_{M' \neq M} [V' + \varphi'_{M'} f'_{M'} + \varphi'_{M'} f'_{M'}] R_{LL'} / |R_{LL'}|, \quad (11)$$

where  $V'$  and  $\varphi'$  stand for  $\partial(V, \varphi)/\partial R_{MM'}$  and  $f'$  for  $\partial f/\partial \rho$ . In the bulk, lattice

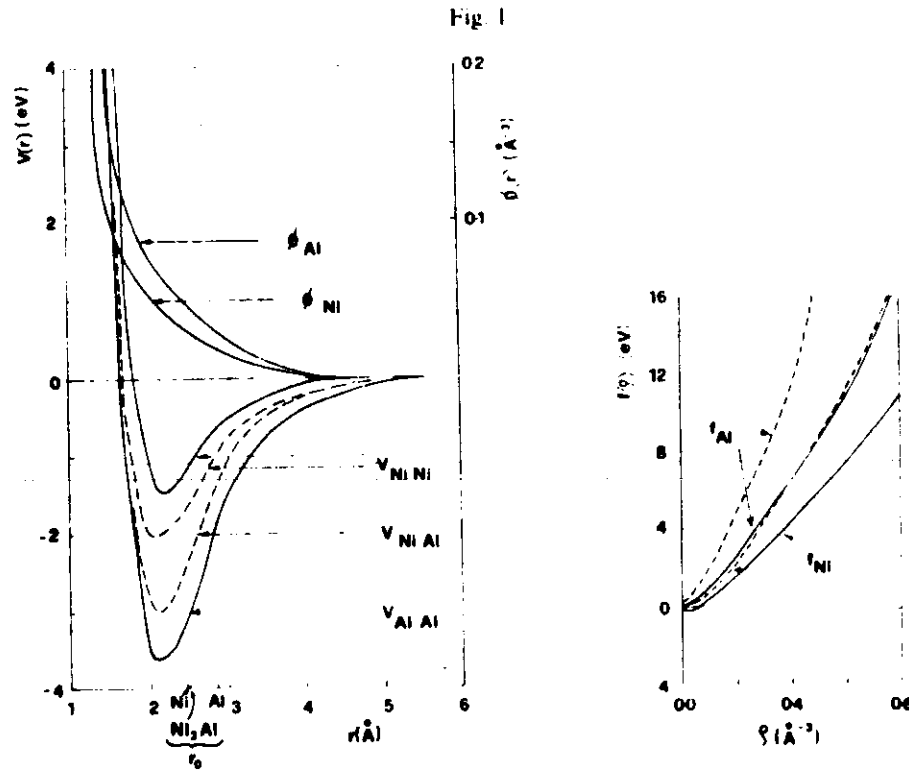


symmetry imposes the cancellation of those forces for a finite-range interatomic potential. Even in the perfect lattice, equilibrium results by the cancellation between opposed pair and volume-dependent forces. At the surface, some atoms miss neighbour atomic interactions. If  $M$  in eqn. (11) stands for one of those atoms, the lack of the corresponding pair in the direction normal to the surface determines a net force due to non-cancellation of the first term on the right-hand side of (11). Also there is a change in the local density  $\rho_M$ . This, in turn, determines the existence of a force on the surface atoms  $M$  arising from the unbalanced last two terms of the right-hand side of eqn. (11). However, even those atoms  $M'$  which do not lose interactions, suffer a force if they interact with surface atoms  $M$  that have reduced their local density by being at the surface. Therefore, within this local-volume model, the competition between volume and pair forces is built into the source of distortion at the surface. As mentioned before, the change in eqn. (3) in the force-constant matrix induced by the defect arises from the loss of atomic interactions and to eventual changes in the interaction constants. The latter are included within the local volume-dependent potential model, contrary to the case where there is only a pair-wise atomic interaction which cannot consistently model a change in interaction constants at the defect core unless imposed *ad hoc*. Therefore, in the local-volume potentials the charge redistribution at the surface is included in the model within the spirit of the description of Heine and Marks (1982) and Finnis and Heine (1974). This is an important difference with the description provided by a pair-interaction model. In addition, if the lattice is modelled as in equilibrium under solely a pair potential the forces (11) must cancel even at the surface. Surface relaxation in that case results from the change in the force-constant matrix because of the loss of atomic interaction at the surface and under the boundary condition of non-average crystal distortion. If a non-equilibrium pair interaction is adopted with a Cauchy pressure applied over the lattice (see Born and Huang (1966)) the source forces will be mainly determined by that pressure. In the case of a positive pressure, like in Ni, Al and Ni<sub>3</sub>Al, those forces will induce an average expansion of the first interlayer distances, in contradiction with the experimental findings.

#### §4. Ni, Al AND Ni<sub>3</sub>Al SURFACE RELAXATION CALCULATION

The local-volume-dependent interatomic potentials used for the calculations were developed by Voter and Chen (1987). Those potentials fit exactly the lattice parameter, cohesive energy and bulk modulus of the pure metals Ni and Al; while they provide an adequate fitting to elastic constants and vacancy formation energy of those metals and of Ni<sub>3</sub>Al. Also for that alloy the superlattice intrinsic stacking fault (SISF), and the (100) and (111) antiphase boundary energies have been fitted together with the lattice parameter and cohesive energy for that alloy and for NiAl. The corresponding functions  $V$ ,  $f$  and  $\phi_M$  defined in eqns. (8) to (10) are plotted in fig. 1. In the plot for the pair part of the interactions and the density as a function of the distance, the first-neighbour locations for Ni, Al, NiAl and Ni<sub>3</sub>Al are shown. It can be clearly seen that at those distances, equilibrium is attained by a competition between strong pair and volume-dependent interaction forces.

The relaxation in the surface region is calculated by means of a numerical procedure based on DEVIL, the computer simulation program developed at Harwell by Norgett, Perrin and Savino (1972). The program is based on a conjugate-gradient method for finding the minimum of the energy (1) for a given ensemble of atoms. DEVIL allows one to generate a lattice with up to six atoms per Bravais lattice site.



Interatomic potential functions for Ni, Al and Ni/Al alloys. Voter *et al.* (1987). Full and dotted lines correspond to a set of energy functions related among themselves by the invariance relations discussed by those authors.

The lattice coordinate axes are taken in accordance with the type of surface to be simulated. Denoting by  $\hat{z}$  the direction normal to the surface, periodic boundary conditions are used in the directions perpendicular to  $\hat{z}$ . That is the location  $\mathbf{S}$  of an atom  $M$  outside the relaxed region is uniquely related to an atom  $M^0$ , within it, by the translation

$$\mathbf{S}(M) = \mathbf{S}(M^0) + m\Delta x\hat{x} + n\Delta y\hat{y}, \quad (12a)$$

where  $n$  and  $m$  are integers and  $\Delta x$ ,  $\Delta y$  are the periodicity lengths. This implies for the displacements:

$$u(M) = u(M^0). \quad (12b)$$

Therefore the free surface is determined by a simple square lattice in the  $xy$  plane and is semi-infinite in the  $\hat{z}$  direction. The conditions (12b) mean that the square-planar lattice cannot be distorted:

$$\sum_{M \in N_S} u(M) \cdot \hat{x} = \sum_{M \in N_S} u(M) \cdot \hat{y} = 0 \quad (13)$$

where  $N_S$  are the atoms located in the relaxed region. (If eqn. (13) were not satisfied the displacements in eqn. (12b) would depend on  $n$  and  $m$  in (12a).)

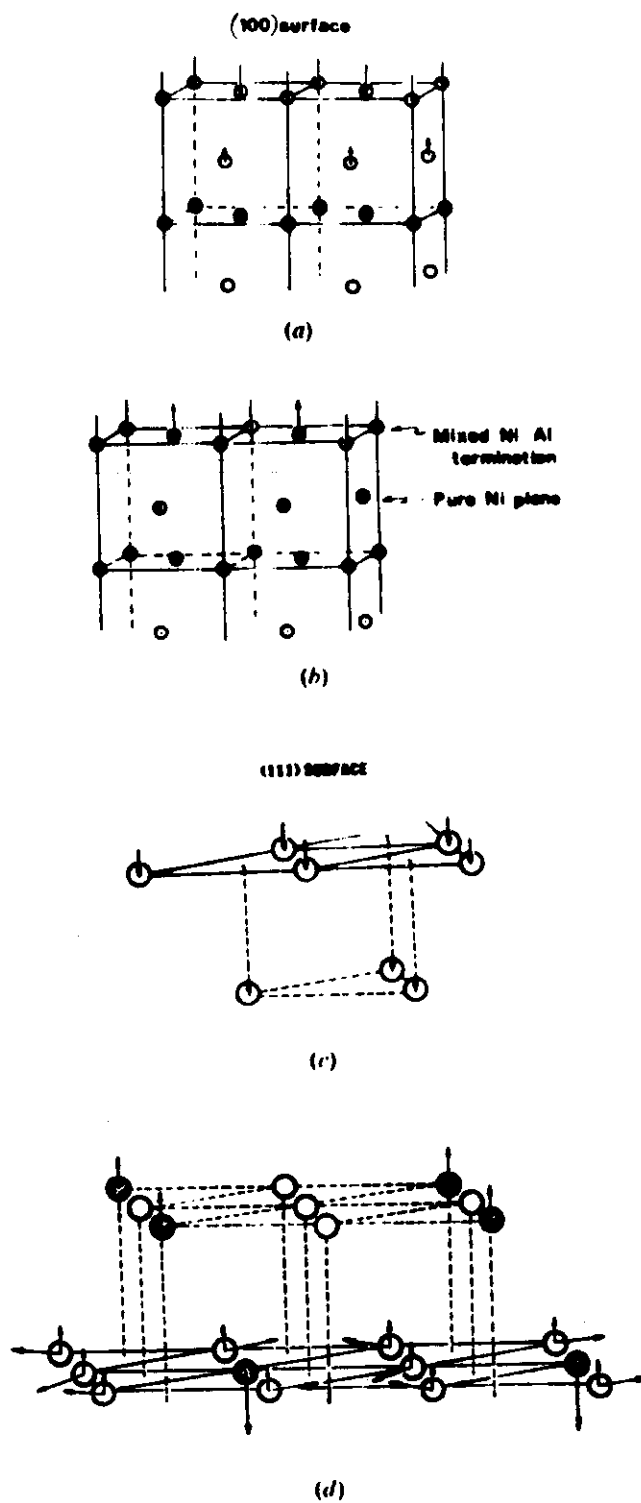
## §5. CALCULATION RESULTS

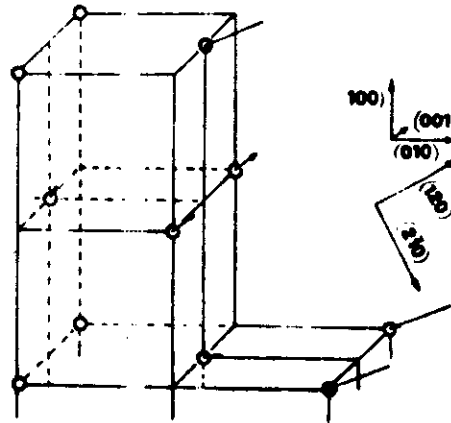
Chen, Voter and Srolovitz (1986, 1987), Foiles and Daw (1987), and Farkas *et al.* (1987) have calculated some free-surface distortions for Ni, Al, NiAl and Ni<sub>3</sub>Al by using local volume-dependent interatomic potentials. For the sake of completeness we shall briefly review their main results. For the alloy NiAl a contraction was found for the (110) surface 50/50 NiAl termination and for the (111) pure Ni termination. On the other side the (100) surface either with 50/50 NiAl or pure Ni termination expanded. Also an expansion was predicted for the (111) surface in that alloy. Chen *et al.* (1987) explain these results as a consequence of the relative size of the Ni and Al atoms. This determines Al to be under compression in the alloys, while the Ni atoms are under tension but to a smaller extent than the Al atoms are compressed. The calculations for Ni<sub>3</sub>Al generally show a small displacement of the first atomic layer but always a rippling effect, with the Al atoms outwards with respect to the Ni atoms. Finally, Farkas *et al.* (1987) show in their study of (111) planar defects in Ni<sub>3</sub>Al, relaxations oscillatory in directions parallel to the defect plane. Here, we shall report some simulations of the (100), (111) and (120) free surfaces of Ni, Al and Ni<sub>3</sub>Al. These were done by allowing for the relaxation of more than 100 planes parallel to the surface, Farkas *et al.* (1987). The results will be analysed within the theory developed in §2.

The (100), (111) and (120) free-surface configurations of the pure metals and of Ni<sub>3</sub>Al are shown in fig. 2. Arrows proportional to the Kanzaki forces at the unrelaxed configuration and evaluated through eqn. (11) are plotted in fig. 2. For the pure metals, those forces are perpendicular to the (100) and (111) surfaces, while they have a shear component parallel to the (120) surface. These shear forces must satisfy the same equilibrium condition eqn. (13) as the atomic displacements. One can see also that the perpendicular forces change sign as a function of the distance from the surface. While the existence of opposite signs in the shear forces is a consequence of the surface symmetry, this change in the sign of the perpendicular forces results from the competition between the pair and the local volume-dependent part of the potential. As discussed in §3 the existence of the surface causes some pair interactions plus volume-dependent forces to remain unbalanced for the outmost external atoms, while the change in the local density of those same atoms determines density-dependent forces to appear over deeper ones. For the alloy, even in the case of the (100) surface, there is an internal straining of the lattice cell by small force moments. For the (100) surface those moments are perpendicular to the surface and may give rise to rippling. For the (111) surface the internal straining and moments may be either perpendicular to the surface or within a 120° rotation symmetry around a normal axis that contains an Al atom at the surface. For the (120) surface, the axis normal to the surface is not a symmetry axis of the unit cell; the resulting strain by Kanzaki forces is, therefore, more complex. Those forces for the unrelaxed lattice are shown schematically in fig. 2.

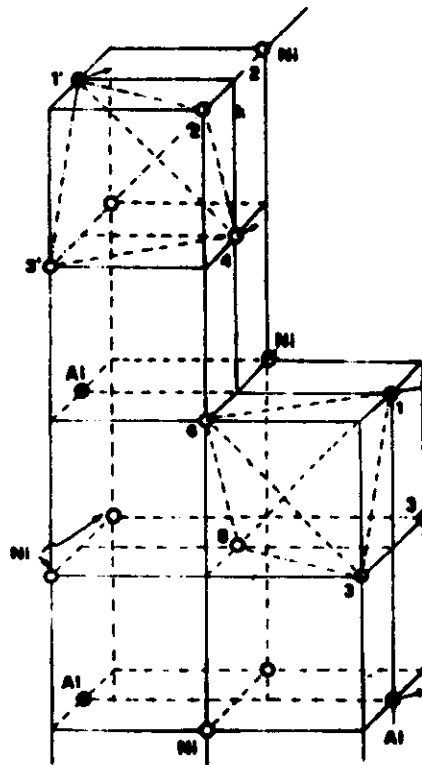
We summarize in the table the relaxation of the first layers calculated for the (100) surface of the pure metals and the two possible terminations of the Ni<sub>3</sub>Al alloy, as well as the predicted rippling. These results agree with those obtained by Chen *et al.* (1986) with the same interatomic potential but using a somewhat different relaxation procedure. Also Foiles and Daw (1987) calculated a similar relaxation pattern; they report for the 50/50 termination of the alloy an outwards displacement of the Al atom of 0.06 Å, smaller than ours. Both calculated values are much larger than the experimental ones of Sondericker *et al.* (1985, 1986). In addition, the average contraction of the outer layers as calculated by us is ten times smaller than the

Fig. 2





(e)



(f)

Sketch of (100), (111) and (120) surfaces. (a), (c), (e): pure metals. (b), (d), (f): Ni<sub>3</sub>Al alloy. Shaded circles stand for Al atoms and the arrows for the 'unrelaxed' lattice Kanzaki forces (not to scale).

(100) surface relaxation in units 'per thousand' of interplanar separation.  $z$  Al-Ni is the distance between Al and Ni atoms at the  $n$ th plane below the surface.

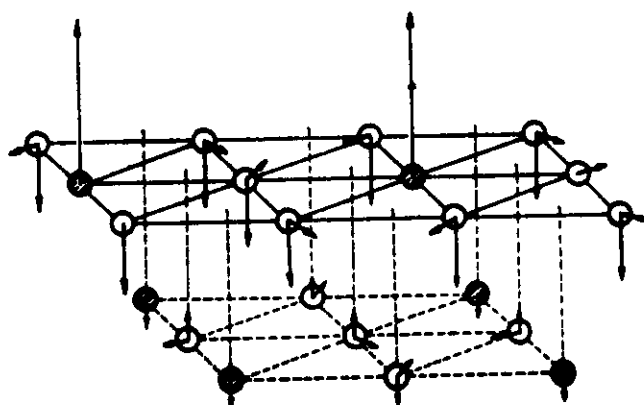
$\Delta d_{n,n+1}$	Ni	Al	Ni <sub>3</sub> Al Ni term	$z$ Al-Ni (Å)	Ni/Al term	$z$ Al-Ni (Å)
$\Delta d_{1,2}$	-10	-29	$\approx 0^\dagger$	—	-3	0.09
$\Delta d_{2,3}$	-5	-8	-4	0.01	-4	—
$\Delta d_{3,4}$	$\approx 0^\dagger$	1	$\approx 0^\dagger$	—	$\approx 0^\dagger$	0.00

$^\dagger$  Absolute value smaller than 0.5 per thousand.

measured one. This disagreement is also a consequence of the large outwards relaxation of the Al atoms predicted by the simulation; that is, the Ni atoms relax inwards by 0.05 Å, agreeing with the experimental value ( $0.05 \pm 0.03$  Å).

A detailed set of results for the computer simulation of (111) planar defects in Ni<sub>3</sub>Al has been reported by Farkas *et al.* (1987); those have been obtained by using the same interatomic potential and relaxation program as used here. In that work we have already separated the symmetric, 'acoustic', contribution to the atomic displacements from the antisymmetric, 'optical', one. The first results mainly from the relaxation of the body forces induced by the Kanzaki forces, while the second is mainly due to the internal strain induced by the moments of those same forces over the atomic cells. As shown in fig. 2, the body forces are in this case perpendicular to the surface, and their main effect is to contract the first interlayer distance. The moments induce a rippling of the outermost layer, with the Al atoms moving outwards with respect to the Ni atoms. Also, oscillations parallel to the free surface appear. Those have the allowed symmetry of 120° around the Al atom and are mainly located in the first and second layer below the surface, fig. 3. Therefore, the internal strain results in a consistent outwards relaxation of the Al atoms at the outermost layer while their nearest neighbour Ni atoms, move in the same atomic plane outwards away from the Al atoms located at the second plane. The Ni atoms at

Fig. 3

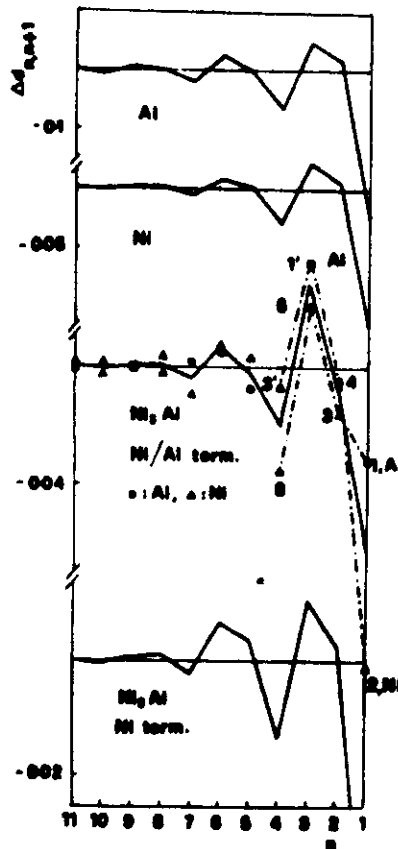


Atomic displacements of the first two layers of a (111) surface in Ni<sub>3</sub>Al. The arrows showing the displacement are in units of lattice distance multiplied by 50.

the second plane move by trying to compensate for the density change arising from the large outwards displacement of the Al. The displacements are consistent with the symmetry restrictions mentioned above.

As a final set of results we report in fig. 4 the atomic relaxation perpendicular to the (120) surfaces. It can be seen that, except for the scale, the pure Ni and Al relaxations are identical. For both terminations of the Ni<sub>3</sub>Al, by performing an average over the Ni and Al atom relaxations at the same (120) plane, an oscillatory pattern appears very similar to the one in the pure metals. This pattern is, therefore, a consequence of the surface symmetry. However, for the alloy, moments have a strong effect and they impose, on the one hand, the relaxation of the Al atoms outwards with respect to the Ni atoms at the outermost layer and, on the other, affect the pattern of the average relaxations plotted here. For example we see in fig. 4 that, in the case of a mixed Ni-Al termination, the plane interspace 2-3 contracts, while it expands in the

Fig. 4



Relative change of interplanar distance perpendicular to (120) surface. For the Ni<sub>3</sub>Al two terminations are shown. The full line for Ni<sub>3</sub>Al corresponds to the average (120) plane displacement, the dots stand for the relative change in the distance of an atom in the plane  $n$  to the displaced  $(n+1)$  plane.

pure metals. In the case of a pure Ni termination it expands even more. This difference arises from the fact that, for the mixed termination case, the third atomic layer contains Al atoms which tend to displace outwards with respect to that layer. The opposite happens for the pure Ni termination, where now the Al atoms are located in the second layer but none are in the first and third layers. In our calculation, Al seems to impose severe internal strains. Another way of visualizing the importance of the moments with respect to the body forces is by showing those strains in different atomic tetrahedra in the surface. In fig. 3, we have joined with a dotted line the change in the interplanar distances by the atoms 1,3,6,8 and that of 2,4,1',3' (see fig. 2 for the numbering). It can be seen that the first of those tetrahedra, where Al is at the free surface, is less strained than the second one, which contains an inside Al atom. Also, displacements parallel to the surface, if allowed by symmetry, can be important in relaxing internal moments, even for the pure metals, within those atomic cells. We have found in our calculation displacements parallel to the (120) surface of up to 0.015 Å in Ni, 0.038 Å in Al and 0.055 Å in Ni<sub>3</sub>Al. For the pure metals the main displacement takes place at the third layer, while for the alloy it does so at the outermost layer.

#### §6. SUMMARY AND DISCUSSION

In this Paper we have studied some of the physical causes of the atomic displacements from the perfect-lattice sites at the free surfaces of metals and alloys, mainly pure Ni, Al, and Ni<sub>3</sub>Al. In §2, we have established the basis of a force-discontinuity model for calculating lattice-surface relaxation. Within that model, the displacement of the surface atoms from their perfect lattice positions was treated as the response to a set of Kanzaki forces, as defined also in §2. In §3 some effects of using local volume-dependent potentials for the calculations were described. Surface distortions predicted by using those potentials were compared with those resulting from a simple pair-interaction model. It was found that, for the systems studied, the latter model is unable to reproduce even the measured contraction of some surfaces. In §4, we have shown the influence of the surface and lattice symmetry on the possible distortion modes of the free surface when restructuring is not allowed. In §5, we reported some computer simulations of the static configuration of free surfaces in Ni, Al and Ni<sub>3</sub>Al. The interatomic potential deduced by Voter and Chen (1987) was used for the calculations. It was shown there that very symmetric surfaces, like (100) and (111) in f.c.c., allow only for perpendicular, however oscillatory, relaxation in the pure metal. In addition, for the alloy, rippling was calculated, in agreement (although somewhat larger in value) with the experiments. For the (111) surface oscillatory relaxations parallel to the surface were reported by Farkas *et al.* (1987). We emphasized that this relaxation can be understood in the same manner as the rippling, as arising from straining of the tetrahedra formed by the motive in Ni<sub>3</sub>Al. Finally for the (120) surface, which is less symmetric than those already mentioned, oscillatory distortions parallel to the surface were found even for pure metals. Also the local strain of different lattice cells located at the same distance from the (120) surface was shown. We shall now discuss the consistency of the above results.

We shall first discuss the origin of the perpendicular relaxation at the surface and the connection between the calculated outer-layer contraction and oscillations with the assumptions of the model. We have shown in §3 that if a pair-interaction potential is assumed for the calculation, a perpendicular expansion will be predicted for Ni, Al and Ni<sub>3</sub>Al surfaces, in disagreement with the experimental findings. On physical



grounds, the surface contracts when the atoms at the surface, located at the perfect-lattice site, try to regain their local bulk density, strongly depleted by the absence of neighbours. However, this relaxation implies that some inner atoms suffer an increase in their local density because of the approach of those located at the immediate neighbourhood of the surface. Therefore, the system gains energy if those atoms compensate the induced increment in their local density by relaxing outwards from their inner neighbours. As the distortion is propagated into inner layers, this density-compensation tendency changes sign and it is intrinsically oscillatory, hence the oscillations in the relaxation. If the system is to be modelled by means of interatomic forces, the above process seems to require the inclusion of many-body interactions in the model. The quasi-analytical models of Allan and Lannoo (1973, 1976) and Landman *et al.* (1980) for the surface relaxation have also obtained oscillatory variations of the interplanar distance as a function of the distance from the surface and, in some cases, a contraction in the first of these distances. Within a simplified description of those models, Allan and Lannoo (1973, 1976) included two quadratic terms in the energy expansion as a function of the interplane separation, one proportional to the product of neighbour interplanar distances ( $\alpha d_{n,n+1} d_{n+1,n+2}$ ) and a second quadratic in those distances ( $\beta(d_{n,n+1})^2$ ;  $\alpha, \beta > 0$ ). It is easy to show that for a first-neighbour pair-interaction potential only this last term will appear; while for a longer-range one the sign of  $\alpha$  in the first term of that energy expansion will be determined by the curvature of the potential at neighbours beyond the first. If only one of the above terms appears in the energy expansion, or they are of opposite sign, no oscillations in the relaxation will be predicted by those simplified models.

With respect to the influence of the surface symmetry and lattice structure on the relaxation; we found, as said above, for the most symmetric surfaces, like (100) or (111), displacements only in the direction perpendicular to the surface plane. For less symmetric surfaces, (120), parallel displacements are also obtained. Those must satisfy the condition (13). Therefore the distortions are oscillatory and, generally, of shear type. However, their calculated magnitude is not negligible. For the case of alloys, the possibility of straining the alloy cell adds new degrees of freedom to those available for relaxation at the same orientation of the free surface. We have seen that, as a consequence of that strain, rippling appears at the surface, with the Al atoms moving outwards from the Ni whenever present at the outer plane of the Ni<sub>3</sub>Al alloy. Also oscillatory local-density changes are found, even for high-symmetry surfaces, like the (111). Their appearance is consistent with the existence of rippling at the outer atomic layer. The internal strain of each atomic cell in the alloy depends on the cell location with respect to the surface and that of the Al atom. In the (120) surface, we have obtained a larger strain for those cells with an inner Al than for those where Al is at the outer atomic layer. We can describe the effect of surface straining by the Al, including the rippling, as the surface relaxing internal lattice strains or, equivalently, as a surface-induced distortion in the electron density which, in turn, results in an atomic distortion. Within the inherently empirical character of the interatomic potentials, the surface distortion can be taken as a potential fitting parameter. The fitting can be obtained through eqn. (7), where the atomic displacements are taken as the measured ones. This fitting will mainly affect first and second derivatives of the interaction and it will give information about internal straining at the unit cell. This kind of information is not generally available in the properties used for fitting the interatomic potentials, except when the phonon optical modes are fitted.

We conclude that, in spite of the considerable success attained by using simple pair

potentials for the calculation of the distortion arising from lattice defects, for the case of free surface those potentials are not only unable to reproduce some experimental results but, in addition, do not seem to contain some of the physical features relevant to the surface distortion. The main limitation is that the competition in a crystal between the pair atomic-interaction forces and multi-atom forces cannot be neglected. For the free surface, which is a large topological discontinuity, not only restructuring, as discussed by Heine and Marks (1982), but also its relaxation seems to be determined by that competition. We have tried in this paper to show the validity of that assessment. We have also stressed the effect of surface symmetry and lattice structure on the relaxation.

As a final point in the discussion we want to refer to our result that, for an alloy, the dispersive character of the lattice and its influence on the relaxation cannot be neglected, even in the elastic limit. The internal straining of the atomic cell seems to be an important mechanism of energy relaxation. This will affect the atomic displacements at the defect core and its interaction with other sources of distortion.

#### ACKNOWLEDGMENTS

One of the authors (E.J.S.) would like to thank Professor Abdus Salam, the International Atomic Energy Agency and UNESCO for hospitality at the International Centre for Theoretical Physics, Trieste. We would also like to thank Dr A. Voter, Dr S. P. Chen and Dr D. Srolovitz for the interatomic potential used for the calculation and Dr A. Voter and Dr F. Ercolessi for useful discussions. This work was partially supported by the Energy Conversion and Utilization Technologies (ECUT) program of the U.S. Department of Energy.

#### REFERENCES

- ADAMS, D. L., PETERSEN, L. E., and SORENSEN, C. S., 1985, *J. Phys. C*, **18**, 1753.  
 ALLAN, G., and LANNOO, M., 1973, *Surf. Sci.*, **40**, 375; 1976, *Phys. Stat. Sol. (b)*, **74**, 409.  
 ANDERSON, J. N., NIELSEN, H. B., PETERSEN, L., and ADAMS, D. L., 1984, *J. Phys. C*, **17**, 173.  
 BORN, M., and HUANG, K., 1966, *Dynamical Theory of Crystal Lattices* (Oxford: Clarendon Press).  
 CHEN, S. P., VOTER, A. F., and SROLOVITZ, D. J., 1986, *Phys. Rev. Lett.*, **57**, 1308; 1987, *Mater. Res. Soc. Proc.*, **82**.  
 DAVIS, H. L., and NOONAN, J. R., 1985, *Phys. Rev. Lett.*, **54**, 566.  
 DAW, M. S., and BASKES, M. I., 1984, *Phys. Rev. B*, **29**, 6443.  
 ERCOLINI, F., PARRINELLO, M., and TOBATTI, E., 1986a, *Surf. Sci.*, **177**, 314.  
 ERCOLINI, F., TOBATTI, E., and PARRINELLO, M., 1986b, *Phys. Rev. Lett.*, **57**, 719.  
 FARKAS, D., SAVINO, E. J., CHIDAMARAM, P., VOTER, A. F., CHEN, S. P., and SROLOVITZ, D., 1987 (to be published).  
 FIDOE, M. W., and HEINE, V., 1974, *J. Phys. F*, **4**, L37.  
 FIDOE, M. W., and SINCLAIR, J. R., 1984, *Phil. Mag. A*, **59**, 45.  
 FLINN, P. A., and MARADUDIN, A. A., 1962, *Ann. Phys.*, N.Y., **18**, 81.  
 FORBES, S. M., and DAW, M. S., 1987, *J. Mater. Res.*, **2**, 5.  
 GARCIA MOLINER, F., PLATINO, G., and VELASCO, V. R., 1984, *Surf. Sci.*, **136**, 601.  
 GARCIA MOLINER, F., and VELASCO, V. R., 1986, *Phys. Scripta*, **34**, 257.  
 GUPTA, R. P., 1981, *Phys. Rev. B*, **23**, 6265.  
 HEINE, V., and MARKS, L. D., 1982, *Surf. Sci.*, **10**, 143.  
 JONA, F., 1978, *J. Phys. C*, **11**, 4271.  
 KANZAKI, H., 1957, *J. Phys. Chem. Solids*, **15**, 39.  
 LANDMAN, U., HILL, R. N., and MOSTOLLER, M., 1980, *Phys. Rev. B*, **21**, 448.  
 KUNIN, I. A., 1982, *Elastic Media with Microstructure I*, Springer Series in Solid State Science, Vol. 26 (Berlin: Springer-Verlag); 1983, *Elastic Media with Microstructure II*, Springer Series in Solid State Science, Vol. 44 (Berlin: Springer-Verlag).

- LEVI, A., BENEDEK, G., MIGLIO, L., PLATERO, G., VELASCO, V. R., and GARCIA MOLINER, F., 1984, *Surf. Sci.*, **193**, 253.
- NIELSEN, H. B., ANDERSON, J. N., PETERSEN, L., and ADAMS, D. L., 1982, *J. Phys. C*, **15**, L1113.
- NOONAN, J. R., and DAVIS, H. L., 1984, *Phys. Rev. B*, **29**, 4349.
- NORGETT, M. J., PERRIN, R. C., and SAVINO, E. J., 1972, *J. Phys. F*, **2**, L73.
- SONDERICKER, D., JONA, F., and MARCUS, P. M., 1986, *Phys. Rev. B*, **33**, 900.
- SONDERICKER, D., JONA, F., MORUZZI, V. L., and MARCUS, P. M., 1985, *Solid St. Commun.*, **53**, 175.
- TEWARY, V. K., 1973, *Adv. Phys.*, **22**, 757.
- VOTER, A. F., and CHEN, S. P., 1987, *Mater. Res. Soc. Proc., Boston*, **82**, 175.



## Oscillatory relaxations in (111) planar defects in $\text{Ni}_3\text{Al}$

By D. FARKAS, E. J. SAVINO, P. CHIDAMBARAM†

Department of Materials Engineering, Virginia Polytechnic and State University, Blacksburg, Virginia 24061, U.S.A.

A. F. VOTER, D. J. SROLOVITZ and S. P. CHEN‡

Los Alamos National Laboratory, Los Alamos, New Mexico 87545, U.S.A.

[Received 15 December 1987§ and accepted 7 November 1988]

### ABSTRACT

Computer simulation results are presented for various types of planar defect occurring on the (111) plane of the intermetallic compound  $\text{Ni}_3\text{Al}$ . The relaxed defect structures produce oscillations in the static displacements, both perpendicular and parallel to the boundary plane. This type of relaxation behaviour is related to the fact that the ordered lattice contains more than one atom per lattice site. Therefore, two different types of static distortion mode are found which, by analogy with lattice vibration modes, are called acoustic and optical. For the planar defects studied here, these two types of distortion mode were separated and it was found that the optical distortion mode is of similar nature in all of them. The acoustic mode is similar to that found in pure Ni and Al.

### §1. INTRODUCTION

The present work is a detailed study of the static relaxation behaviour of (111) planar defects of  $\text{Ni}_3\text{Al}$ .  $\text{Ni}_3\text{Al}$  was chosen because of recent interest in the nature of planar defects in this alloy (Liu, White and Horton 1985). This interest is attributable to the material's excellent high-temperature properties and propensity to intergranular fracture. Interatomic potentials which include a pair interaction plus a local volume term, as proposed by Daw and Baskes (1984), have been developed for the Ni-Al system by Voter and Chen (1987). Recent work using these potentials revealed oscillatory behaviour in the surface static relaxation for a variety of free surfaces and grain boundaries in pure metals and ordered alloys (Chen, Voter and Srolovitz 1986a, 1987a,c). Savino and Farkas (1988) provided a framework for analysing this oscillatory relaxation behaviour and they studied some free surfaces of  $\text{Ni}_3\text{Al}$ . The aim of the present investigation is to examine the relaxation behaviour of a number of internal interfaces on the (111) plane of  $\text{Ni}_3\text{Al}$  (twin, stacking fault and antiphase boundary interfaces) and the free (111) surface.

An important consideration in the study of planar defects in ordered structures is that, for most orientations, atomic planes with the same index are different in nature.

†Permanent address: Departamento de Materiales, Comisión Nacional de Energía Atómica, Argentina.

‡Permanent address: Department of Materials Science and Engineering, University of Michigan, Ann Arbor, Michigan 48109, U.S.A.

§Received in present form 28 September 1988.

This occurs for all surfaces containing even Miller indices (Farkas and Ran 1986). In the present work, we restrict the simulations to defects in the (111) plane, where this effect does not arise and the configuration of each type of defect is unique. Furthermore, (111) planar defects play a major role in the splitting of glide dislocations, and they must be studied in relation to mechanical behaviour in these alloys and as a necessary previous step to any dislocation study (Yamaguchi, Paidar, Pope and Vitek 1982).

Since  $\text{Ni}_3\text{Al}$  is an  $\text{L1}_2$  ( $\text{Cu}_3\text{Au}$ ) alloy, it may be described as consisting of four interpenetrating simple-cubic sublattices. One of these sublattices is occupied by Al and hence, even in the perfect lattice, it is not equivalent to the other three. However, each one of them may respond to an applied distortion in different ways. When such distortions occur because of the presence of an internal defect, the response depends on the defect symmetry. In cases where an entire atomic plane would translate uniformly in a pure metal, internal distortion of the atomic planes in the ordered alloy may occur. Savino and Farkas (1988) described the defect-induced atomic displacements in lattices containing more than one atom per unit cell in terms of what they call acoustic and optical components. The net translation of the plane parallel to the planar defect corresponds to an acoustical mode, while relative motion of the sublattices corresponds to optical modes. In analysing our results below, we shall apply that same distinction between modes of static distortion.

## § 2. THEORY AND CALCULATIONS

### 2.1. Numerical method

In simulating the interface structures, we employ the local-volume potentials for the Ni–Al system described by Voter and Chen (1987). These potentials are very similar to the embedded-atom method of Daw and Baskes (1984), which has proved successful in a variety of applications (Chen, Voter and Solovitz 1986a, b, 1987a, b, c, Foiles and Daw 1987). The method is inherently many-bodied and divides the crystal energy into two distinct terms: a local-density or volume term and a pairwise interaction term. The local-density term circumvents the problems associated with a fixed-volume pair potential, in that major defects (e.g. free surfaces) can be treated in spite of the severe change in density. The total energy of a homonuclear system of atoms is given by

$$e = \sum_i E_i, \quad (1)$$

where the energy of atom  $i$  is

$$E_i = \frac{1}{2} \sum_{j \neq i} \phi(r_{ij}) + F \left[ \sum_{j \neq i} \rho(r_{ij}) \right]. \quad (2)$$

Here  $r_{ij}$  is the scalar distance between atoms  $i$  and  $j$ ,  $\phi(r)$  is the pairwise interaction (a Morse function with cut-off; four parameters),  $\rho(r)$  is the density function (taken as  $r^6[\exp(-\beta r) + 512 \exp(-2\beta r)]$ ; one parameter) and  $F$  is the embedding function, which provides the many-body effect.  $F$  is chosen to give exact agreement with the experimental lattice constant, cohesive energy and bulk modulus. A best fit to the three elastic constants, the vacancy formation energy, and the diatomic bond length and bond energy is found by searching in the five-parameter space (while requiring  $E(\text{f.c.c.}) < E(\text{h.c.p.}), E(\text{b.c.c.})$ ) for Al and Ni. For an alloy system, eqn. (1) is modified so that  $\phi(r)$ ,  $\rho(r)$  and  $F$  depend on atom type. A Ni–Al cross-potential (Morse) is

determined by optimizing a fit to the lattice parameter and cohesive energy of  $NiAl$  and  $Ni_3Al$ , as well as to the elastic constants, stacking-fault energy and antiphase boundary energies of  $Ni_3Al$  and to estimates of its ordering energy and vacancy formation energy. The resulting potential is capable of describing pure Ni, pure Al, diatomic  $Ni_2$ , diatomic  $Al_2$ , and  $Ni_3Al$  ( $L1_2$ ).

The relaxed structure was obtained using a code based on the DEVIL code developed by Norgett, Perrin and Savino (1972). This code is based on the conjugate-gradient method and has been modified to allow for the local-volume term in the potential. For the calculation an atomic block is simulated by the atomic coordinates. Periodic boundary conditions were employed in the plane of the interface. The model contains at least 60 atomic planes parallel to the interface. The relative translation of the two grains was determined such that a minimum in energy was obtained. This implies that far from the interface the grains were strain free.

### §3. RESULTS

#### 3.1. General results

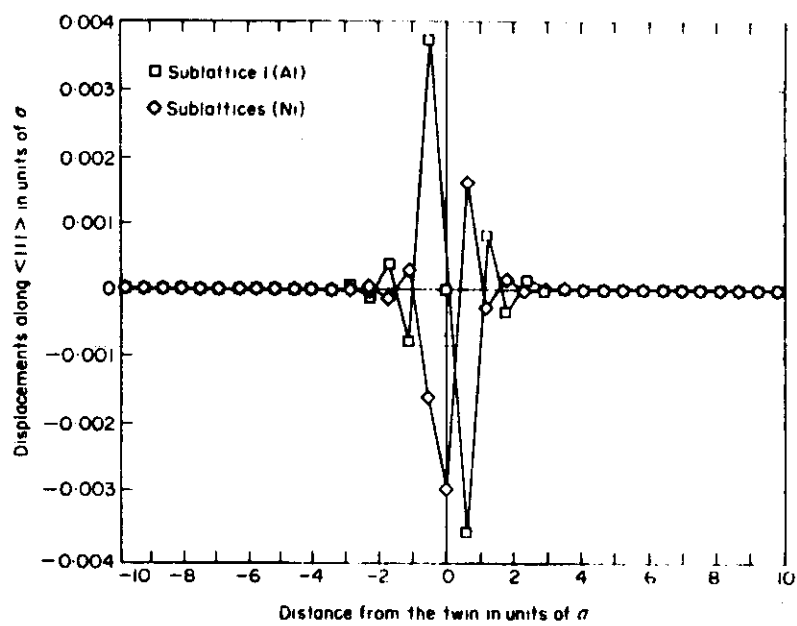
Various (111) planar defects were simulated and their energies are reported in the table in some cases. Rigid-body displacements of atoms at one side of the fault with respect to those at the other were observed. In the direction perpendicular to the (111) plane in  $Ni_3Al$ , the distortions consist of both acoustic and optical displacement modes (Savino and Farkas 1988). For some defects (i.e. a twin boundary), only optical distortion modes are observed in directions parallel to the defect plane. In these cases the Al atoms in the alloy were not displaced at all. Acoustic modes also appear in directions parallel to the (111) plane when the symmetry in these directions is broken. It is important to note (see the table) that the energy calculated for the twin boundary is indeed very small compared with the antiphase boundary energy and is even smaller than that of the superlattice intrinsic stacking fault (these two latter defects were part of the set considered in the development of the potentials).

Energies of various (111) planar defects.

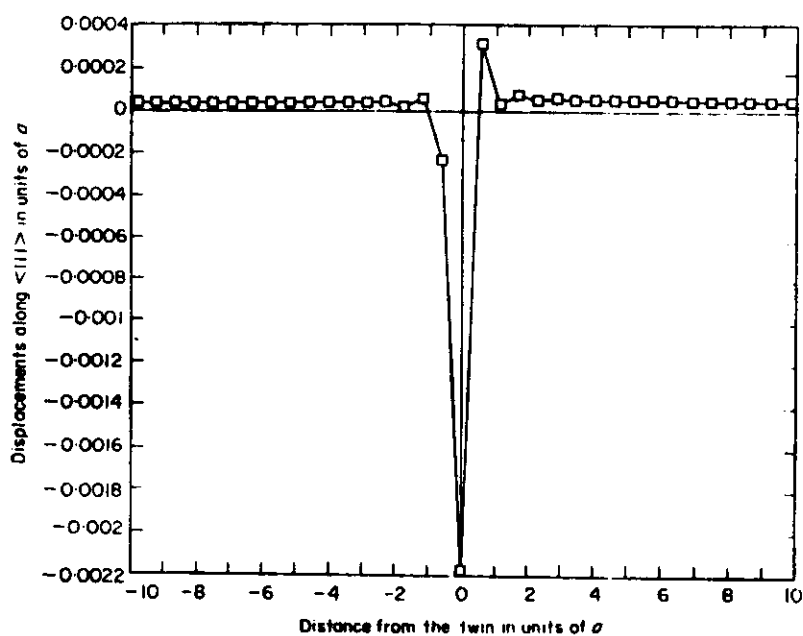
Defect	Rigid-body displacement (units of $a$ )	Acoustic mode	Optical mode	Energy ( $mJ m^{-2}$ )
Surface, $Ni_3Al$	---	[111]	All directions	1750
Twin boundary, $Ni_3Al$	-0.006	[111]	All directions	6.5
Superlattice intrinsic stacking fault $Ni_3Al$ †	-0.006	[111]	All directions	13
Antiphase boundary $Ni_3Al$ †	0	[111][112]	All directions	142
Twin boundary, Ni	+0.0056	[111]	—	29
Twin boundary, Al	+0.0163	[111]	—	46
Stacking fault, Ni	+0.006	[111]	—	59
Stacking fault, Al	+0.02	[111]	—	81

† Defects considered in the development of the potentials.

Fig. 1.

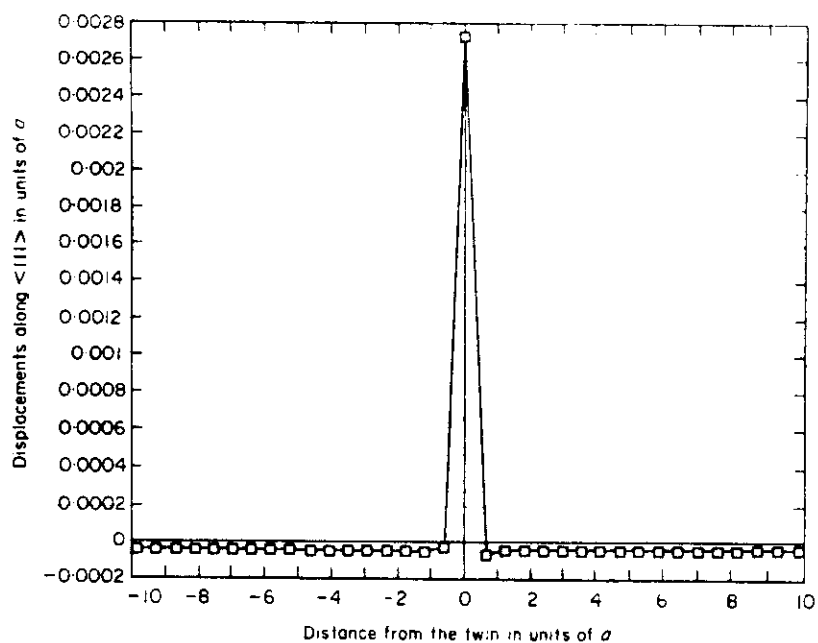


(a)

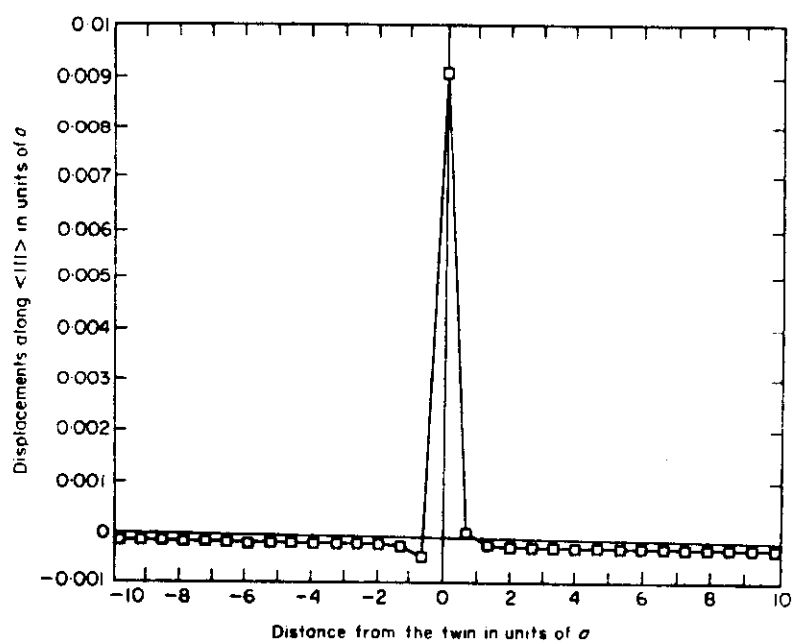


(b)





(c)



(d)

Atomic displacements perpendicular to a (111) twin boundary: (a) total displacements; (b) acoustic displacements; (c) displacements for pure Ni; (d) displacements for pure Al.

### 3.2. Twin boundary

For the (111) twin boundary, the (111) plane is a mirror plane. The twin has the lowest energy of all the planar defects considered here. The rigid-body displacement is  $-0.006a$  for  $\text{Ni}_3\text{Al}$  in the direction perpendicular to the boundary (i.e. there is a lattice contraction with the twin). This is in contrast with the *positive* displacement observed for pure Ni and Al (see table). Figure 1 shows that distortions perpendicular to the twin plane exist in addition to the above-mentioned rigid-body displacement. In this direction it can be seen that oscillatory distortions are superimposed on the non-oscillatory distortion. As shown in fig. 1, the acoustic mode is of the same general nature as but of opposite sign to that obtained in calculations for the pure metals, also shown in fig. 1.

Figures 2 and 3 show the observed displacements in the directions parallel to the twin plane. The Al atoms, which are located on sublattice 1, are not displaced at all in these directions. The Ni atoms displace differently, depending on their sublattices; however, their centre of mass remains fixed, as expected on symmetry grounds. In the [112] direction, the three Ni sublattices move, one of them with an amplitude which is opposite and twice that of the other two. In the [110] direction the Al sublattice and one of the Ni sublattices do not move, while the remaining two move with equal amplitudes but in opposite directions. Note that in the [112] direction the oscillatory displacements of a sublattice do not change direction at the boundary, whereas in the [110] direction they do.

Figure 3 shows displacements plotted for the twin plane and the planes immediately above and below. It can be seen as a contraction of the Ni atoms ordered into groups of three in the twin plane. Each of these three atoms moves toward the centre of the triangle, away from the Al atoms on the planes immediately above and below the twin plane. Since the Ni atoms in the twin plane leave more space for the Al atoms in the planes immediately above and below the twin plane than in the perfect crystal stacking, this defect can contract by a rigid-body displacement perpendicular to the twin plane. Such a contraction is, in fact, observed (see the table).

### 3.3. Superlattice intrinsic stacking fault

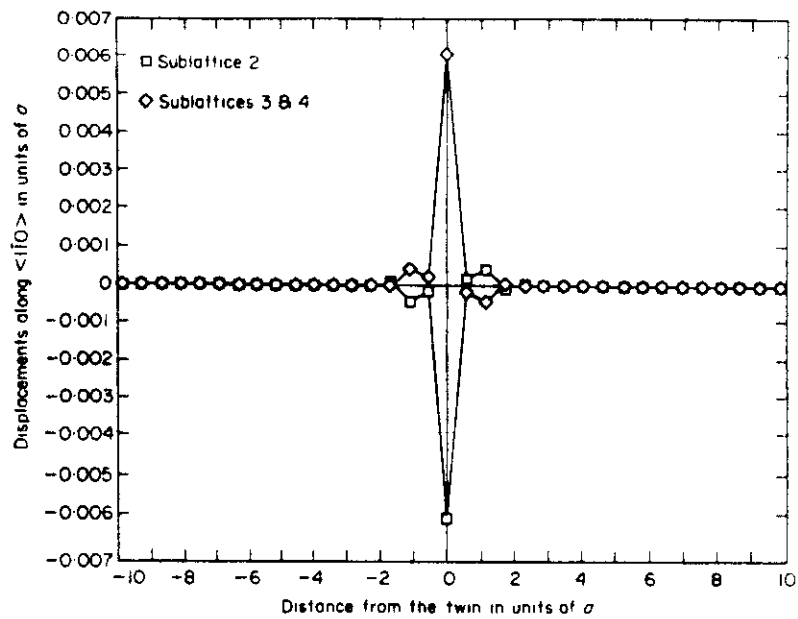
The rigid-body displacement observed for the superlattice intrinsic stacking fault in the direction perpendicular to the fault plane is a contraction of  $-0.006a$ . This is again contrary to the expansion found in pure Ni and Al (table). Oscillatory displacements perpendicular to the fault were also observed as for the twin. When separated into optical and acoustic modes, the acoustic part coincides with the result for the pure metals.

The modes parallel to the surface are all optical and resemble those for the twin boundary for which the local structure of the defect in the first planes adjacent to the fault is the same. These distortions are shown in fig. 4 as a function of the distance from the fault. Note that in this case the sign of the optical distortion changes at the fault plane. This means that triangles at both sides of the fault contract (fig 5). As for the twin, the optical distortions in the plane of the fault permit the contraction of this defect.

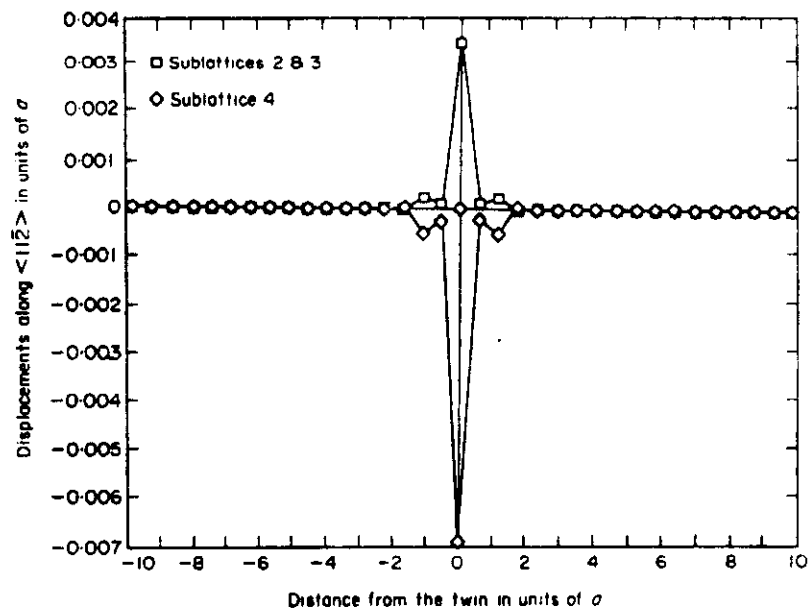
### 3.4. Antiphase boundary

No rigid-body displacement perpendicular to the boundary was observed for the antiphase boundary. Figure 6 shows the calculated displacements plotted in the (111) plane. This figure shows that, although the [112] direction is parallel to the boundary plane, a component of the acoustic type still occurs in this direction. The main reason

Fig. 2.



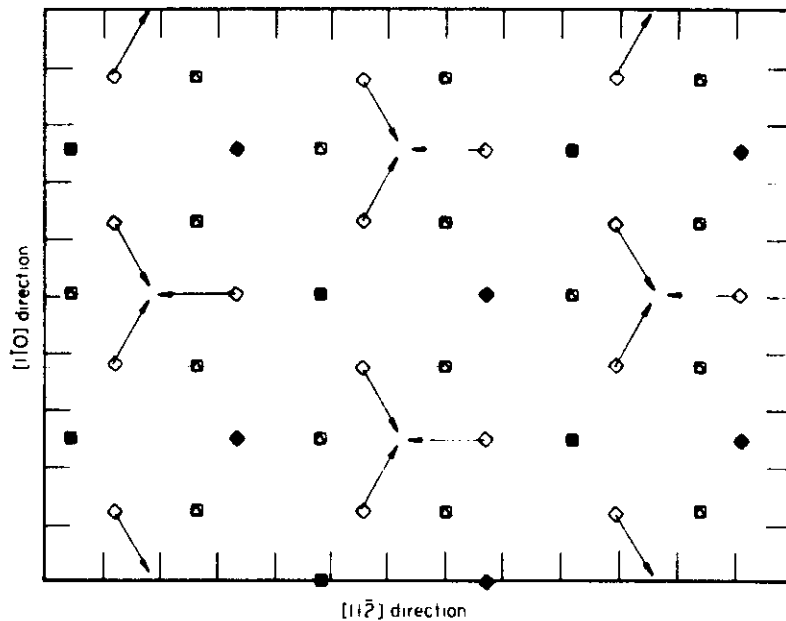
(a)



(b)

Atomic displacements of Ni sublattices in directions parallel to the (111) twin boundary (a) along  $[1\bar{1}0]$  and (b) along  $[1\bar{1}2]$ . The Ni sublattices are numbered from 2 to 4.

Fig. 3.



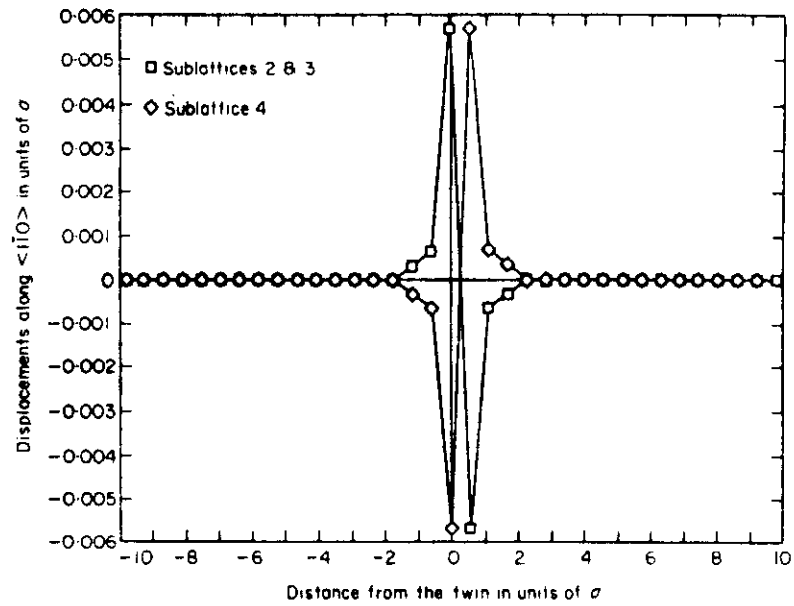
Projection of the first two planes adjacent to a (111) twin boundary: □, plane above twin; ◇, plane below twin; ◇, twin plane. The calculated atomic displacements are magnified 100 times and full symbols represent the Al atoms.

for this is that the defect introduces Al-Al bonds not present in the bulk. Relaxation is such that the Al-Al bond lengths are increased. The observed shear distortion contributes to this increase in bond length. A similar tendency for increasing bond length is obtained from the perpendicular displacements of Al. These displacements present both optical and acoustic modes. The minimum Al-Al bond length is increased from the 0.252 nm in the unrelaxed boundary to 0.262 nm in the relaxed structure. This is not the case for the Ni sublattices, which show little change in the Ni-Ni bond length upon relaxation. Whereas in the  $[1\bar{1}0]$  direction only the optical mode is present (fig. 7(a)), both acoustic and optical modes appear in the  $[11\bar{2}]$  direction (fig. 7(b)). The optical mode in the  $[11\bar{2}]$  displacements differs from those in the previous defects, because the Al sublattice is now also affected by the oscillations. However, if the Ni and Al atoms are treated separately, by computing the displacements of the three Ni sublattices with respect to their centre of mass, the same distortion mode observed for the other defects is obtained. Figure 7(c) shows the Ni acoustic mode in the  $[11\bar{2}]$  direction.

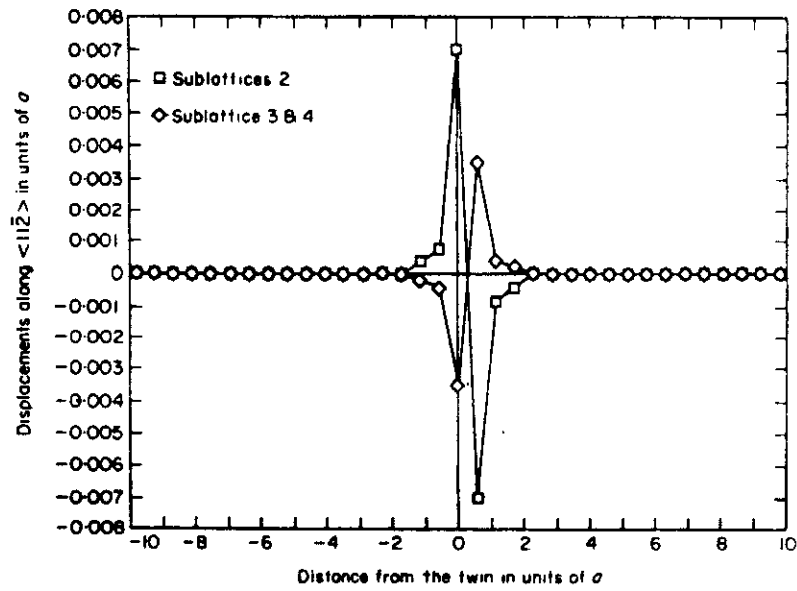
### 3.5. Free surface

Oscillatory behaviour in the direction perpendicular and parallel to the  $\text{Ni}_3\text{Al}(111)$  free surface was previously observed by Chen *et al.* (1986a) and Savino and Farkas (1988) using the same potentials. This is different from the (111) faces of pure Ni and Al which present no oscillatory behaviour. Figure 8 shows the parallel

Fig. 4.



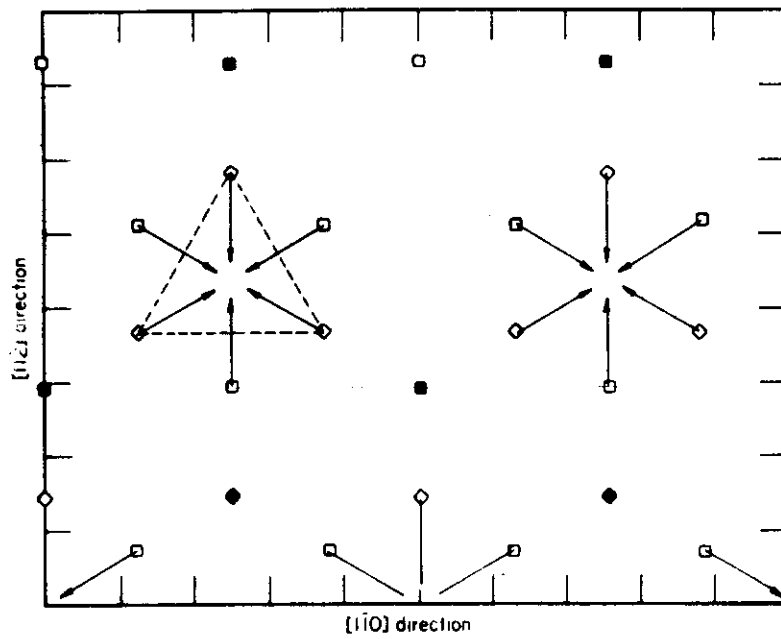
(a)



(b)

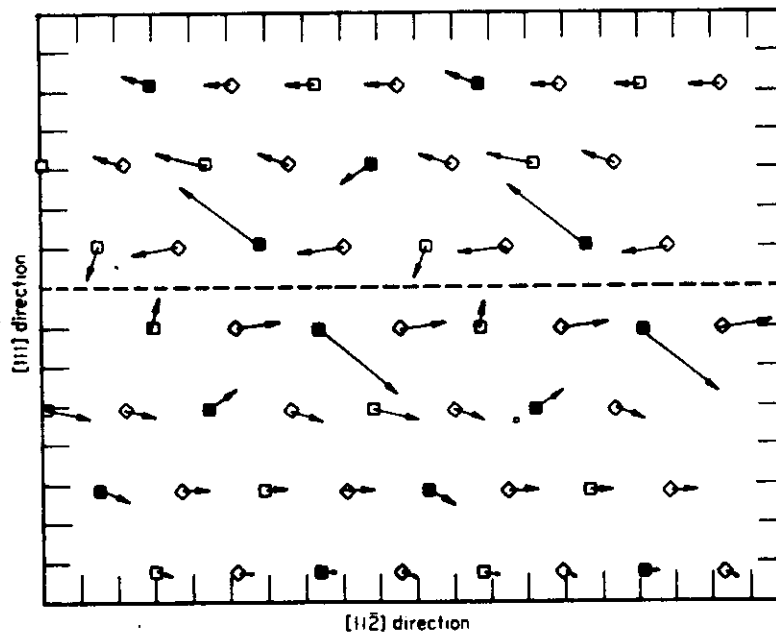
Atomic displacements parallel to a superlattice intrinsic stacking fault: (a) along  $[1\bar{1}0]$ ; (b) along  $[11\bar{2}]$ .

Fig. 5.



Projection of the first two planes adjacent to a superlattice intrinsic stacking fault with observed displacements magnified 100 times: □, plane above fault; ◇, plane below fault.

Fig. 6.



[110] projection of the antiphase boundary with displacements magnified 50 times: □, one plane; ◇, two planes.

relaxation of the first (111) planes near to the surface. While there is no displacement of the Al atoms parallel to the surface plane, the three Ni sublattices exhibit the same oscillatory relaxation mode observed for the previous defects. It can be seen in fig. 8 that at the surface plane the Ni atoms in groups of three contract towards the centre of the equilateral triangle that each group forms. Note that at the outer surface plane the centre of the triangle corresponds to a position where an Al atom would be located on the (111) plane immediately above in a perfect bulk material. On the other hand, the displacements are such that the triangle of Ni atoms located immediately below the surface expands.

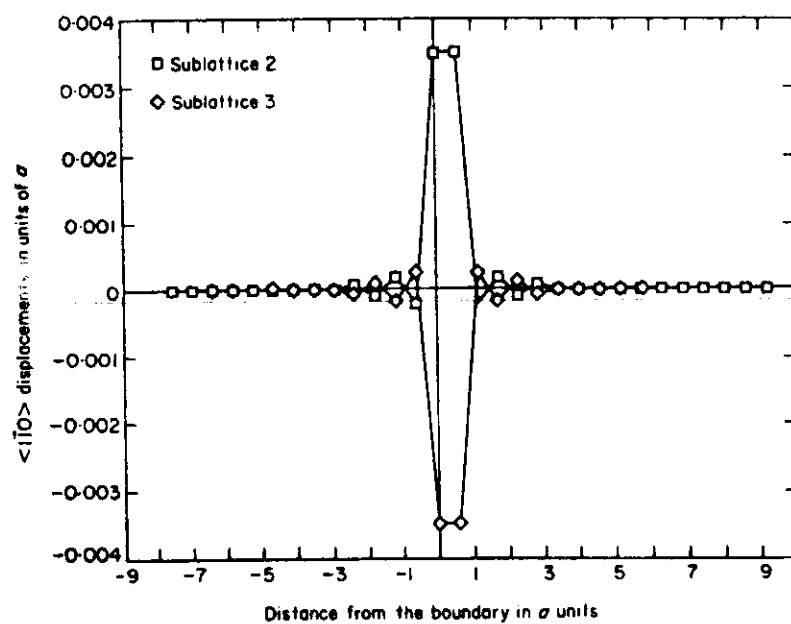
#### §4. DISCUSSION

Savino and Farkas (1988) reported calculations of oscillations in the static relaxation parallel to a planar free surface in pure metals and alloys. These oscillations can also be seen in fig. 2 of Chen *et al.* (1986a, 1987a). Parallel as well as perpendicular oscillations are related to the fact that the energy of the system depends on both the local-density and the pair ion-ion interaction. At the free surface there is a change in the density due to the absence of atoms. Volume-dependent and pair interaction forces appear over the surface atoms. Under both sets of forces the first interatomic layers relax and, as a consequence, the density around atoms at inner layers also varies. Volume-dependent forces appear on those inner atoms as a consequence of this change in density. The resulting distribution is clearly oscillatory in the displacements perpendicular to the free surface. Even in pure metals, for free surfaces of reduced symmetry, oscillations in the displacements parallel to the surface may also appear. For the case of (111) interfaces only, perpendicular relaxations are to be expected in pure metals. For the case of  $\text{Ni}_3\text{Al}$  ordered alloys, we report in this paper 'optical' and 'acoustic' relaxation modes. The first of these is parallel and the second may be both parallel and perpendicular to the interface. The present study shows that the two modes can appear together, but they can be separated. When this is done, the observed acoustic distortion resembles that obtained for pure metals. The existence of the optical distortion is due solely to the presence of an *ordered* lattice. The optical distortions strongly influence the atomic configurations of the defect cores. For example, the optical distortion in the twin boundary plane is a major component of the relaxation around the Al atoms in the planes adjacent to boundary. This results in a rigid-body displacement that is different from those found in pure metals, namely an average lattice compression instead of expansion.

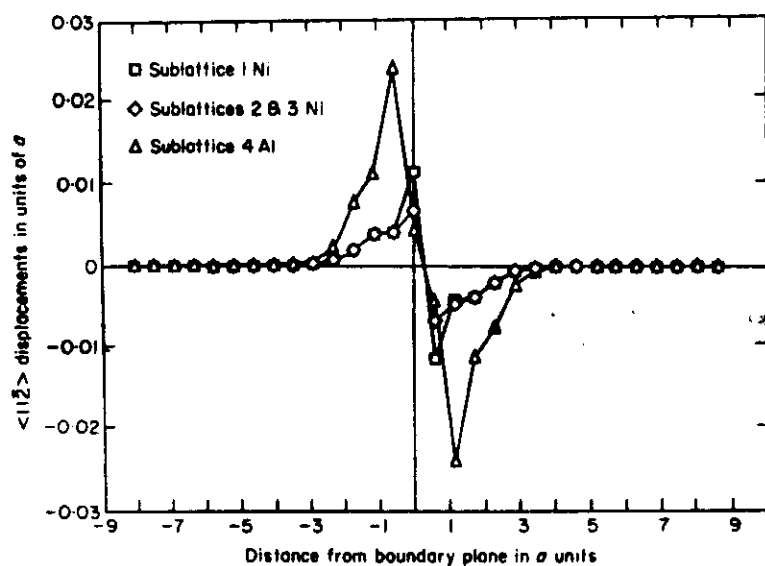
Local distortions of the optical type may also have important implications for the segregation of interstitial impurities to these defects. The present results indicate that some interstitial sites will be significantly expanded. These sites can become preferential segregation sites. For cases where the defect is bounded by partial dislocations, such modification of the segregation properties will have a strong effect on the Suzuki locking of these dislocations (Hirth and Lothe 1982).

The optical distortion modes in the (111) plane have a similar nature in all the defects studied, namely, the expansion (or compression) of nearest-neighbour triangles in the plane. This optical distortion is transmitted in an oscillatory fashion from plane to plane in the direction perpendicular to the defect plane.

Fig. 7.

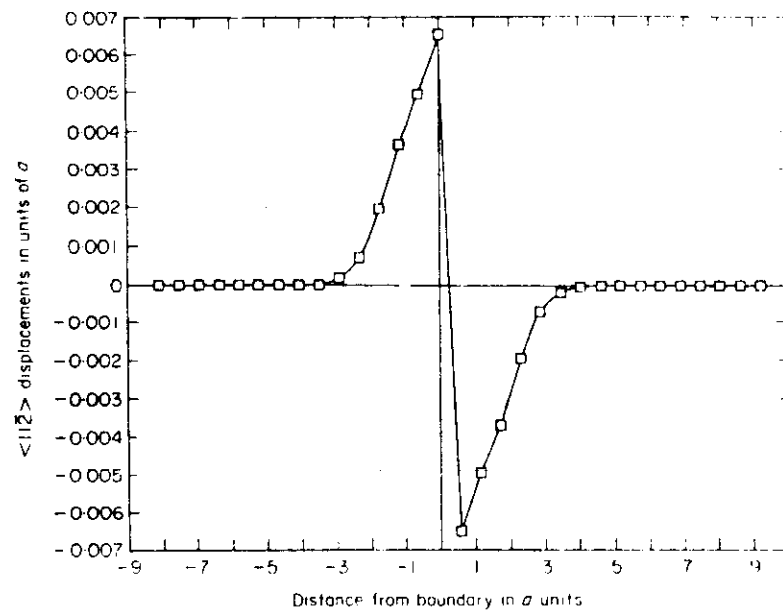


(a)



(b)

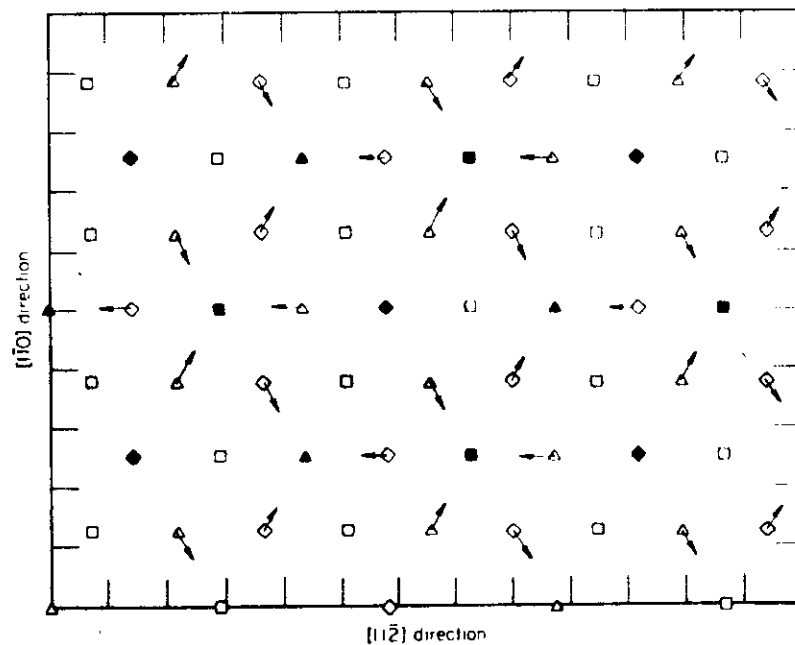




(c)

Atomic displacements parallel to a (111) antiphase boundary: (a) along  $[1\bar{1}0]$ ; (b) total displacements along  $[11\bar{2}]$ ; (c) Ni acoustic mode along  $[11\bar{2}]$ .

Fig. 8.



Projection of the first (111) planes in the surface region, with calculated displacements magnified 50 times:  $\Delta$ , surface plane;  $\diamond$ , one plane below surface;  $\square$ , two planes below surface.

## ACKNOWLEDGMENTS

This work (D.F., E.J.S. and P.C.) was supported by the Department of Energy, Energy Conversion and Utilization Technologies (ECUT) program under Subcontract 19X-89678V with Martin Marietta Energy Systems Inc. and was monitored by Oak Ridge National Laboratories. A.F.V., D.J.S. and S.P.C. were supported by the ECUT program through Los Alamos National Laboratory.

## REFERENCES

- CHEN, S. P., VOTER, A. F., and SROLOVITZ, D. J., 1986, *Phys. Rev. Lett.*, **57**, 1308; 1986b, *Scripta metall.*, **20**, 1389; 1987a, *Characterization of Defects in Materials*, Materials Research Society Symposium Proceedings, Vol. 82 (Pittsburgh, Pennsylvania: Materials Research Society), p. 515; 1987b, *High Temperature Ordered Intermetallic Alloys II*, Materials Research Society Symposium Proceedings, Vol. 81 (Pittsburgh, Pennsylvania: Materials Research Society), p. 45; 1987c, *J. Phys., Paris* (to be published).
- DAW, M. S., and BASKES, M. J., 1984, *Phys. Rev. B*, **29**, 6443.
- FARKAS, D., and RAN, A., 1986, *Phys. Stat. sol. (a)*, **93**, 45.
- HILES, S., and DAW, M. S., 1987, *J. Mater. Res.*, **2**, 5.
- HIRTH, J. P., and LOTHE, J., 1982, *Theory of Dislocations* (New York: Interscience).
- LIU, C. T., WHITE, C. L., and HORTON, J. A., 1985, *Acta metall.*, **33**, 213.
- NORGETT, M. J., PERRIN, R. C., and SAVINO, E. J., 1972, *J. Phys. F*, **2**, L73.
- SAVINO, E. J., and FARKAS, D., 1988, *Phil. Mag. A*, **58**, 227.
- VOTER, A., and CHEN, S. P., 1987, *Characterization of Defects in Materials*, Materials Research Society Symposium Proceedings Vol. 82 (Pittsburg, Pennsylvania: Materials Research Society), p. 175.
- YAMAGUCHI, M., PAIDAR, V., POPE, D. P., and VITEK, V., 1982, *Phil. Mag. A*, **45**, 867.

# CORE STRUCTURE OF STRAIGHT DISLOCATIONS IN Ni<sub>3</sub>Al

R. Pasianot, D. Farkas and E.J. Savino<sup>1</sup>  
Department of Materials Engineering,  
Virginia Polytechnic Institute  
Blacksburg, VA 24061

## Introduction

In our previous work (1) we have simulated the atomistic structures for the core of the  $1/2[1\bar{1}0]$  screw superpartials bounding an Anti Phase Boundary (APB) on the (111) plane. For all the configurations tested in that work, the structure obtained was non-planar, with the core of the partials spread in the (111) plane and not in the (111) plane of the APB. In that work we used local volume interatomic potentials for Ni<sub>3</sub>Al developed by Voter et al. (2). Using similar interatomic functions, Yoo et al. (3) obtained a planar core structure, where both superpartials split into Shockley dislocations on the APB plane, in addition to the non-planar structure obtained by us. Those authors also claimed that the planar structure is the stable one. This conclusion agrees with the discussion presented by Yamaguchi et al. in their already classical work (4). Those authors used pair interaction potentials for simulating the dislocation core plus linear elastic theory for inferring the minimum energy dislocation configuration. Yoo (5) also calculated the elastic interaction energy of the two screw superpartials in an anisotropic continuum approximation and found torque forces on the superpartials. He proposed that a momentum force distribution must be applied on the APB plane to compensate those forces. In the present work we tackle two main questions: the solution of the elastic distortion field of the dislocations in equilibrium with the corresponding plane fault regions of the crystal, and the relation between elastic predictions and computer simulated structures. Therefore, by using Stroh's anisotropic elastic solution for the dislocation fields (6), we calculate the equilibrium configurations for the two  $1/2[011]$  superpartials when they split into the corresponding  $1/6[112]$  Shockley partials. Afterwards, we study, within a computer simulation approximation, the above mentioned planar and non planar dislocation core structures as well as others that can be obtained with different choices of the initial elastic configuration used for the relaxation procedure. All of them represent possible minimum energy configurations which are consistent with the boundary Volterra elastic dislocation field.

## Results

### *Elastic Model*

Elastic calculations are performed for the several possible configurations of the dissociated dislocation bounding an APB region along the (111) plane. For model purposes, two pure screw partial dislocations of the type  $1/2[1\bar{1}0]$  are assumed. Furthermore, each partial is dissociated in Shockley ones with a Complex Stacking Fault (CSF) in either (111) or (111) planes. Stroh's anisotropic elastic solution for the straight dislocation field (6) is used. The system equilibrium is obtained by minimizing the sum of the energy of APB and CSF regions lying on compact (111) planes, plus the work done in creating each dislocation in the field of the others (6). Fig. 1 shows, in a schematic way, the degrees of freedom allowed to the whole structure, i.e., X, Y, Z and W. These are respectively, X and W: the CSF region width for the corresponding superpartial, Y: the distance measured on a (111) plane between the superpartial center and the APB plane and Z: the APB width. Some results for the calculations are reported in Table I. Y is not reported in that table

<sup>1</sup> Permanent address: Comisión Nacional de Energía Atómica, Av. Libertador 8250, 1429 Buenos Aires, Argentina

because it either results  $Y=0$  for the planar superpartials or  $Y=X/2$  for the non planar case. This situation is clearly depicted in the insets and is a consequence of the extra energy needed to extend the APB area outside the (111) plane. The non planar core constitutes a zig-zag shape configuration. We perform the calculations using different values for the elastic constants and the APB/CSF energy ratio. For the elastic constants we use either the experimental ones, or those fitted by Voter et al.'s interatomic potential. As it is believed that for  $\text{Ni}_3\text{Al}$  the CSF energy may be larger than the APB energy, in contradiction to the interatomic potential prediction, we also perform a set of calculations increasing that value. Some results are summarized in Table I.

Yoo (5) carried out elastic calculations and concluded that a torque force appears on the two  $1/2[011]$  superpartials. Our elastic calculations are consistent with this result in that the above mentioned zig-zag shape is obtained as a minimum energy configuration. That shape is produced by the sliding of the partials driven by the competition between the torque force and the radial repulsion. Whenever the torque force dominates the sliding is anticlockwise, whereas the clockwise sense is only allowed for relatively large radial forces. For relatively large CSF energy, a small separation between the Shockley partials will reduce that force; therefore, on increasing this energy value, some configurations may not be found. In turn the torque force is proportional to the anisotropy ratio  $A$  ( $A = 2c_{44}/(c_{11} - c_{12})$ ). This implies that, for relatively large values of that ratio, the above same configurations are not favored, see Table I.

### Computer Simulation Results

The computer simulations are carried out in the usual way (1). The atomic coordinates inside a crystal region I, containing the defect core, are allowed to relax in order to find an energy minimum consistent with the boundary atoms position at a region II where anisotropic elasticity is used. We study the configurations 1, 2 and 4 in Table I and they are respectively called hereafter planar, non planar and mixed configuration. We first study the minimum required size of region I, where the atomic coordinates are free to relax under the interatomic potential. A minimum size for that region is needed to insure that the elastic solution in the fixed region II does not affect the calculated core structures. This size is determined by plotting the energy differences between the initial elastic configuration and the final relaxed configuration for two increasingly larger cylindrical regions centered in the dislocation lines. Outside the core region, where the harmonic solution for the atomic displacements is valid, this difference should approach a straight line corresponding to the relaxation energy of the APB. The method provides at the same time an estimate of the core size. The plot corresponding to the non planar dislocation is shown in Fig. 2 and it implies in this case a core size for each superpartial of 1.5 to 2 nm. The relaxation energy of the APB is very small and the slope is not detected in the plot of Fig. 2.

As already pointed out by other authors (3), even for calculations performed with over 15000 atoms in region I, the core centers of the superpartials do not seem to move during the simulations. One expects they would do so by trying to converge towards a minimum energy separation. Actually we always find their location to be determined by the elastic solution in region II. Therefore, for finding the equilibrium separation between the partials, we compute the energy of the simulation block, region I, for different values of that distance and add in each case the corresponding elastic energy of a continuum outside the block, up to a square of  $0.2 \mu\text{m}$ . The calculated energy values are plotted in Figure 3. The optimum separation corresponds to the minimum in those curves. On the other hand, all the superpartial structures tested split by themselves into two Shockley dislocations, and the corresponding CSF width does not seem to be strongly dependent on the boundary conditions. Also, as suggested by our elastic model, for the non planar and mixed configurations the location of the superpartials must be varied on the (111) plane complementary to the APB plane. However, with respect to the location of the partials, we note that, in a non planar configuration, the boundary conditions impose that they do not move to be at different heights with respect to the APB unless the APB is created with the corresponding zig-zag shape. This must be done in the starting, elastic, configuration for the computer simulation. Therefore, we modify the initial elastic solution so that the branch cut for the logarithmic term follows a chosen set of planes between the dislocation centers. In this way the APB shape is part of the input. The minimum energy relaxed configuration shows an asymmetry in the partial position with respect to the APB plane. Although this is not so pronounced as predicted by the elastic solution, it is shown below that it is still noticeable.

The planar core is the lowest energy configuration among those tested, as shown in Figure 3. For the mixed and non-planar structures, we find respectively an extra energy of 0.1 eV/nm and 0.5 eV/nm relative to the planar core one. The non-planar core computed in our previous work is 6.6 eV/nm higher. This extra energy in energy results by allowing the superpartials slip outside the APB plane. As shown in Figure 3, the calculated separation among partials is about 6 nm for the planar and mixed cores and about 5 nm for the non-planar core. This is in qualitative agreement with the elastic results.

From the relaxed atomic configuration the continuum strain tensor  $E_{ij}$  can be calculated. In Fig. 4 two invariants of that tensor are plotted using contour line graphs. Fig. 4.a plots the quantity  $2(E_{xx}^2 + E_{yy}^2)$  and Fig. 4.b plots  $E_{xx}^2 + E_{yy}^2 + 2E_{zz}^2$ . Both quantities are invariant under rotations about the dislocation line (the  $z$  axis). Since (110) is a mirror plane, the first quantity is related only to the screw components and the second one to the edge components of the dislocation. In Figure 4, the dissociation of the superpartial dislocation into Shockley partials, as well as the above mentioned asymmetry of the superpartial center location with respect to the APB plane, can be seen. It is also noticed that the edge components are more closely spaced than the screw components and that their distortion fields show a large overlapping.

#### Discussion

Different choices for the elastic center of the dislocation in the computer simulation procedure can lead after relaxation to different core structures. This is so because the elastic solution acts not only as the boundary condition but also as the initial configuration for the minimization procedure, enforcing therefore the convergency to a given configuration. This situation is fully exploited in this work to obtain the different dislocation structures discussed above. We find that, by a proper choice of the boundary initial elastic configuration, different dislocation structures can be simulated for the same superpartial dislocation, APB plane and interatomic potential. Among those are the planar and non planar structures mentioned in the Introduction plus a mixed configuration, not reported previously, where one of the partials spreads in the plane of the APB while the other does so in another (111) plane. This mixed configuration may be important for the understanding of pinning-unpinning mechanisms. Also that configuration has an energy of only 0.1 eV/nm higher than the global energy minimum, which we find to be the planar core configuration. The global energy minimum configuration agrees with the one predicted by the classical work of Yamaguchi et al.(4), and by Yoo et al.(3). We also find a non-planar configuration in which the left partial is located below the APB plane whereas the right partial is located above it. The overall dislocation core takes then a zig-zag shape. This type of core has lower energy than the non-planar core reported in our previous work (1). The fact that the partials can move on the complementary APB plane results in a decrease of the energy for the non-planar core.

As said in the Introduction, in an elastic model Yoo (5) found a torque force to exist for the  $\frac{1}{2}[111]$  superpartials dissociation when they are located on the APB plane. We have developed above a simple model based on anisotropic elasticity, that allows us to predict, among other parameters, the location of the superpartials and Shockley dislocations at equilibrium with the corresponding APB and CSL areas. That model imposes the displacement of the partials as a necessary condition for finding the minimum energy position. The partials move as a consequence of the radial forces repelling one another and the torque force mentioned above. Those forces are therefore relaxed by the displacement of the partials outside the APB plane. The existence of opposite forces gives rise to more than one stable mixed and non planar configuration with the partials splitting into different (111) planes. For a relatively large anisotropy ratio  $A$ , the torque force always dominates and only one configuration is found for each of those cases. The trends on the dislocation configuration predicted by elasticity are confirmed by the computer simulations. Planar, non planar and mixed configurations are calculated. The dislocation dissociation widths nearly agree with the elastic predictions. However, in the computer simulation the calculated center of the non planar superpartial always appears nearer the APB plane than predicted by elasticity.

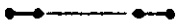
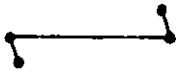
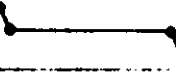
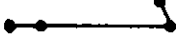
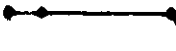
#### Acknowledgements

This work was supported in part by the Office of Naval Research, Division of Materials Sciences and by the U.S. Department of Energy, Energy Conversion and Utilization Technologies (ECUT) program under sub-contract No. 19X-89678V with Martin Marietta Energy Systems Inc. and was monitored by Oak Ridge National Laboratories. Partial support was also provided by the National Science Foundation, Division of International Programs and CONICET, through a collaborative research grant. We gratefully acknowledge A.F. Voter for the use of the interatomic potentials.

### References

1. D. Farkas and E. I. Savino, Scripta Metall. 22, 557 (1988)
2. A. F. Voter and S. P. Chen, MRS Symposium Proc. 82, 175 (1987)
3. M. H. Yoo, M. S. Daw and M. I. Baskes in "Atomistic Simulation of Materials", pag. 401, Ed. by V. Vitek and D. J. Srolovitz, Plenum Press, N.Y. 1989.
4. M. Yamaguchi, V. Paidar, D. P. Pope and V. Vitek, Phil. Mag. A45(5), 867 (1982)
5. M. H. Yoo, Acta Metall. 35(7), 1559 (1987).
6. A. N. Stroh, Phil. Mag. 3, 625 (1958).

Table 1: Elastic Model Results

	(a)*			(b)*			(c)*		
	X[nm]	Z[nm]	W[nm]	X[nm]	Z[nm]	W[nm]	X[nm]	Z[nm]	W[nm]
	----	4.17	1.83	----	5.17	0.71	----	3.78	1.49
	1.09	5.43	----	0.51	5.75	----	1.00	4.63	----
	0.94	5.69	----	0.49	5.82	----	not found		
	0.97	5.02	1.69	0.50	5.49	0.70	0.87	4.40	1.39
	0.89	5.10	1.69	not found			not found		

\*using the parameters given by the interatomic potentials

$c_{11} = 246, c_{12} = 137, c_{44} = 123$  [GPa];  $\gamma_{APB} = 142, \gamma_{CSF} = 121$  [mJ/m<sup>2</sup>]

\*(b) same as in (a) but with  $\gamma_{CSF} = 213$  [mJ/m<sup>2</sup>]

\*(c) using the experimental elastic constants:

$c_{11} = 230, c_{12} = 150, c_{44} = 131$  [GPa];  $\gamma_{APB} = 142, \gamma_{CSF} = 121$  [mJ/m<sup>2</sup>]

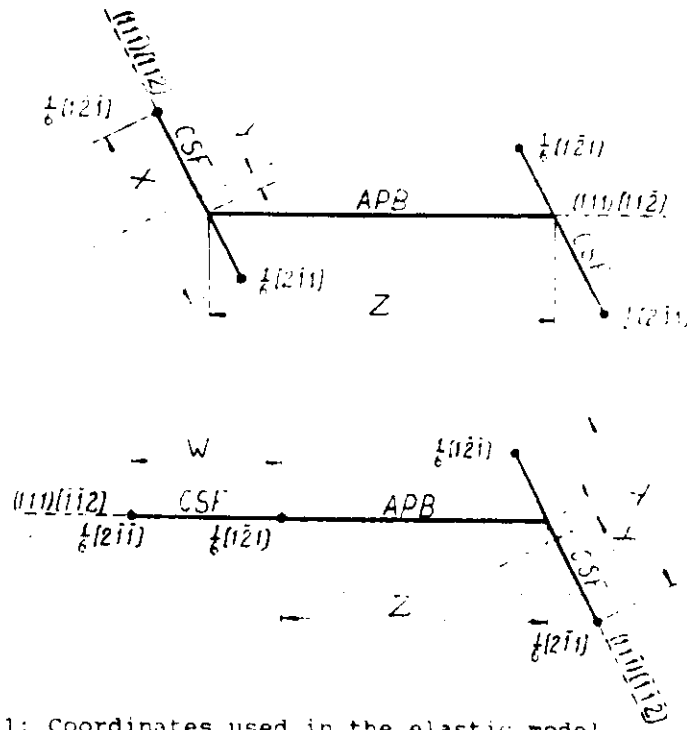


Fig. 1: Coordinates used in the elastic model

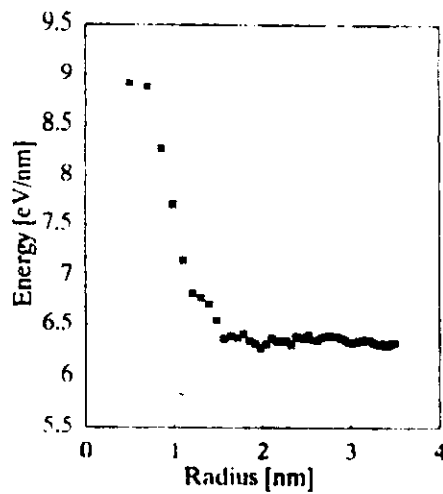


Fig. 2: Energy difference between relaxed and starting (elastic) core configurations

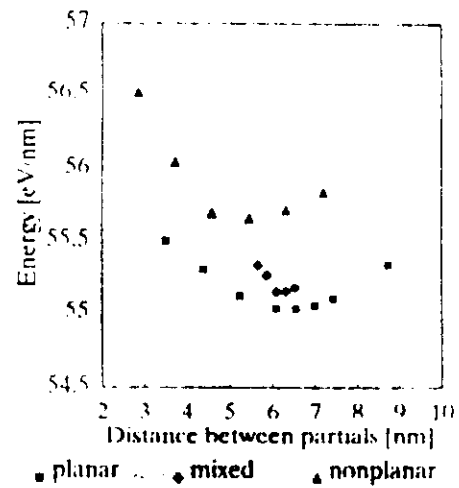
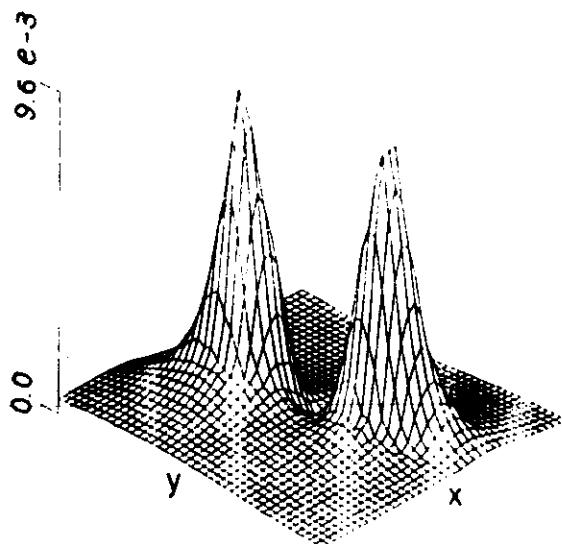
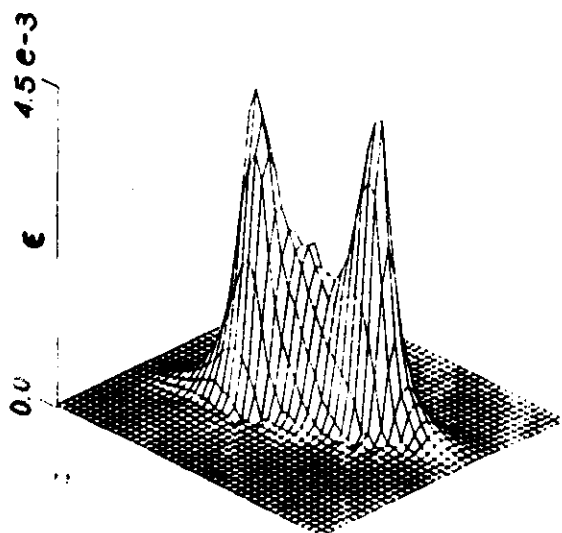
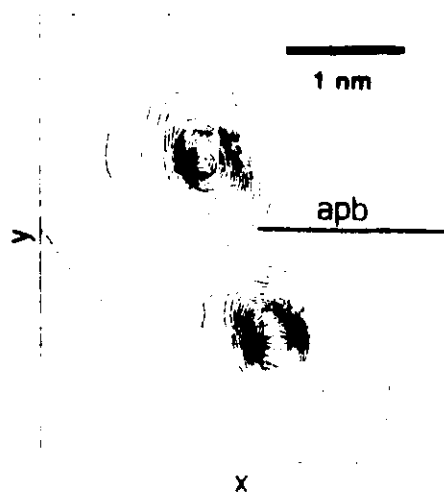


Fig. 3: Core energies as a function of superpartial separation



a



b

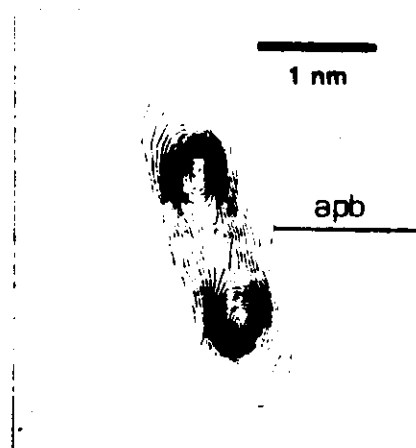


Fig. 4: Strain invariants for (a): screw components and (b): edge components, in the left superpartial of the nonplanar structure



# COMPARISON OF TEM OBSERVATIONS WITH DISLOCATION CORE STRUCTURE CALCULATIONS IN B2 ORDERED COMPOUNDS

D. Farkas, R. Pasianot, E. J. Savino and D. B. Miracle \*

Department of Materials Engineering, Virginia Polytechnic Institute and State University, Blacksburg, VA. 24061.

\* Wright Patterson AFB Dayton, OH 45433

## ABSTRACT

Dislocation core structures have been calculated using atomistic computer simulations in NiAl and other B2 compounds. In the present work the calculated dislocation core structure are correlated with the known deformation behavior of B2 alloys. It is found that for the high ordering energy compounds  $\langle 111 \rangle$  dislocations do not split in the simulations, in agreement with the experimental observations. It is also found that core structures for certain  $\langle 111 \rangle$  and  $1/2 \langle 111 \rangle$  dislocations are spread in  $\{112\}$  planes, which is consistent with the slip plane often reported for these dislocations. For the  $\langle 100 \rangle$  dislocations several orientations of the dislocation line produce sessile core configurations, whereas other orientations produce relatively more glissile cores. However, a structural transition of each of these dislocation cores may be required before  $\langle 100 \rangle$  dislocations become mobile, and this is consistent with the limited tensile ductility observed in NiAl "soft" single crystals below 200°C. Core structure simulations for  $\langle 110 \rangle$  dislocations are also reported and are discussed with respect to the importance of these dislocations in the deformation of NiAl.

## INTRODUCTION

Since the early studies on BCC metals (1) it is clear that the dislocation core structure plays an important role in the understanding of yield behavior. More recently, this approach was able to give an explanation of the anomalous yield behavior in L1<sub>2</sub> alloys (2). The basic ingredient of these theories is that some cores are found to be non-planar and therefore sessile, whereas others are planar and therefore relatively more mobile.

The wide range of deformation behavior in B2 alloys has been correlated with the APB energy in these compounds (3). Compounds with a low APB energy, such as  $\beta$ -CuZn, exhibit  $\langle 111 \rangle$  slip from room temperature (RT) to the disordering temperature (3, 4). In FeAl, which has a higher APB energy (5), a transition from  $\langle 111 \rangle$  slip at RT to  $\langle 100 \rangle$  slip at higher temperature has been reported (6,7). Both simple considerations based on basic theories of ordering (8,9) as well as first-principles calculations (10) suggest that the APB energy in NiAl is higher than in either  $\beta$ -CuZn or FeAl, and  $\langle 100 \rangle$  is the preferred slip direction over all temperatures (11,12).

The purpose of the present work is to compare these observations with the predictions that can be inferred from the calculation of dislocation core structures using computer simulation. The material that we will discuss in the present work is mainly NiAl. We performed static (0 K) atomistic simulations of the dislocation core area using embedded atom interatomic potentials (13), which we already used to describe the B2 phase (14). The simulation method is the same as in our previous work on Ni<sub>3</sub>Al and NiAl (14,15).

We proposed recently a new way of depicting the core structure that will be briefly discussed below (15). It is directly based on the strain tensor  $\bar{E}$ , constructed using a finite difference scheme over the atomic displacements. Assuming that the dislocation line lies along the z axis, two quantities are computed, namely  $Y_1 = 2(E_{xx}^2 + E_{yy}^2)$  and  $Y_2 = E_{xx}^2 + E_{yy}^2 + 2E_{zz}^2$ . Both are invariant under rotations about the dislocation line, and have therefore scalar nature. The first invariant may be thought of as a squared mean strain involving shears along the dislocation line only, whereas the second would be a squared mean strain within the plane perpendicular to the dislocation line. For the particular case in which this plane is a plane of mirror symmetry of the crystal, or if the body is isotropic, shears due to screw dislocations do not mix with shears due to edge dislocations; therefore  $Y_1$  is only related with screw components and  $Y_2$  with edge components. Though an accurate representation of the core structure would

involve the 6 components of the strain tensor, this representation is much simpler and sufficient to identify the core shapes. Both quantities can be plotted using standard 3D graphics, and the contour plots of this surface will directly give the shape of the dislocation core, extended to different levels of deformation.

### **<111> SCREW DISLOCATIONS**

There have been several reports that these dislocations exist in NiAl as complete <111> dislocations and they do not split into superpartials with an APB either on {110} or {112} planes (11, 16). These observations are in agreement with the computed dislocation core structures and energies, as reported in our previous work (14). It was found that the energy of a block containing the two superpartials decreased as the superpartial separation decreased.

The undissociated dislocation has an internal structure that is quite complex and highly non-planar, therefore it must undergo a severe structural transformation before slip is possible. The core is more extended on {112} planes, and we expect from this result that the dislocation will be transformed to a planar structure in a {112} plane leading to slip along this plane. This process will require very high stresses. Alternatively, two branches may combine under stress to form a core structure that is planar in a {110} plane. Actually both slip systems have been reported (11) but the stresses required are extremely high, and are over 1% of the shear stress at room temperature (10, 17, 18).

### **<100> DISLOCATIONS**

B2 materials with high ordering energies typically deform by the motion of [100] dislocations (3,19), and experimental observations of <100> dislocations in NiAl, show an overall orientation near screw (11, 12). However, <100> screw dislocations are elastically unstable in NiAl, and these dislocations therefore exhibit a serrated morphology so that the screw orientation rarely exists (11). <100> dislocations are typically reported to glide on both {100} and {110} planes (11, 12, 20). Easy cross-slip of <100> dislocations onto orthogonal {110} planes has also been suggested to occur in NiAl (20).

Simulations for a number of <100> dislocation orientations, from pure edge to nearly pure screw, on the {100} and {110} planes have been performed. The specific dislocation line directions modeled are [010], [120], [110] and [210] for [100][001] slip, and [011], [122], [111] and [211] for [100] (011) slip. Figs 1 and 2 show contour maps of  $\gamma_1$  and  $\gamma_2$  for these two slip systems respectively. It is seen that in all cases the core structures have non-planar components, suggesting that high stress levels would be needed to cause slip. The magnitude and extent of the dislocation strain fields suggests that <100> dislocations may be more difficult to move on {100} planes than on {110}. Note that the critical resolved shear stress for <100> {100} slip in NiAl has been determined experimentally to be about 10% lower than the critical resolved shear stress for <100> {110} slip (21).

### **<110> DISLOCATIONS**

The role of <110> dislocations in the deformation of NiAl has not been clearly established. <110> dislocation segments have been suggested to form as the sessile reaction product of mobile <100> dislocations (22, 23), and have alternatively been reported to contribute to the deformation of NiAl (24, 25, 26). The screw orientation has been suggested to be more mobile than the edge segment, and the slip plane has been determined to be {110} (26). Our computer simulation result for the [110] screw orientation, Fig. 3(a), shows that the screw component of the strain field,  $\gamma_1$ , is largely spread on the (110) plane, and that there is a nascent dissociation of the type  $1/2[111] + 1/2[1\bar{1}\bar{1}]$  with a corresponding very narrow band of (110) APB in between. Simple elastic calculations are also in agreement with this finding. However, the edge component,  $\gamma_2$ , has some spreading on the (001) plane and this may preclude easy glide on the (110) plane. Indeed this configuration was able to stand stresses of about  $3 \times 10^{-2}$  of the shear modulus without slipping. This is the order of stresses needed in computer simulations to move  $1/2[111]$  screw dislocations in BCC materials. The same is true for the edge dislocation on the (110) plane shown in Fig. 3(b).

## DISCUSSION AND CONCLUSIONS

Core structures have been simulated for various orientations of  $\langle 100 \rangle$ ,  $\langle 110 \rangle$ , and  $\langle 111 \rangle$  dislocations in NiAl. Each dislocation studied exhibits an extended core, which is expected to be difficult to move. In fact, none of the dislocations moved in the simulations with applied stresses as high as  $3 \times 10^{-2}$  G. Although this is the proper order of magnitude for the critical resolved shear stress for  $\langle 111 \rangle$  glide at RT (17),  $\langle 100 \rangle$  dislocations typically become mobile at much lower stresses (12, 20, 27). The sessile dislocation cores may transform to a more mobile configuration under the influence of an applied stress or thermal activation, and the  $\langle 100 \rangle$  and  $\langle 110 \rangle$  dislocations are expected to transform more easily than the  $\langle 111 \rangle$  dislocations.  $\langle 111 \rangle$  dislocations are preferred over  $\langle 110 \rangle$  dislocations below 300°C (10, 15), yet  $\langle 110 \rangle$  dislocations are more frequently observed above this temperature (24, 25, 26, 28). The thermally-activated  $\langle 110 \rangle$  core transformation may therefore be responsible for this transition from  $\langle 111 \rangle$  slip below 300°C to  $\langle 110 \rangle$  slip above this temperature. The simulations do not predict a dissociation of the  $\langle 110 \rangle$  dislocation cores to a separation that can be detected in TEM, and this is consistent with experimental observations of  $\langle 110 \rangle$  dislocations in weak beam microscopy (26).

## ACKNOWLEDGMENTS

This work was supported in part by the Office of Naval Research, Division of Materials Sciences. Partial support was also provided by the National Science Foundation, Division of International Programs and CONICET, through a collaborative research grant. We gratefully acknowledge A.F. Voter for the use of the interatomic potentials.

## REFERENCES

1. V. Vitek, *Crystal Lattice Defects*, **5**, 1 (1974). *A41(4)*, 541, (1980).
2. V. Paidar, D.P. Pope and V. Vitek, *Acta Metall.* **32(3)**, 435, (1984).
3. W. A. Rachinger and A. H. Cottrell, *Acta Metall.* **4**, 109 (1956).
4. Y. Umakoshi, M. Yamaguchi, *Acta Metall.* **24**, 89, (1976) and *Scripta Metall.* **11**, 211, (1977).
5. R. C. Crawford, *Phil. Mag.*, **35**, 567 (1977).
6. M. G. Mendirata, H. M. Kim, H. A. Lipsitt, *Metall. Trans.* **A(15)**, 395, (1984).
7. Y. Umakoshi and M. Yamaguchi, *Phil. Mag.*, **A44**, 711 (1981).
8. W. L. Bragg and E. J. Williams, *Proc. Roy. Soc.*, **A151**, 540 (1935).
9. P. A. Flinn, *Trans. AIME*, **218**, 145 (1960).
10. R. Darolia, R. Field and D. Lahrman, *Alloy Modelling and Experimental Correlation for ductility Enhancement in Near Stoichiometric Single Crystal Nickel Aluminide*, Annual Report, AFOSR Contract F49620-88-C-0052, (1989).
11. M. H. Loretto and R. J. Wasilewski, *Phil. Mag.* **23**, 1311 (1971).
12. A. Ball, R.E. Smallman, *Acta Met.* **14**, 1517 (1966).
13. A. F. Voter, S. P. Chen, *MRS Symp. Proc.* **82**, 175, (1987).
14. R. Pasianot, D. Farkas, *MRS Symp. Proc.*, San Francisco, 1990.
15. R. Pasianot, D. Farkas, E.J. Savino, *Scripta Met. et Mater.* **24**, 1669 (1990).
16. P. R. Munroe, I. Baker, *Scripta Metall.* **23**, 495, (1989).
17. R. Bowman, R. Noebe and R. Darolia, *NASA Conference Pub.* 10039, 47-1 (1989).
18. R. T. Pascoe and C. W. A. Newey, *Metal Sci. J.*, **2**, 138 (1968).
19. D. I. Potter, *Mater. Sci. Eng.*, **5**, 201 (1969/1970).
20. N. J. Wasilewski, S. R. Butler and J. E. Hanlon, *Trans. AIME*, **239**, 1357 (1967).
21. R. D. Field, *These proceedings* (1990).
22. N. J. Zaluzec and H. L. Fraser, *Scripta Metall.*, **8**, 1049 (1974).
23. I. Baker and E. M. Schulson, *Metall. Trans.*, **15A**, 1129 (1984).
24. C.H. Lloyd, M.H. Loretto, *Phys. Stat. Sol.* **39**, 163 (1970).
25. A. Lasalmonie, *Journ. Mat. Scie.* **17**, 2419 (1982).
26. D. B. Miracle, Ph.D. Thesis, Ohio State University, 1990.
27. R.T. Pascoe, C.A.N. Newey, *Phys. Stat. Sol.* **29**, 357 (1968).
28. J. Bevk, R.A. Dodd, P.R.S. Strutt, *Metall. Trans.* **14**, 159 (1973).

Fig. 1:  $\langle 100 \rangle (001)$  slip system

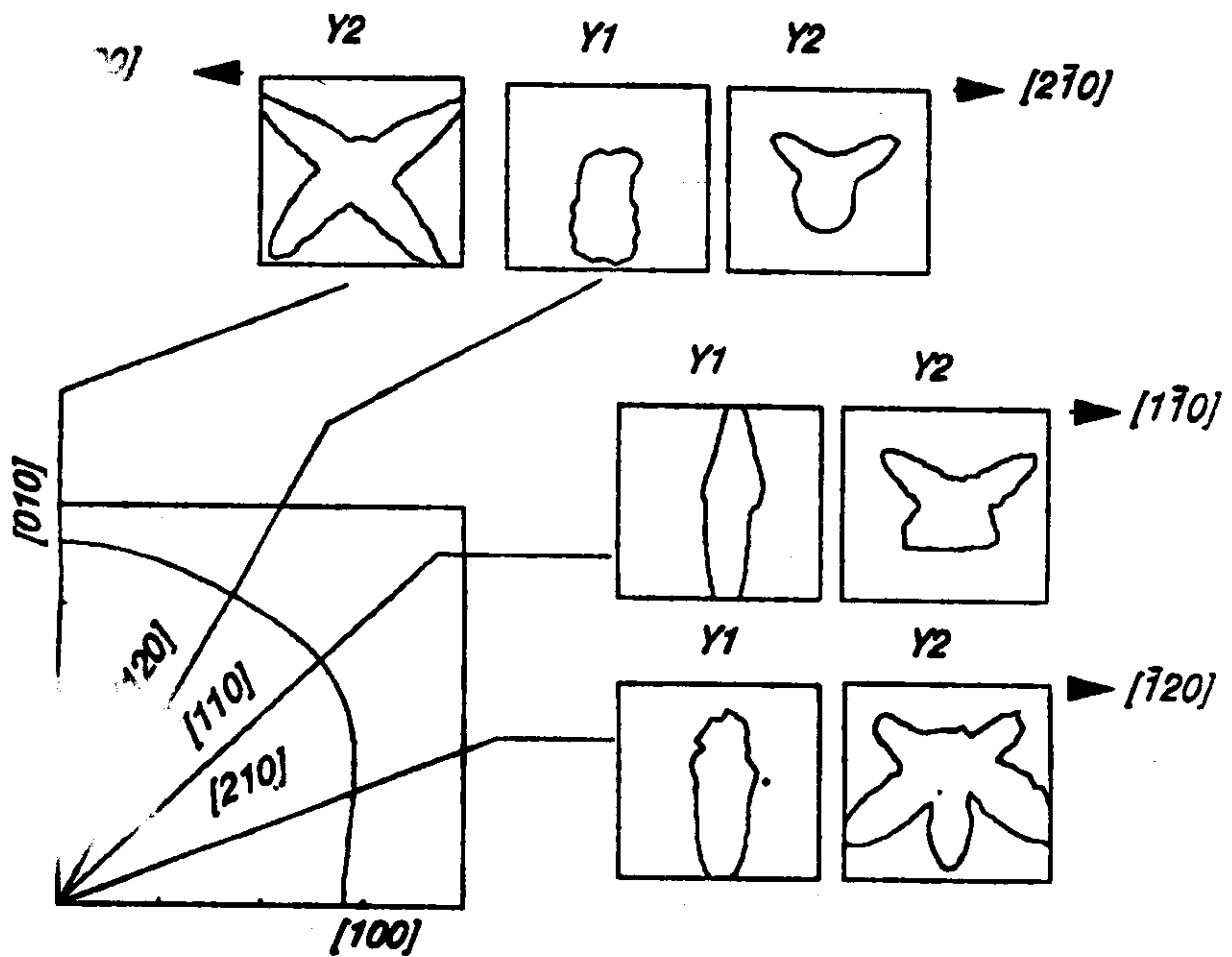


Fig. 2:  $\langle 100 \rangle (01\bar{1})$  slip system

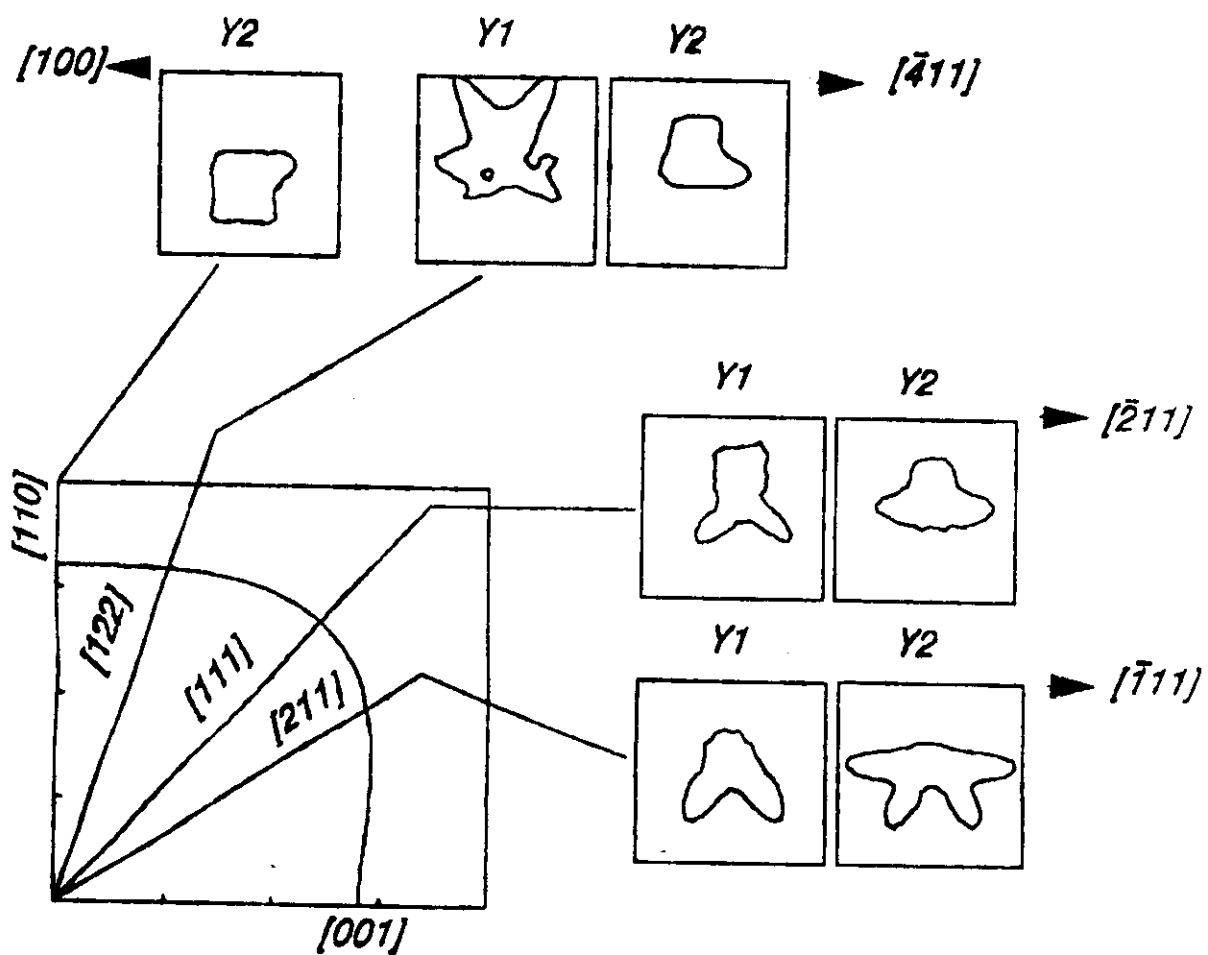
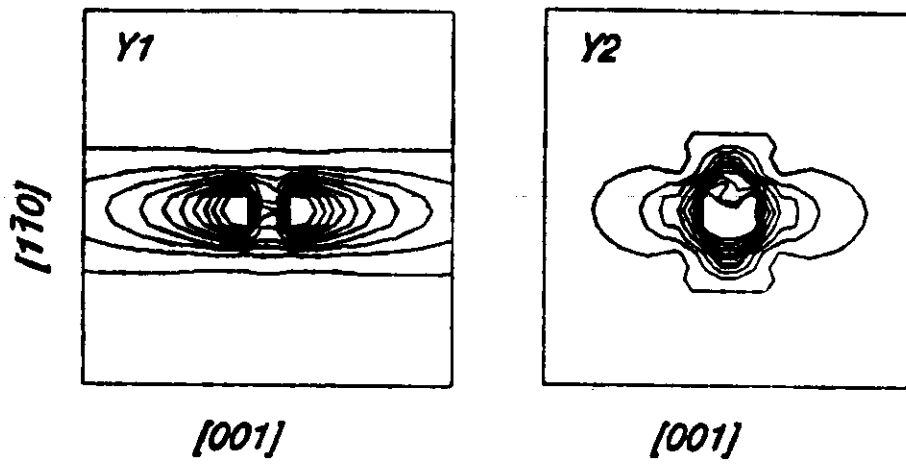
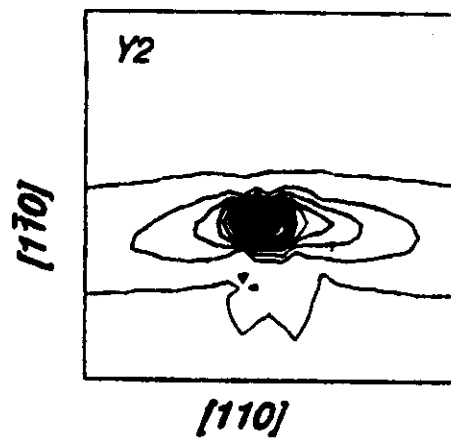


Fig. 3 :  $\langle 110 \rangle$   $(1\bar{1}0)$  slip system

(a) *Screw*



(b) *Edge*



# **DISLOCATION CORE STRUCTURE IN ORDERED INTERMETALLIC ALLOYS**

**R. Pasianot, Diana Farkas and E.J. Savino**

**Department of Materials Engineering,  
Virginia Polytechnic Institute  
Blacksburg, VA 24061**

## **Abstract**

Basic features of dislocation core structures in ordered intermetallic alloys are revealed by atomistic computer simulation. The simulated dislocation core for the most commonly observed slip systems in both  $L1_2$  and B2 alloys. The simulations were carried out with embedded atom interatomic potentials. Screw and edge dislocations were studied, particularly investigating the planarity of the dislocation cores. The general trend of the results agrees with the results of previous investigators using pair potentials for model alloys. In all cases the core structure is spread in one or possibly more closed packed planes.



## ***1. Introduction***

The atomistic structure of dislocation cores is known to have important implications in the mechanical behavior of materials. This was first recognized for BCC lattices by Vitek (1). The significance of this work was that the mechanical behavior of BCC metals could be explained using the results of the core structure simulation. The simulations indicated that screw dislocations were characterized by a nonplanar core, with the corresponding low mobility. The edge dislocations, on the contrary were planar and therefore glissile. The screw dislocations would control the plastic behavior in this case. As higher stresses are applied the structure of these dislocations undergoes a transformation to a glissile structure. Although the core structure calculations are for zero temperature it can be assumed that the effect of temperature may be to allow transitions among the possible core structures. These transitions may occur from the lowest energy configuration (global minimum) to a slightly higher energy configuration that corresponds to a local minimum energy in the calculations. The possibility of these transformations is particularly important if the global minimum configuration is sessile and the transformation occurs to a glissile core at some critical stress. The activated state for this type of transformation may correspond to the configuration found as the dislocation is subject to the critical stress. In this way the core structure simulations can help modeling mechanical behavior changes with temperature. A similar type of study was later used in models for the anomalous yield behavior of  $L1_2$  compounds (2,3). This work was originally initiated with pair potentials for model alloys with the  $L1_2$  structure. These potentials were not intended to represent any particular material, but rather a model alloy. Calculations of dislocation core structure using embedded atom potentials have been carried out recently for the case of a  $[110]$  screw dislocation dissociated in the  $\{111\}$  or  $\{100\}$  planes in  $L1_2$   $Ni_3Al$  (4,5). They indicate that the structure of the dislocation dissociated in the  $\{100\}$  planes is always nonplanar (away from  $\{100\}$  plane), whereas there are several possible configurations for the dislocation dissociated in the

{111} plane. One of these is planar and the others nonplanar. Elastic calculations show that in some of these cases there will be a torque force between the partials (6).

For the case of the B2 structure some simulations have been done with pair potentials (7). We have carried out calculations for the NiAl B2 phase using embedded atom potentials (8). The pair potential work was done for model alloys with relatively low APB energy, and for a screw [111] dislocation dissociated in two  $1/2[111]$  dislocations separated by an APB. The configurations obtained for this case were similar to those obtained for the  $1/2[111]$  dislocation in BCC metals. Experimental studies in NiAl show that the [111] dislocation does not separate into partials (9) and that there is [100] slip (10).

In the present work we would like to give a general overview of the results for the  $L1_2$  and B2 structures. We present the results of a detailed analysis of possible dislocation core structures in  $Ni_3Al$  and NiAl.

In section 2, we describe a procedure based on the elasticity theory, that can be applied to the study of dislocation reactions. The results of this model are presented in section 3. Section 4 deals with the atomistic simulations of the core configurations, and in section 5 these results are compared with those of the elastic model.

## ***2. Elastic Model***

A code which uses a numerical technique to calculate the equilibrium configuration of a number of parallel straight interacting dislocations of arbitrary Burgers vector was developed. Anisotropic elasticity is used in the form proposed by Stroh (11).

In this framework, the interaction energy of two parallel straight dislocations of Burgers vectors  $\bar{b}_1$  and  $\bar{b}_2$  is given by (disregarding constant terms and core effects):

$$E_{inter}^{1,2} = -\frac{1}{\pi} \text{Im}\left\{ \sum_{\alpha=1}^3 \langle \bar{b}_1 | \bar{L}_\alpha \otimes \bar{L}_\alpha | \bar{b}_2 \rangle \ln\left(\frac{1}{Z_\alpha}\right) \right\} \quad (1)$$

where  $\text{Im}\{\}$  is the imaginary part of a complex number,  $\langle \bar{x} | \bar{y} \rangle$  stands for the scalar product of two vectors,  $\bar{L}_\alpha$  are invariant vectors depending only on the orientation of the dislocation lines as defined in reference (11),  $\bar{x} \otimes \bar{y}$  is the diadic (tensorial) product of two vectors,  $Z_\alpha = x_1 + p_\alpha x_2$  is a complex number depending on the dislocation positions (see Fig.1) and  $p_\alpha$  are the roots of the sextic equation with  $\text{Im}(p_\alpha) > 0$ .

The energy of a given dislocation system is simply the addition of terms like eq.1 for each pair considered, and the energy of the faults bounded by the dislocation lines.

In this sense, the above energy depends on the dislocation positions (through the complex numbers  $Z_\alpha$  and the extension of the faults), or equivalently, on a set of coordinates  $\{q_i\}$  that define the degrees of freedom allowed:

$$E_{Tot}(q_1, q_2, \dots, q_n) = \sum_k E_k(\text{fault}) + \sum_{i>j} E_{inter}^{ij} \quad (2)$$

This function is given as input to a standard optimization routine that, through a numerical technique, determines the set  $\{q_i\}$  for which  $E_{Tot}$  is minimum.

Dislocation self energy need not be considered for equilibrium force purposes because it amounts to add a constant term to equation 2, then the set  $\{q_i\}$  so determined is the equilibrium configuration. The method can therefore give the equilibrium position of the partial dislocations for a given splitting reaction. In some cases the absence of a minimum indicated the fact that the particular splitting was not possible. In some other cases a minimum may be found, although it is local minimum and a different dissociation is favored.

Note that energy comparisons for different types of splitting are not simply achieved by adding the self energy for each partial. This is due to inconsistencies in the expressions for the interaction energy. The energies of two calculations of this kind can be unambiguously compared if they deal with exactly the same partial dislocations and if the orientation of the reference coordinate system used is the same in terms of the crystal directions. Therefore, energies were only compared when the dissociation involved identical or equivalent partial dislocations. This is discussed in detail by Steeds (12).

Also note that, in order to compare with simulation results, the elastic constants and fault energies used in this code are the ones predicted by the interatomic potential used in the computer simulation work.

## ***Results from the Elastic Calculations***

### **< 110 > Dislocations in Ni<sub>3</sub>Al**

Several configurations of this dislocation were tested, which may be relevant for the modeling of mechanical behavior. These involve APB and CSF faults. The energies of these faults as predicted by the interatomic potential (13) are given in Table 1, whereas the elastic constants are shown in Table 2. These dissociations occur mainly in planes of the {111} or {100} family.

#### ***Dissociation in the {111} planes.***

For model purposes, two partials of the type  $1/2[1\bar{1}0]$  were assumed to bound an APB in the (111) plane. Furthermore, each partial was dissociated in Shockleys with a complex stacking fault ( CSF ) in either (111) or  $(11\bar{1})$  planes.

There are three contributions to the energy of the system, namely, the APB energy the CSF energy and the elastic interaction energy between pairs of dislocations. Fig.2 shows, in a schematic way, the degrees of freedom allowed to the whole structure, i.e., X, Y, Z and W. These are as follows, W and X : the CSF region width for core spreading on the (111) plane and on the  $(1\bar{1}\bar{1})$  plane respectively , Y : the distance measured on the  $(1\bar{1}\bar{1})$  plane between the superpartial center and the APB plane, and Z : the APB width.

The energy was then numerically minimized as described above with respect to these parameters, and the results are collected in Table 3. Y is not reported in that table because it either results  $Y = 0$  for the planar superpartials or  $Y = X/2$  for the nonplanar case. The last column of the table gives the energy of the different structures -depicted in the insets- relative to the planar core.

The elastic calculations show that the global minimum corresponds to the planar core. This was first pointed out by Yamaguchi et al. (2). The nonplanar core, with the partials dissociated in the  $\{111\}$  plane complementary to the APB and located at the same height with respect to the APB ,was not found to be a minimum. Yoo (6) carried out elastic calculations for the interaction of two  $1/2 \langle 110 \rangle$  partials bounding an APB in the  $\{111\}$  plane and found that it implies a torque that would tend to bend the APB. The present calculations suggest that this torque may be relieved by introducing an APB in a zig-zag shape, as indicated in Fig.2. The model predicts an energy difference between the planar core and the lowest energy nonplanar core (in zig-zag shape) of 0.9 eV/nm. Table 3 also shows the equilibrium separation between the superpartials as well as that between the Shockleys. The elastic predictions are that the minimum energy separation for the planar core is somewhat higher than that for the nonplanar core. It is also seen that the distance among the Schockley partials is about 1-2 nm. This is expected to be the order of magnitude of the spread of the core for each superpartial. However this is a small distance, for which elastic assumptions could loose validity.

### *Dissociation in the {100} plane.*

Similar calculations were carried out for dissociations in the cubic plane that involve the same type of dislocations discussed before. The results are collected in Table 4, where X and Z have the same meaning as before. Note that there are a number of other configurations that are necessarily equivalent to one of the ones shown in Table 4. All these configurations are nonplanar, and therefore are expected to be sessile. Table 4 also gives the energies of the various configurations relative to the {111} planar core. The first point is that the values are lower than those obtained for dissociation in the  $\{111\}$  plane, so that dissociation in the cubic plane will be favored. This is consistent with most models for the anomalous yield behavior of the material.

The differences in energy among the structures shown are very small, both being sessile. These configurations may be relevant for the modeling of the mechanism of transformation of the sessile structures into the glissile planar core dissociated in the {111} plane.

It is of interest to note that closely related structures have been observed experimentally using the HREM technique (14).

### *Mixed $\langle 110 \rangle$ Dislocations in $\text{Ni}_3\text{Al}$*

Several edge and mixed dislocations were considered dissociated in the {111} plane. A dislocation with mixed character with dislocation line along a  $\langle 110 \rangle$  direction  $60^\circ$  from the burgers vector was considered. The separations between the partials increase as the edge character increases (as in the case for an isotropic material in virtue of the  $\frac{1}{1-\nu}$  factor that modifies the expressions for edge dislocations). We obtained a value of about 10 nm for the pure edge and 8.1 nm for the  $60^\circ$  case. In all cases the core structure was assumed to be contained in the {111} plane of the dissociation. We also studied the

$[1\bar{1}0]$  edge dislocation dissociated in the  $(001)$  plane. The distance between the partials in this case was found to be 16.6 nm. Further dissociation of the superpartials was not attempted.

### **< 111 > Screw Dislocations in B2 NiAl**

We performed elastic calculations for the splitting of this dislocation into two partials of the type  $1/2 < 111 >$  bounding an APB. The APB was located in either the  $\{110\}$  or  $\{112\}$  planes. The energies of these faults, as given by the interatomic potential, are shown in Table 5. For the dissociation in the  $\{110\}$  plane a distance between superpartials of 2nm was found; instead, for the  $\{112\}$  plane the corresponding value was 1.7nm. The configuration with the APB in the  $\{110\}$  plane has an energy which is 0.6 eV/nm lower, as expected from the lower fault energy. These separations are very close to the resolution limit of weak beam electron microscopy techniques. Also, for these small spacings the validity of elasticity calculations starts being doubtful.

## ***4. Atomistic Computer Simulation***

### **Interatomic Potentials and Simulation Method**

We performed atomistic simulations of the dislocation core area using embedded atom interatomic potentials. These potentials were developed by Voter and co-workers based on the  $\text{Ni}_3\text{Al}$  phase (13). Table 1 gives the fault energies predicted for this structure and Table 2 gives the elastic constants.

The values of the APB are in reasonable agreement with experiment. However, the complex stacking fault is somewhat lower in energy than the APB and although no experimental data are available this is probably unrealistic. One would expect that since in a CSF both, spatial structure and chemical order are distorted, the fault energy should

be higher than that of an APB, where only chemical order is perturbed. This probably means that the CSF energy predicted by the potential is too low. Otherwise these potentials seem to be a very good description of  $\text{Ni}_3\text{Al}$ .

For the NiAl phase only the lattice parameter and cohesive energy were considered in the development of these potentials. Our calculations have shown that the B2 phase is indeed stable with respect to the  $L1_0$ . The difference in cohesive energies of these two phases is very small (4.369 for the  $L1_0$  phase eV/atom compared to 4.375 eV/atom for the B2 structure). This is very reasonable since it is known that off-stoichiometry NiAl undergoes a martensitic transformation to the  $L1_0$  phase. The extrapolation of the  $M_s$  temperature to the stoichiometric composition gives a temperature only slightly below zero (15). As we mentioned earlier, Table 5 gives the fault energies calculated with these potentials.

$\Gamma$  surface calculations (1) were carried out to insure that no other stable faults were present, other than the APBs. Experimental measurements are available for the energy of the APBs based only on the edge dislocation separation (16) since the screw  $\langle 111 \rangle$  dislocation does not split into partials (9). The edge  $\langle 111 \rangle \{01\bar{1}\}$  is expected to dissociate into  $\langle 100 \rangle + \langle 011 \rangle$  according to elastic calculations, and there is some doubt about the validity of the fault energies reported based on the dissociation into two  $1/2 \langle 111 \rangle \{01\bar{1}\}$  edge dislocations. Calculated values for the APB in the  $\{110\}$  plane range from about 250 to 880 mJ/m<sup>2</sup> (17). The high value of 880 mJ/m<sup>2</sup> was computed from quantum mechanical calculations using a supercell approach (17). We reproduced the same supercell and computed the energy of the APB based on this supercell and atomistic energy minimization with periodic boundary conditions. The value obtained was 540 mJ/m<sup>2</sup> as opposed to the 340 obtained for the same interatomic potential but fixed boundary conditions in the direction perpendicular to the APB plane. We conclude that the former calculation is affected by quite strong interactions between the parallel APBs considered in the supercell.



The values of the elastic constants predicted by these potentials are given in Table 6 together with the experimental ones (18).

The atomistic simulations for the dislocations considered were carried out in the usual way using fixed boundary conditions in the directions perpendicular to the dislocation line, by holding the atoms at the positions given by anisotropic elasticity (Volterra solution), whereas periodicity is assumed along the dislocation line ( $z$  axis). Different orientations of the simulation region were used so that the major fault of the system was always oriented perpendicular to the  $y$  axis, coincident with the  $(x,z)$  plane. The computational codes are based on DEVIL (19) modified to be used with volume dependent potentials. They were also adapted so that the fault could be given a zig-zag shape (though mainly contained on the  $(x,z)$  plane). This point is important since some of our elasticity results suggested zig-zag shapes as minimum energy configurations. The procedure involves choosing a proper zig-zag shape for the branch cut of the logarithmic term of the displacement field so as to match the fault shape.

It is important to note that the anisotropic elastic solution plays two roles in these simulations. One is to fix the boundary conditions far away from the dislocation core. The other is to serve as the starting configuration for the minimization process. It is well known that different local minima can be attained in atomistic simulations depending on the initial configuration (2). Therefore several initial positions of the elastic center of the dislocation should be tried, so to insure that the global minimum configuration is found. In the present work we varied our initial configuration by varying the elastic center of the dislocation and also by trying various splitting possibilities with very small distances among the dislocations.

## Graphical Representation of Dislocation Core Structures

It has been customary to represent the dislocation core structures by means of arrows related to displacements of atoms in a given direction. In the method used by Yamaguchi et al. (2), the arrows represent relative displacements of one atom with respect to another, generally a first neighbor. The direction of the arrow simply indicates the two atoms considered and the magnitude is proportional to the magnitude of the relative displacement between the two atoms modulus  $b/2$ , being "b" the Burgers vector.

1. use a related scheme (5).

Here a different way of depicting the core structures based directly on the strain tensor  $\bar{\bar{E}}$ . We plot the quantity  $Y_1 = 2(E_{xx}^2 + E_{yy}^2)$  and  $Y_2 = E_{xx}^2 + E_{yy}^2 + 2E_{xy}^2$ . Both quantities are invariant under rotations about the dislocation line (the z axis). When the plane perpendicular to the dislocation line is a mirror plane the first quantity is related only to the screw components and the second one to the edge components. This is so because for this case edge and screw components have no interaction with each other and may be treated separately. Once  $\bar{\bar{E}}$  is obtained through a finite difference scheme on the displacement field,  $Y_1$  and  $Y_2$  can be plotted as functions of (x,y) using standard three dimensional graphics. In particular the contour plots of this surface will directly give the shape of the dislocation core, extended to different levels of deformation.

The plot can be done using various choices of the burgers vector to study the possible internal structure of the dislocation core. Using the appropriate burgers vectors corresponding to the splitting considered, the method proposed here can give the position of the partial dislocations accurately. In the following sections we will use this scheme as well as that developed by Yamaguchi et al. (2).

## Simulation Results for Ni<sub>3</sub>Al

The results of the computer simulations for the dislocations in Ni<sub>3</sub>Al are generally in agreement with elasticity theory.

### *Dissociation in the {111} planes.*

For the dissociation of the  $\langle 110 \rangle$  screw dislocation in the {111} plane three basic cores were studied that were found feasible in the elastic model. These are the planar, nonplanar and mixed core. The nonplanar core was confirmed to have the zig-zag shape that was predicted by elasticity. The energy of the simulation block was monitored as a function of the separation between partials in order to find the minimum. The partials do not find their minimum energy spacing as part of the energy minimization process unless the simulation block is very large. This is probably due to the effect of the fixed boundary conditions which are obtained from the elastic solution with the partials at the initially given location. The calculation of the total energy is done as the sum of the energy of the simulation block and the elastic energy of the region outside the block up to a square of  $0.2\mu$ , taken as a continuum. Fig.3 shows the obtained results for the three basic cores, where the energy of the system is given as a function of the superpartials separation. It is seen that the elastic prediction of the planar core as the lowest energy is confirmed, though the difference in energy between nonplanar and planar cores is one third of that predicted by elasticity.

Another important point is that the energy of the nonplanar core in zig-zag shape is quite lower than that of the nonplanar calculated in our previous work (4) and also found in the work of Yoo et al. (5). For a  $1/2 \langle 110 \rangle$  screw superpartial to stand a tangential force (6) from the other superpartial, a core structure must be assumed that has a Peierls stress high enough to prevent motion along the direction of the force (see

Fig.4). The stress on each partial can easily be estimated from the expression of the tangential force between the two:

$$f_{\theta} = \frac{b^2}{2\pi r} \sqrt{c_{44} \frac{(c_{11} - c_{12})}{2}} \frac{(A - 1)tg\theta}{(Atg^2\theta + 1)} \quad (3)$$

where  $A = 2c_{44}/(c_{11} - c_{12})$ .

Writing  $f_{\theta} = \tau b$  where  $\tau$  is the shear stress, and substituting for the values of the elastic constants taken from Table 2 and  $tg\theta = \sqrt{2}$ ,  $b \approx 0.25nm$ ,  $r \approx 6nm$ , we get  $\tau = 190$  MPa.

high stress may be supported by the planar core found in the simulations because it is fully applied perpendicular to the slip plane (111). This is not the case for the nonplanar core with the partials spread on the  $(11\bar{1})$  plane. The resolved shear stress on the slip plane for this core is still high,  $\tau_{ss} = \tau \times 2 \frac{\sqrt{2}}{3} \approx 0.94\tau$  causing slip in the  $(11\bar{1})$  plane that reliefs most of the torque and creates a fault in zig-zag shape. Fig.5 shows the relaxed structure of the nonplanar core configuration. In this figure, the zig-zag shape is barely noticed due to the small deviation of the position of the partials from the APB plane. In order to obtain this structure it was necessary to use a starting configuration with the APB created in a zig-zag shape. We also studied the internal structure of the relaxed core for each superpartial. This is seen in Fig.6 where the new scheme described above is used. The figure corresponds to the screw and edge components for the left partial of the nonplanar core. Both components show a two peak structure corresponding to the two Shockley partials. The distance between the Shockley partials is larger in the screw components than in the edge components (these overlap). The overall value is in good agreement with elastic predictions. The separation of the two main partials is also in good agreement with elasticity, being shorter for the nonplanar core.

### *Dissociation in the $\{100\}$ plane.*

The results for the dissociation in the cubic plane are also similar to the predictions of elasticity. Fig. 7 shows one core structure obtained from the simulations in which the  $1/2\langle 110 \rangle$  partial is spread in only one  $\{111\}$  plane. Another core structure much higher in energy was also found corresponding to the  $1/2\langle 110 \rangle$  screw partial being spread on both  $\{111\}$  planes containing the dislocation line. Its high energy value suggests that it will not occur, unless stabilized by some other process. However, it may be relevant to the transformation of the sessile equilibrium structure into a glissile one under high stress or temperature.

In a recent work using in situ TEM, dislocations of this type were observed to move by a locking- unlocking mechanism in the cubic plane (20). This observation suggests the existence of a higher energy configuration core spread in the cube plane. We therefore searched for other high energy local minima that may be relevant to the deformation process at high temperatures, particularly configurations spread in the cube plane. A number of possible initial configurations were tested, that may lead to such a local minimum in the energy-configuration hypersurface. In all cases the structure was observed to change to a core spread in the  $(111)$ ,  $(11\bar{1})$  or both planes. In particular, we tested an initial configuration that consisted of a core actually spread in the  $(001)$  plane (Fig 8), that was constructed to be near the expected structure of a glissile core on  $(001)$ . The structure immediately relaxed and spread on a close packed plane. A similar result was obtained under application of a resolved shear stress of about  $0.04\mu$  (shear modulus): the core transformed to the  $(11\bar{1})$  plane and subsequently moved on the same plane.

The core structures observed are also essentially the same than those found for the dissociation in the  $\{111\}$  planes except that the two cores in the  $(111)$  and  $(11\bar{1})$  planes

are now completely equivalent. We conclude that the position of the APB does not significantly affect core shapes.

### ***Edge and mixed $\langle 110 \rangle$ Dislocations in $\text{Ni}_3\text{Al}$***

A planar structure was found for the edge dislocation dissociated in the  $\{111\}$  plane, although a complete study of the effect of the location of the elastic center was not performed. Similar results were obtained for the mixed dislocation with a  $60^\circ$  angle between the burgers vector and the dislocation line, as described in section 3. A nonplanar core structure was obtained for the edge dislocation dissociated in the cube plane. The internal structure of this nonplanar core is shown in Fig.9. It presents some spreading in the cubic plane as well as in both  $\{111\}$  planes containing the dislocation line. The

was found for several different positions of the elastic center of the dislo-

### **Simulation Results in B2 $\text{NiAl}$**

There are two main burgers vectors to be considered  $\langle 111 \rangle$  and  $\langle 100 \rangle$  (21). The  $\langle 111 \rangle$  screw dislocation can possibly dissociate and the elastic calculations suggested that it does. The edge  $\langle 111 \rangle$  is unstable against the dissociation into  $\langle 100 \rangle + \langle 011 \rangle$ . The  $\langle 100 \rangle$  dislocations cannot dissociate and therefore no elastic calculations were performed. Fig. 10 shows the line stability diagrams (Wulff plots) for  $[100]$  burgers vector and two different slip planes. The experimental elastic constants of Table 6 were used. In these diagrams the regions of concave curvature represent unstable orientations, therefore, no screw or edge orientation is expected for  $(011)$  slip. For  $(001)$  slip the screw orientation is unstable but not the edge one.

### ***<111> Screw Dislocations***

The first analysis performed was the energy calculation as a function of the distance between the  $1/2$   $\langle 111 \rangle$  screw partials on both planes  $\{110\}$  and  $\{112\}$ . It was found that the total energy decreased as the dislocations became closer and closer. It was concluded that the elastic predictions were not maintained in this case. It should be noted that the energy calculation included the elastic contribution of the region outside the simulation block. There are two possible interpretations of the discrepancy of the elastic results and the simulation results. The first is that the minimum energy separations obtained from elasticity are simply outside the range of validity of elasticity theory. Another interpretation is that there is actually a local minimum for the dissociated case but that the undissociated configuration is the global minimum and the relaxation process reaches this global minimum. The latter interpretation seems to be supported by the shape of the energy versus separation curve obtained for dissociation in the  $\{110\}$  plane shown in Fig.11, where a shallow local minimum appears to be located at about 2 nm, as predicted by elasticity. Similar results were obtained for the partials dissociated in the  $\{112\}$  plane. In all cases the energy decreased sharply as the partials were closer than 1 nm.

The undissociated dislocation has an internal structure that is quite complex, as shown in Fig.12. Several different internal structures for this dislocation core were obtained besides the ones shown in Fig.12. In all cases the core region is spread over no more than a few nm, this is consistent with recent weak beam electron microscopy results that show that the  $\langle 111 \rangle$  dislocations in NiAl are not dissociated (9).

### ***<100> Dislocations***

Pure screw orientations in this case are elastically unstable. The edge  $\langle 100 \rangle$  dislocation with the dislocation line along a  $\langle 010 \rangle$  direction was found to have two con-

figurations, as illustrated in Fig.13. Note that the local stoichiometry of these two configurations is different. The configuration in a) was lower energy. The distortion of the core is spread in compact planes of the type  $\{110\}$ , as shown in Fig. 13c.

We computed two different mixed orientations for the  $[100]$  dislocation suggested by the plots of Fig. 10. The first is with the dislocation line along  $[101]$  and the second along  $[111]$ . In both cases we found core structures that had some nonplanar components. For the first case the screw components are planar and the edge components are nonplanar. However, the screw components are planar along the  $(\bar{1}01)$ , which is not the slip plane. For the second case the edge components were planar along the  $(01\bar{1})$  slip

The latter is more likely to transform to a glissile structure at low levels of stress. of these cores under stress is in progress.

### **Effect of the Interatomic Potential Used**

The core structures reported above for the  $L1_2$  phase are basically the same core structures originally reported by Yamaguchi et al. (2) using pair potentials for model alloys. The results for the B2 structure are different from the ones obtained by Takeuchi (7). This may be because the APB energy used in that work is lower. It seems that in our calculations a local minimum also exists with structure similar to those found in reference (2), except that the separation between the partials is too small and the structure relaxes to the global minimum of the undissociated dislocation. These facts suggest that the same basic structures are predicted by different interatomic potential functions, with different separations between partials and different relative energies.

### ***5.Comparison of Elastic and Simulation Results***

For all the calculations carried out in  $Ni_3Al$  it was observed that the predictions of our elastic model were all confirmed by the atomistic simulation results. The separation



distances calculated were followed very closely for all types of dissociation, with a discrepancy of less than 10%. Note that all the distances between the main superpartials obtained in these cases are around 6 nm. The separations among the Shockley partials however, are smaller (less than 2 nm). Reasonable agreement was nevertheless obtained for these small separations as well. Qualitative trends were also confirmed, for example the fact that the separation of the partials in the (111) plane is lower for the nonplanar configuration than for the planar one. The energy trend predicted by the elastic model was in agreement with the simulation results. The differences in energies among the different core configurations obtained from the simulations were of the same order of magnitude than those predicted by the elastic model, with discrepancies of up to a factor of three. This is of course expected since core effects are not taken into account in the elastic calculations and the energy differences are small.

In the case of the NiAl calculations it also seems that the simulations show a minimum at about the splitting distances calculated elastically. In this case we expected that agreement would be more difficult since the separation distances are smaller (2nm) and core effects should be relatively more important.

## ***6. Discussion and Conclusions***

The present results for the  $L1_2$  structure are in qualitative agreement with those obtained by Yamaguchi et al. using pair potentials for model  $L1_2$  alloys (2). The major difference is that we obtain the planar core as a lower energy than the nonplanar one in the case of dissociation on the (111) plane. In this respect, our results agree with those of Yoo (5). For the nonplanar core split in the (111) plane, the two partials were found to be slightly above and below the APB line forming a core in zig-zag shape for the total dislocation. This has a significant effect on the energy of the core structure. This configuration mostly relieves the torque force. The energetic balance among different core

structures is very delicate. The important fact is that the same basic core structures are obtained despite that more realistic interatomic potentials are used. However this situation may not be general. In (22) it is found that pair potentials do not explain the prismatic slip observed in certain hcp transition metals. For this case a tight binding model, that accounts for d orbital effects, seems more appropriate.

We also note that the location of the APB does not affect core types, because either with the APB located on (111) or on (001) the same two cores were obtained : the core spreads on (111) , or on  $(11\bar{1})$ . Regarding the experimental observations of ref. 20, we were not able to find a core spread on the (001) plane of the APB, as these observations would suggest. For the case of the B2 structure, our results are very different from those obtained with model alloys (7). Possibly, the reason is that the APB is much higher in the materials considered here than in the model alloy potentials of previous works. The

new dislocation therefore does not dissociate into two  $1/2 \langle 111 \rangle$  superpartials. Nevertheless, we believe that the configurations with the two superpartials dissociated in the {110} or {112} planes are local minima with separations that are close to the predictions of elasticity. These separations are small enough so that the simulation converges to the global minimum. Most importantly, these results agree with the experimental observations using weak beam electron microscopy. The present work however, still cannot make an assessment of the question  $\langle 111 \rangle$  versus  $\langle 100 \rangle$  slip. This assessment has to be done in a study of the dislocation core mobility, which is in progress and will be reported elsewhere.

It is interesting to note that all the cores studied in the present work suggest that the equilibrium core structures tend to be mainly localized on close packed planes.

## REFERENCES

1. V. Vitek, *Crystal Lattice Defects*, 5, 1 (1974).
2. M. Yamaguchi, V. Paidar, D. P. Pope, V. Vitek, *Phil. Mag.* A45(5), 867, (1982).
3. V. Paidar, D.P. Pope and V. Vitek, *Acta Metall.* 32(3), 435, (1984).
4. D. Farkas, E. J. Savino, *Scr. Metall.* 22, 557, (1988).
5. M. H. Yoo, M. S. Daw, M. I. Baskes in "Atomistic Simulation of Materials", pag. 401, Ed. by V. Vitek and D.J. Srolovitz Plenum Press, N.Y. (1989).
6. M. H. Yoo, *Scr. Metall.* 20, 915 (1986).
7. S. Takeuchi, *Phil. Mag.* A41(4), 541, (1980).
8. R. Pasianot, D. Farkas and E.J. Savino, to be published.
9. P. R. Munroe, I. Baker, *Scr. Metall.* 23, 495, (1989).
10. A. Ball and R. E. Smallman, *Acta Metall.* 14, 1349, (1966).
11. J. P. Hirth, J. Lothe, "Theory of dislocations", 2nd ed., John Wiley & Sons, (1982).
12. J. W. Steeds, "Introduction to anisotropic elasticity theory of dislocations", Clarendon Press, Oxford, pag.31 (1973).
13. A. F. Voter, S. P. Chen, *MRS Symp. Proc.* 82, 175, (1987).
14. M.A. Crimp, *Phil. Mag. Lett.* 60, 45 (1989).
15. J. L. Smialek and R. F. Hehemann, *Metall. Transactions*, 4, 1571 (1973).
16. R. G. Campany, M. H. Loretto, and R. E. Smallman, *Journal of Microscopy*, 98, 174, (1973).
17. A. J. Freeman and T. Hong, id. ref. 5, pag. 41.
18. A. F. Voter, private communication.
19. M.J. Norgett, R.C. Perrin, and E.J. Savino, *J.Phys. F* 2 L73, (1972).
20. N. Clément, D. Caillard, P. Lours, A. Coujou, *Scr. Metall.* 23, 563, (1989).
21. M. H. Loretto and R. J. Wasilewski, *Phil. Mag.* 23, 1311 (1971).
22. B. Legrand, *Phil. Mag.* A52, 83 (1985).

## Acknowledgments

This work was supported in part by the Office of Naval Research, Division of Materials Sciences and by the U.S. Department of Energy, Energy Conversion and Utilization Technologies program under contract #19x-89678v with Martin Marietta Systems, Inc. and was monitored by Oak Ridge National Laboratory. Partial support was also provided by the National Science Foundation, Division of International Programs and CONICET, through a collaborative research grant. We gratefully acknowledge A.F. Voter for the use of the interatomic potentials. and M. Yoo for helpful discussions.

### Figure Captions

1. Scheme used for the elastic dislocation interaction (Eq. 1)
  2. Schematic drawing of the position of the partial dislocations considered in the elastic model for a  $\langle 110 \rangle$  dislocation dissociated in the  $\{111\}$  plane.
  3. Energy vs. separation curves for three possible core structures of the  $\langle 110 \rangle$  dislocation dissociated in the  $\{111\}$  plane.
  4. Scheme for the calculation of the resolved shear stress (Eq. 3).
  5. Differential displacement map for the core structure of the complete (nonplanar)  $[1\bar{1}0]$  screw dislocation. The APB is indicated and only two atom planes are shown.  $\square$  : Al,  $\Delta$  : Ni.
  6. Strain invariants for a relaxed (nonplanar) superpartial dissociated into Shockley partials, using  $1/6 \langle 112 \rangle$  burgers vector. a)Screw components ( $Y_1$ ) b)Edge components ( $Y_2$ )
  7. Differential displacement map for the screw components of a  $1/2[1\bar{1}0]$  screw dislocation spread in the  $\{111\}$  plane. The APB is on the  $(001)$  plane.  $\square$  : Al,  $\Delta$  : Ni.
  8. Initial configuration tested with a core spread in the  $(001)$  plane. The APB is on the  $(001)$  plane.  $\square$  : Al,  $\Delta$  : Ni. This core relaxed to that of Fig. 7.
  9. Differential displacement map for a core structure of the  $1/2 \langle 110 \rangle$  edge dislocation. The APB is on the  $(001)$  plane.  $\square$  : Al,  $\Delta$  : Ni.
- ability diagrams in NiAl for  $\langle 100 \rangle$  slip, a) on  $\{001\}$  and b) on  $\{011\}$ .
11. Energy vs. separation for the splitting of the  $\langle 111 \rangle$  screw dislocation into two  $1/2 \langle 111 \rangle$  on the  $\{110\}$  plane.
  12. Two possible core structures of the  $\langle 111 \rangle$  screw dislocation in NiAl: Contour lines for  $Y_2$  invariant.
  13. Two core structures of the edge  $[100]$  dislocation in NiAl a) and b) and typical contour plot c).  $\bullet$  : Ni,  $\Delta$  : Al.

Table 1. Fault Energies of Ni<sub>3</sub>Al (mJ/m<sup>2</sup>)

	APB		{111}	
	{111}	{100}	CSF	SISF
EAM	142	83	121	13

Table 2. Elastic constants for Ni<sub>3</sub>Al

	Elastic Constants in GPa	
	EAM	Experimental
$c_{11}$	246	230
$c_{12}$	137	150
$c_{44}$	123	131

Table 3. Elastic Model Results for the  $[\bar{1}\bar{1}0]$  screw dislocation dissociated in the {111} plane.



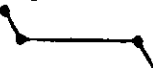

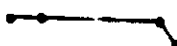
X [nm]	Z [nm]	W [nm]	E [eV/nm]	
—	4.17	1.83	0.0	
1.09	5.43	—	0.9	
0.94	5.69	—	1.0	
0.97	5.02	1.69	0.5	
0.89	5.10	1.69	0.6	

Table 4. Elastic Model Results for the  $[\bar{1}\bar{1}0]$  screw dislocation dissociated in the  $\{001\}$  plane.



X [nm]	Z [nm]	E [eV/nm]	
1.05	9.42	-1.2	
1.06	9.39	-1.2	

Table 5. Fault Energies for NiAl (mJ/m<sup>2</sup>)

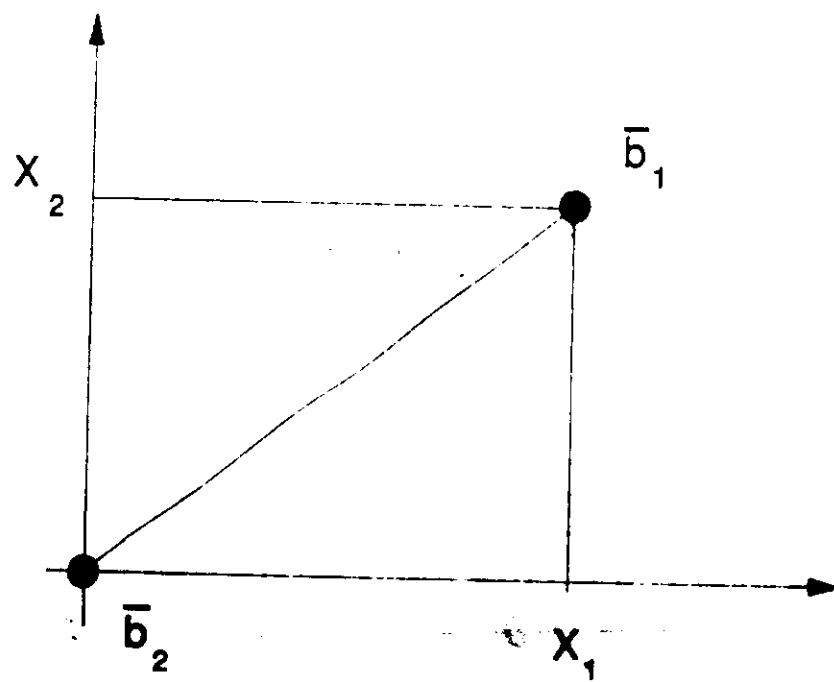
APB	
{110}	{112}
340	410

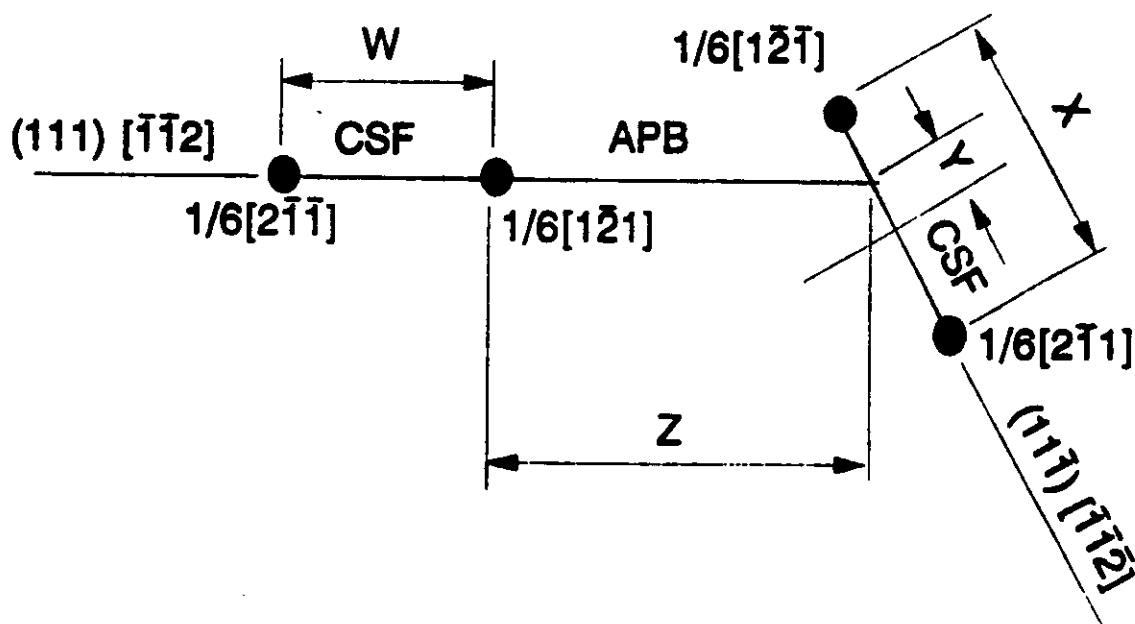
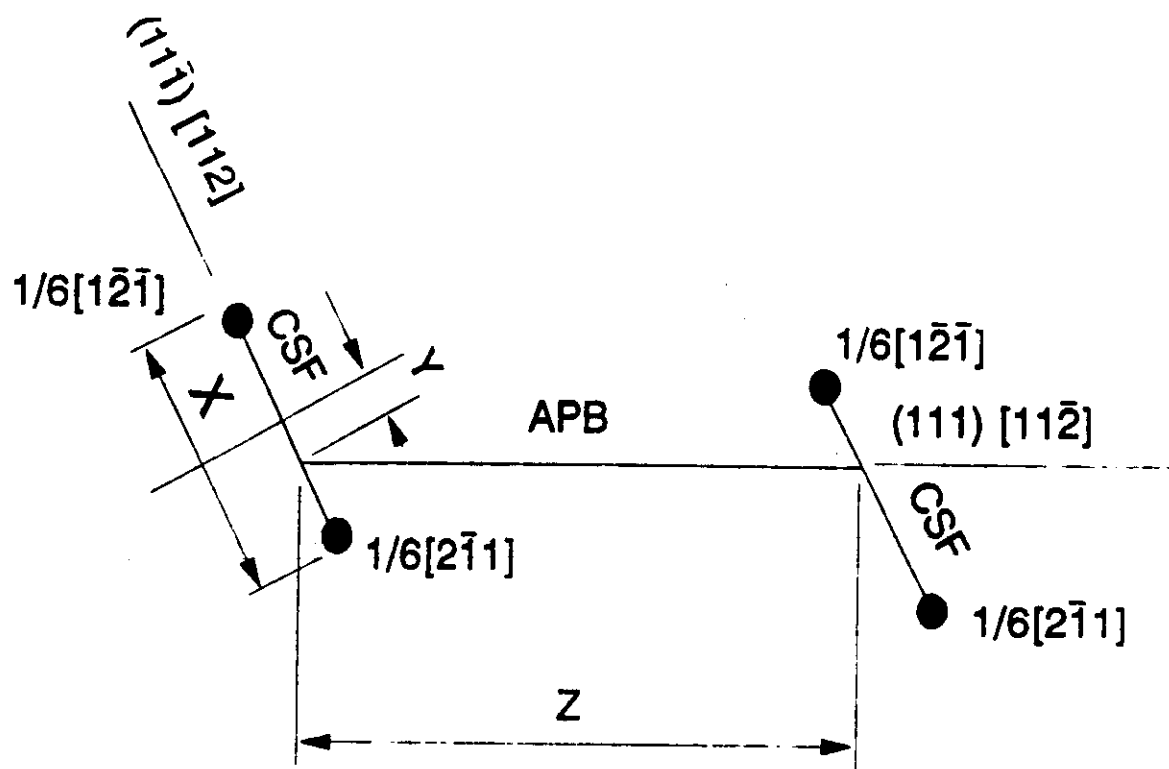
Table 6. Elastic Constants for NiAl

	Elastic Constants in GPa		
	EAM	Experiment (1)	Experiment (2)
$c_{11}$	279	203	204
$c_{12}$	186	134	136
$c_{44}$	178	116	114

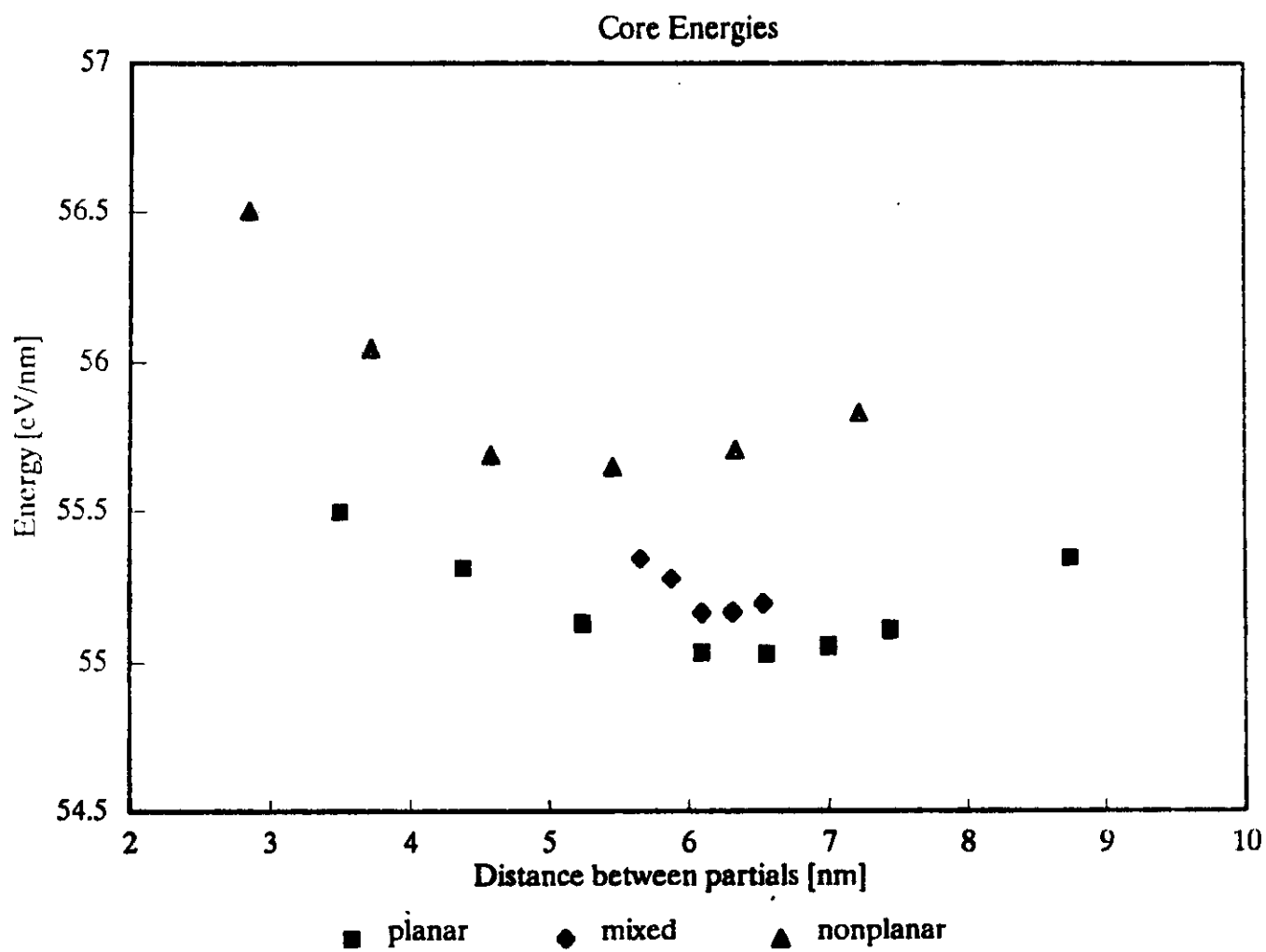
<sup>1</sup> N. Rusovic and E.T Henig, Phys. Stat. Sol. A, 57 (2) 529-540 (1980)

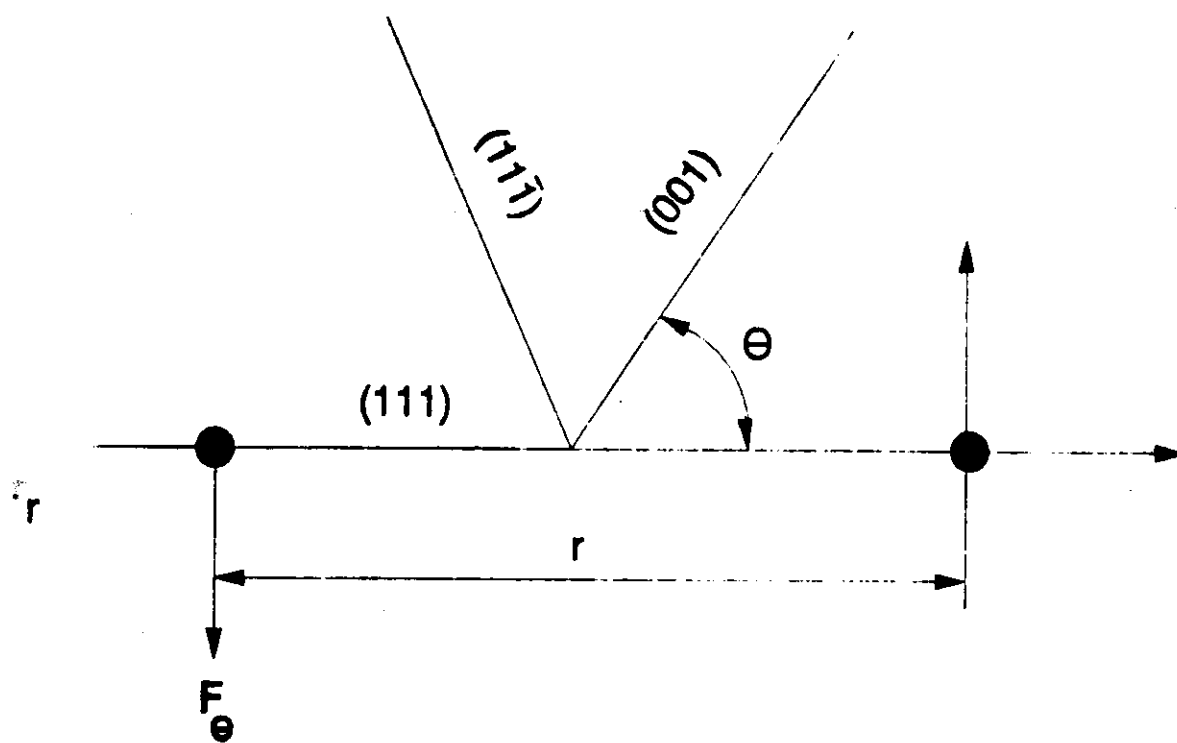
<sup>2</sup> N. Rusovic and H. Warlimont, Phys. Stat. Sol. A., 44, 609 (1977)

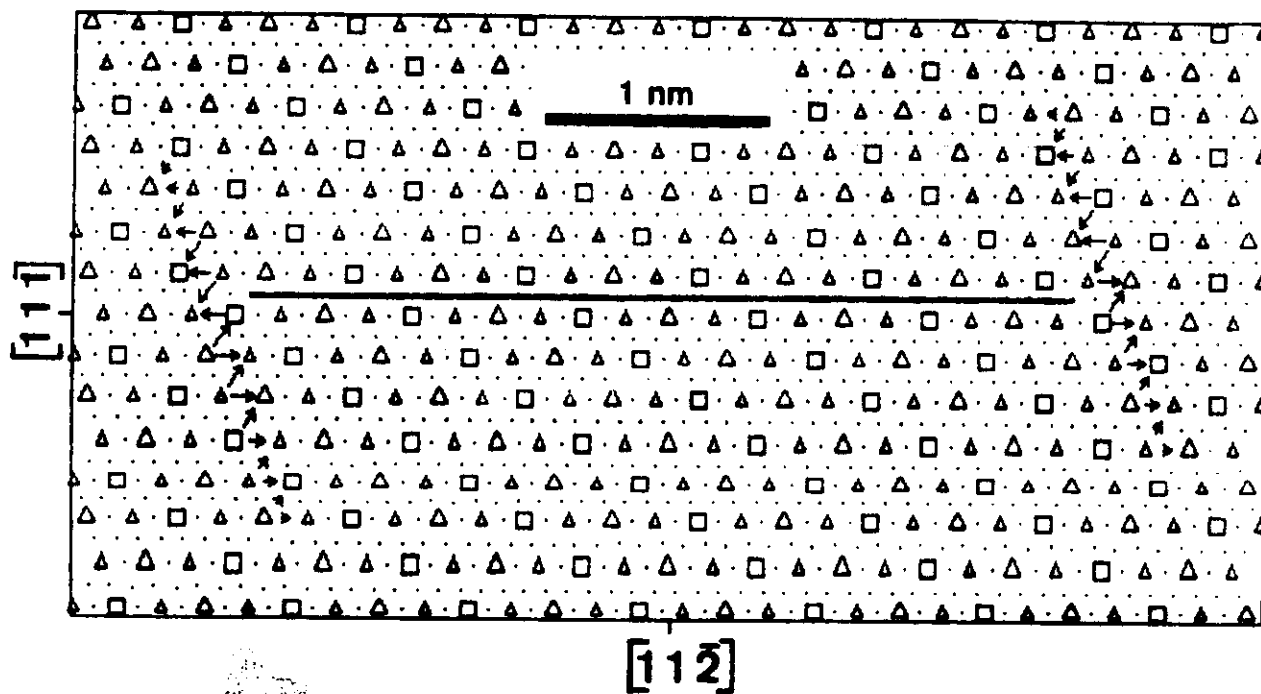


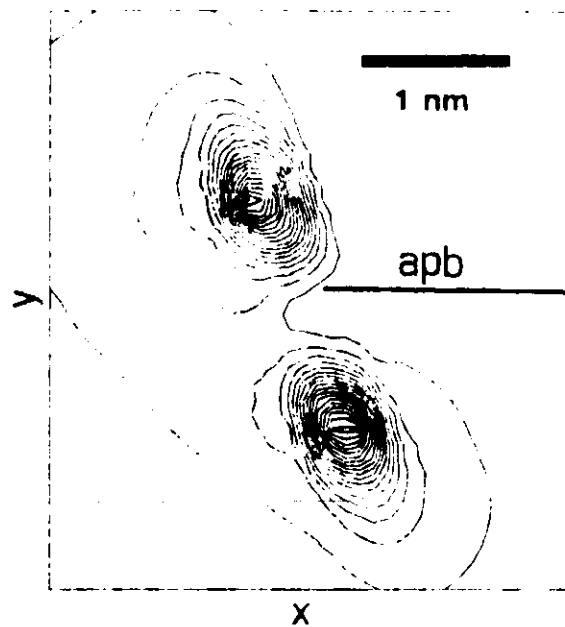
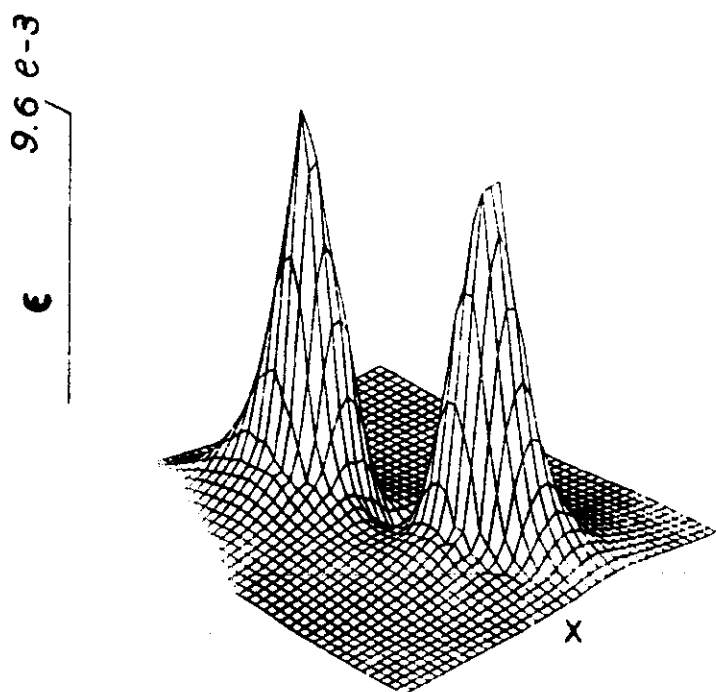




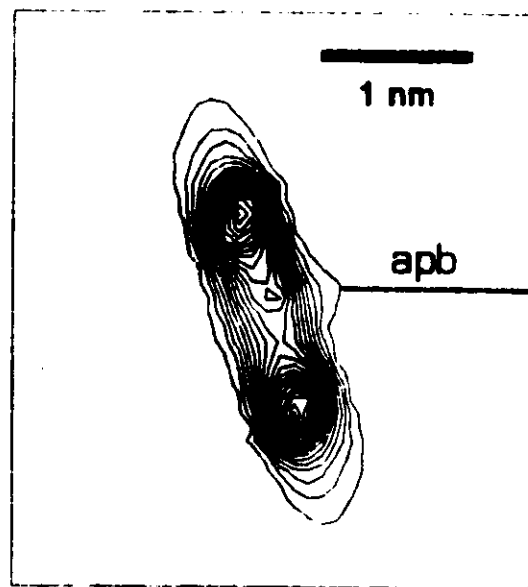
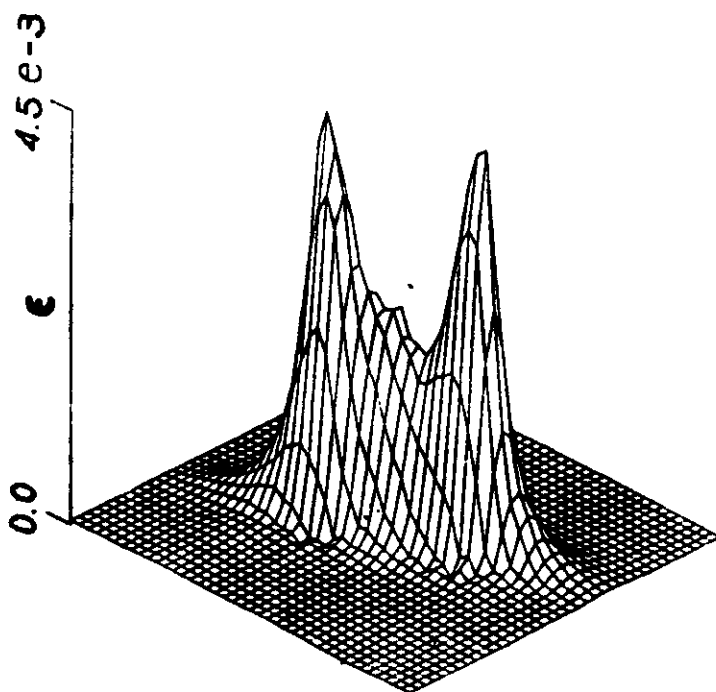








a



b

